

LIBRARIES MICHIGAN STATE UNIVERSITY EAST LANSING, MICH 48824-1048

This is to certify that the thesis entitled

TEMPERATURE CONSIDERATIONS FOR A WIRELESS IMPLANTABLE MEMS PRESSURE SENSOR

presented by

ROBERT DOYLE CABLE III

has been accepted towards fulfillment of the requirements for the

M.S. degree in MECHANICAL ENGINEERING

Major Professor's Signature

Date

MSU is an Affirmative Action/Equal Opportunity Institution

PLACE IN RETURN BOX to remove this checkout from your record. TO AVOID FINES return on or before date due. MAY BE RECALLED with earlier due date if requested.

DATE DUE	DATE DUE	DATE DUE
	-	

6/01 c:/CIRC/DateDue.p65-p.15

TEMPERATURE CONSIDERATIONS FOR A WIRELESS IMPLANTABLE MEMS PRESSURE SENSOR

By

Robert Doyle Cable III

A THESIS

Submitted to
Michigan State University
in partial fulfillment of the requirements
for the degree of

MASTER OF SCIENCE

Department of Mechanical Engineering

2004

ABSTRACT

TEMPERATURE CONSIDERATIONS FOR A WIRELESS IMPLANTABLE MEMS PRESSURE SENSOR

By

Robert Doyle Cable III

Elevated Intraocular Pressure (IOP) is the main risk factor associated with glaucoma. A continuous IOP monitoring system is being developed as a research tool to study glaucoma and ultimately reduce the number of people suffering from glaucoma related blindness. The main component of the system is a MEMS pressure sensor. The sensor, based on a RLC circuit, utilizes capacitive sensing and is powered by wireless telemetry, a requirement for implantation in the eye. The temperature range of the sensor's environment is investigated using a finite element model of the eye and by impinging an air jet with varying velocities, temperatures, and relative humidities on the eye of a cat. The sensitivity of the sensor and its associated circuit elements to temperature changes is examined. This research confirms that IOP readings are sensitive to temperature variations in the sensor's environment and further demonstrates the potential of the sensor to record temperature independent of pressure.

This thesis is dedicated to my family who made many sacrifices while supporting me financially and mentally through all my years of schooling, and to my friends who urged me to never quit and reminded me of the light at the end of the tunnel. I would not have come this far without you.

ACKNOWLEDGEMENTS

I would like to express my thanks to Dr. John R. Lloyd for his patience and guidance as my advisor. My master's committee members Dr. Arthur J. Weber and Dr. Timothy A. Grotjohn provided a great deal of assistance in my research.

This work was funded in part by Alcon Incorporated.

TABLE OF CONTENTS

LIST OF TABLES	vi
LIST OF FIGURES	ix
NOMENCLATURE	xiii
INTRODUCTION	1
CHAPTER 1	
INTRODUCTION	
1.1 Glaucoma Background	
1.2 Currently Available Glaucoma Tests	
1.3 IOP Sensor as a Superior Glaucoma Research Tool	
CHAPTER 2	
SENSOR INFORMATION	
2.1 Description of Pressure Monitoring System	
2.2 Overview for Determining IOP	
2.3 Description of how the System Works	
2.4 Location of Implantation	
CHAPTER 3	
TEMPERATURE AND PRESSURE CONSIDERATIONS	29
3.1 Fabrication	29
3.2 RLC Considerations	30
3.2.1 Resistor Considerations	30
3.2.2 Inductor Considerations	48
3.2.3 Capacitor Considerations	55
3.3 Cavity Pressure Considerations	
CHAPTER 4	
EYE CONSIDERATIONS	
4.1 Eye Models Available in Literature	
4.2 Heat Transfer Model of the Human Eye	80
4.3 Cat Testing	
4.4 Simulation Comparison to Cat Testing	
CHAPTER 5	
FUTURE WORK	
5.1 Sensor	
5.2 Extraocular Components	98
5.3 Chamber Testing	98

5.4 Implantation	101
CHAPTER 6	
SOCIAL AND ETHICAL CONSIDERATIONS	103
CHAPTER 7	
CONCLUSIONS	105
BIBLIOGRAPHY	108

LIST OF TABLES

Chapter 2. Sensor Information
Table 2.1 Plate Spacing, Capacitance and Natural Frequency23
Table 2.2 Diaphragm Properties and Dimensions24
Table 2.3 Pressure Limits and Characteristics25
Chapter 3. Temperature and Pressure Considerations
Table 3.1 Sensitivities of Resistor models
Table 3.2 Additional Capacitance Effects on Natural Frequency Range51
Table 3.3 f _{rL} , Operating Range of the Sensor53
Table 3.4 Inductance Equation Parameters54
Table 3.5 Constant Thermal Conductivities69
Table 3.6 Thermal Conductivity of Air69
Table 3.7 FEM Analysis Results73
Chapter 4. Eye Considerations
Table 4.1 Steady-state Temperatures (Control Values)76
Table 4.2 Steady-state Temperatures (Increased Ambient)76
Table 4.3 Steady-state Temperatures (Increased Body-core)
Table 4.4 Corneal Surface Temperatures for 2100 W/m ² Incident Irradiation78
Table 4.5 The Effect of Ambient Temperature on Temperature Rises Experienced in the Eye Exposed to an Incident Irradiance of 1250 W/m ² 79
Table 4.6 Experimental Rabbit Data80
Table 4.7 Tissue Thermal Conductivities8

Table 4.8 Cat Testing Initial Conditions	86
Table 4.9 Cat Testing Results	86
Table 4.10 Constants for Nu _{st} Correlation	90
Table 4.11 Jet Properties	92
Table 4.12 Simulation Comparison to Cat Testing	95

LIST OF FIGURES

Chapter 1. Introduction	
Figure 1.1 Representation of the Eye	1
Chapter 2. Sensor Information	
Figure 2.1 Pressure Sensor with Overall Dimensions	5
Figure 2.2 Base of the Sensor	6
Figure 2.3 Data Acquisition and Processing Device	7
Figure 2.4 Process for Determining IOP	10
Figure 2.5 Equivalent Circuit	11
Figure 2.6 Current, Voltage Relationship – Resistor	12
Figure 2.7 Current, Voltage Relationship – Capacitor	13
Figure 2.8 Current, Voltage Relationship – Inductor	14
Figure 2.9 RLC Phasor Diagrams	14
Figure 2.10 Phasor Diagram of Impedance for the Internal Circuit	15
Figure 2.11 Internal Component Voltage Drops vs. Frequency	17
Figure 2.12 Equivalent Circuit During Mutual Inductance	19
Figure 2.13 External Voltage Drop vs. Frequency	20
Figure 2.14 External Current vs. Frequency	21
Figure 2.15 Sensor Location	26
Figure 2.16 Resonance Curves for Coupled Circuits	27
Chapter 3. Temperature and Pressure Considerations	
Figure 3.1 Effect of Frequency on Skin Depth	31

Figure 3.2 Skin Depth vs. Frequency	32
Figure 3.3 Resistance vs. Frequency	33
Figure 3.4 Resistance vs. Temperature	34
Figure 3.5 Line Width Variation of Coil for Different Temperatures	36
Figure 3.6 R(CTE) vs. Temperature	37
Figure 3.7 Resistance Variations with Temperature	37
Figure 3.8 Resistance Change on Internal Peak Current Curve	39
Figure 3.9 Resistance Change on Internal Voltage Curve	39
Figure 3.10 Resistance Change on External Peak Current Curve	40
Figure 3.11 Resistance Change on External Voltage Curve	41
Figure 3.12 Internal Circuit Phase Angle	42
Figure 3.13 Resistance Change on Internal Phase Curve	42
Figure 3.14 External Circuit Phase Angle	43
Figure 3.15 Resistance Change on External Phase Curve	44
Figure 3.16 Instantaneous Power in Internal Circuit	45
Figure 3.17 P _{rms} in Internal Circuit	46
Figure 3.18 Thermal Noise vs. Temperature	47
Figure 3.19 Dip Measurement from R _{ext} Voltage Profile	48
Figure 3.20 Sensor Equivalent Circuit Showing Additional Capacitance	50
Figure 3.21 The Q Variation of an Inductor with Frequency	52
Figure 3.22 Layout for a Square Spiral Inductor	54
Figure 3.23 Inductance vs. Temperature	
Figure 3.24 Hinged Plate Capacitor Model	

Figure 3.25 Capacitance Derivation Schematic	56
Figure 3.26 Comparison of Capacitance Models	58
Figure 3.27 Capacitance vs. Cavity Temperature	59
Figure 3.28 Model of a Spherical Segment	60
Figure 3.29 C _{ε(P-V)} vs. Plate Spacing	62
Figure 3.30 $C_{\varepsilon(P-T)}$ vs. Pressure	63
Figure 3.31 C _T vs. Temperature	64
Figure 3.32 FEM Model	67
Figure 3.33 Close-up of Cavity	67
Figure 3.34 Entire Meshed Model	70
Figure 3.35 Meshed Cavity	71
Figure 3.36 Temperature Distribution in the Sensor	72
Figure 3.37 Cavity Temperature Distribution	72
Figure 3.38 Cavity Pressure vs. Temperature	74
Chapter 4. Eye Considerations	
Figure 4.1 FEM Human Eye Model	81
Figure 4.2 Temperature Distributions in the Eye	83
Figure 4.3 Test Rig for Cat Testing.	84
Figure 4.4 Hypodermic Needle Thermocouple Probe	85
Figure 4.5 Effect of Jet Relative Humidity on Ocular Temperature Changes	s87
Figure 4.6 Effect of Jet Velocity on Ocular Temperature Changes	88
Figure 4.7 Nusselt, Reynolds Numbers From Cat Testing	93
Figure 4.8 Region for Temperature Recording from Simulations	94

Chapter 5. Future Work

Figure 5.1 Top View of Sensor	97
Figure 5.2 Bottom View of Sensor	98
Figure 5.3 Pressure Chamber	100
Figure 5.4 Pressure Chamber Close-up.	101

NOMENCLATURE

A Overlapping Capacitor Plate Area (m²), Cross-sectional Area of a

Conductor (m²)

A_o Nominal Overlapping Capacitor Plate Area (m²)

A_T Temperature Dependant Overlapping Capacitor Plate Area (m²)

B Bandwidth (Hertz)

C Capacitance (Farads)

C_{eq} Equivalent Capacitance (Farads)

C_{HP} Hinged Plate Capacitance (Farads)

C_{L-L} Capacitance between Inductor Windings (Farads)

C_{Pave} Average Plate Spacing Capacitance (Farads)

C_{Si-L} Silicon Recess to Inductor Capacitance (Farads)

C_T Temperature Dependant Capacitance (Farads)

 $C_{\epsilon(P-T)}$ Capacitance as a Function of Temperature Dependant Pressure (Farads)

 $C_{\epsilon(P-V)}$ Capacitance as a Function of Volume Dependant Pressure (Farads)

D Impingement Surface Diameter (Meters), Eye Diameter (Meters)

E Young's Modulus (Pascals)

I Current (Amps)

I_{int} Sensor Current (Amps)

 I_{o} Current Amplitude (Amps) Current through Resistor (Amps) I_R L Inductance (Henries), Length of a Conductor (Meters), Sensor Cavity Width (Meters), Nozzle-to-surface Distance (Meters) External Circuit Inductance (Henries) Lext Sensor Inductance (Henries) Lint L_{H} Line Height of Inductor (Meters) Temperature Dependant Inductor Line Height (Meters) L_HT L_{L} Line Length of Inductor (Meters) L_{LT} Temperature Dependant Inductor Line Length (Meters) Calculated Inductance (Henries) LMON

L_o Nominal Length (Meters)

L_W Line Width of Inductor (Meters)

LWT Temperature Dependant Inductor Line Width (Meters)

M Mutual Inductance (Henries)

Nu_{st} Stagnation Point Nusselt Number

P Pressure (Atmospheres)

Partial Pressure of Air (Pa)

P_m Pressure of Fluid Mixture (Pa)

P_v Partial Pressure of Steam (Pa)

Pext Pressure on External Diaphragm Surface (atm, mmHg)

P_{int} Pressure on Internal Diaphragm Surface (atm, mmHg)

P_{rms} Root Mean Square Power (Watts)

Q Ratio of Inductor Reactance to Resistance

R Resistance (Ohms)

Raj Rayleigh Number

Re Reynolds Number

R_{ext} External Circuit Impedance (Ohms)

R_{int} Sensor Resistance (Ohms)

R_o Nominal Resistance (Ohms)

R_T Temperature Dependent Resistance (Ohms)

R₁₁ Universal Gas Constant equal to 82.05 (L*atm)/(kmol*K)

T Temperature (°C, K)

V Voltage (Volts), Volume (Liters), Fluid Velocity (m/s)

V_{cav} Sensor Cavity Volume (Liters)

V_N Root Mean Square Noise Voltage (Volts)

V_o Voltage Amplitude (Volts), Nominal Sensor Cavity Volume (Liters)

V_R Voltage Drop across Resistor (Volts)

Volume of a Spherical Segment (m³) V_{seg} Side Length of Square Electrode (Meters) W Mole Fraction of Air X_1 X_2 Mole Fraction of Steam Capacitive Reactance (Ohms) $X_{\mathbb{C}}$ Inductive Reactance (Ohms) X_{L} X_{M} Induced Reactance (Ohms) Z Impedance (Ohms) Zext External Circuit Impedance (Ohms) Zint Internal Circuit Impedance (Ohms) Half of the Diaphragm Side Length (Meters) a d Capacitor Plate Spacing (Meters), Nozzle Diameter (Meters) Average Spiral Diameter of Inductor (µm) dAVG Outer Spiral Diameter of Inductor (µm) dout Silicon Recess to Inductor Spacing (Meters) dSi-L $f_{\mathbf{r}}$ Natural Frequency (Hertz)

Inductor Self Resonant Frequency (Hertz)

Diaphragm Thickness (Meters)

 f_{rL}

g

h

Plate Spacing for Zero Deflection (Meters), Gravity (m/s²)

h_{OAu}	Nominal Electrode Height (Meters)
h _s	Convection Coefficient (Wm ⁻¹ K ⁻¹)
h _{st}	Stagnation Point Convection Coefficient (Wm ⁻¹ K ⁻¹)
h_{TAu}	Unconstrained Electrode Height (Meters)
k	Mutual Inductance Coupling Coefficient, Boltzmann's Constant equal to 1.38E-23 (J/K), Thermal Conductivity (W/m*K)
$\mathbf{k_1}$	Air Thermal Conductivity (W/m*K)
k ₂	Steam Thermal Conductivity (W/m*K)
k _m	Fluid Mixture Thermal Conductivity (W/m*K)
n	Number of Moles (Kilomoles), Number of Inductor Spiral Turns
S	Inductor Line Spacing (µm), Spacing between Lowest Point of Hinged Plate and Electrode (Meters)
t	Time (Seconds)
w _c	Diaphragm Center Deflection (Meters)
Φ_1	Total Flux in Coil 1
Φ_{12}	Flux from Coil 1 to Coil 2, Thermal Conductivity Mixture Coefficient equal to 0.8153
Φ2	Total Flux in Coil 2
Φ ₂₁	Flux from Coil 2 to Coil 1, Thermal Conductivity Mixture Coefficient equal to 0.7257
Ψ_{12}	Dynamic Viscosity Mixture Coefficient equal to 0.8390

Ψ_{21}	Dynamic Viscosity Mixture Coefficient equal to 0.7438
α	Inductor Layout Dependant Coefficient, Thermal Diffusivity (m ² /s)
β	Inductor Layout Dependant Coefficient, Expansion Coefficient for an Ideal Gas (K ⁻¹)
α ₇₇₄₀	Linear Coefficient of Thermal Expansion for Glass equal to 3.25E-6 (°C ⁻¹)
$\alpha_{\hbox{Au}}$	Linear Coefficient of Thermal Expansion for Gold equal to 14.2E-6 (°C ⁻¹)
$\alpha_{\mathbf{R}}$	Temperature Coefficient of Resistance (°C ⁻¹)
α_{T}	Linear Coefficient of Thermal Expansion (°C ⁻¹)
$\alpha_{\epsilon P}$	Pressure Coefficient of the Dielectric Constant of Air equal to 100E-6 (°C ⁻¹)
$\alpha_{\epsilon T}$	Temperature Coefficient of the Dielectric Constant of Air equal to 2E-6 (°C ⁻¹)
δ	Skin Depth (Meters)
ε7740	Dielectric Constant of Glass equal to 44.25 (pF/m)
ϵ_0	Dielectric Constant of Free Space equal to 8.85E-12 (F/m)
$\epsilon_{\mathbf{r}}$	Relative Dielectric Constant
ф	Phase Angle (Radians), Relative Humidity
μ	Permeability of a Metal (H/m), Dynamic Fluid Viscosity (Pa*s)
μ_1	Air Dynamic Viscosity (Pa*s)
μ_2	Steam Dynamic Viscosity (Pa*s)

$\mu_{\mathbf{m}}$	Fluid Mixture Dynamic Viscosity (Pa*s)
μ_0	Permeability of Free Space equal to $4\pi E-7$ (H/m)
μ_r	Relative Permeability of a Material
ν	Poisson's Ratio, Kinematic Viscosity (m ² /s)
θ	Sensor Phase Angle (Radians), Angle between Hinged Plate and Horizontal (Radians)
ρ	Resistivity of a Conductor (Ω^*m), Fluid Density (kg/m ³)
σ	Diaphragm Intrinsic Stress (Pascals)
ω	Angular Frequency (Radians/Second)
$\omega_{\mathbf{r}}$	Natural Frequency (Radians/Second)

Chapter 1. Introduction

1.1 Glaucoma Background

Glaucoma is a group of eye diseases that slowly steals sight, often without warning or symptoms [1]. Loss of vision results from damage to the optic nerve that carries the images we see to the brain. Certain groups of people are at higher risk for developing glaucoma than others. These groups include African-Americans, Asian-Americans, persons over the age of 60, those with a family history of glaucoma, people who have suffered blunt trauma or a penetrating injury to the eye or head, and finally people with a history of steroid use. Although it is possible to experience vision loss from glaucoma with "normal" intraocular pressure (IOP), between 12-22 mmHg, elevated IOP is the main risk factor associated with the disease [1]. IOP is maintained by a balance in the production and drainage of aqueous humor from the anterior chamber of the eye, refer to Figure 1.1.

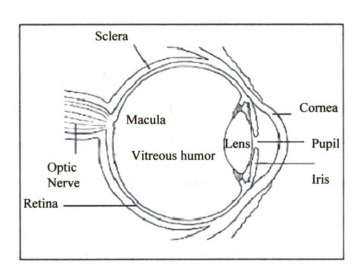


Figure 1.1 Representation of the Eye

Elevated IOP can range from moderately high pressures over 22 mmHg to extreme levels of 45-50 mmHg [2].

The two main types of glaucoma are primary open angle glaucoma (POAG) and angle closure glaucoma. POAG is the most common form and affects over 3 million Americans [1]. This occurs when the drainage canals for the aqueous humor become clogged causing IOP to rise [1]. POAG develops slowly, sometimes without noticeable sight loss for many years. If caught and treated early, POAG usually responds well to medications. Angle closure glaucoma, also known as acute glaucoma or narrow angle glaucoma, occurs when the drainage canals get blocked and IOP rises very rapidly [1]. Blocking results from the outer edge of the iris bunching up over the drainage canals [1]. This happens when the pupil enlarges too much or too quickly. Surgery to remove the outer portion of the iris is usually successful and long lasting. Currently there is no cure for glaucoma. It is a chronic disease that must be treated for life.

1.2 Currently Available Glaucoma Tests

Regular eye check-ups include two routine glaucoma tests, tonometry and ophthalmoscopy [1]. The tonometry test measures IOP. Typically drops are used to numb the eye. The doctor then uses a tonometer to measure the pressure inside the eye. Ophthalmoscopy examines the inside of the eye, specifically the optic nerve [1]. In a darkened room, the doctor uses an ophthalmoscope to inspect the shape and color of the optic nerve [1]. If the IOP is not within the normal range, or if the optic nerve looks unusual, two special tests may be performed. These tests are perimetry and gonioscopy. During perimetry, the patient looks straight ahead and indicates when a light passes their

peripheral vision. Gonioscopy checks whether the angle where the iris meets the cornea is open or closed, indicating if either open angle or closed angle glaucoma is present. While accurate, there are several drawbacks to these tests. Only a single reading at an instant in time is recorded in a controlled environment. Furthermore, these readings are usually separated by long periods of time between visits to the physician's office. A patient's IOP changes on a daily basis. Fluctuations in IOP around an average value occur due to changes in activity and environment [3]. It is crucial to monitor IOP on a continuous basis to immediately administer treatment at the onset of high IOP and prevent permanent damage that could occur between check-ups. A research tool is needed to better understand what affects IOP and the role it plays in developing glaucoma.

1.3 IOP Sensor as a Superior Glaucoma Research Tool

The sensor presented in this thesis was designed by Goodall and holds many advantages over current glaucoma tests [4]. First, the sensor will monitor IOP on a continuous basis. This will allow for immediate treatment to prevent permanent damage and vision loss as discussed in the previous section. This continuous monitoring will provide valuable information to researchers regarding IOP and the development of glaucoma. It is unknown whether peak IOP levels, cumulative IOP over a period of time, average IOP levels, or high and low IOP differential levels have the greatest effect on the eye. Continuous monitoring with a time record will also allow researchers to determine how a patient's activities, lifestyle and environment affect their IOP.

The overall dimensions of the cubic sensor are 2 mm x 2 mm x 1 mm. The sensor will be powered by wireless telemetry, requiring no batteries. Along with the small size,

this allows for the sensor to be implanted in the patient's eye without affecting vision or comfort. The sensor is designed to measure pressures in the range of 0 to 60 mmHg, covering the limits in IOP a patient may experience. However, the design of the sensor can be altered to measure a different range of pressures for other applications.

Due to the design of the sensor, readings from the IOP monitoring system will be sensitive to changes in temperature. This work investigates possible temperatures the sensor may experience while implanted in the eye. Temperature fluctuations in the sensor caused by the sensor's environment and operation will be used to determine the sensitivity of the pressure readings to these changes.

Chapter 2. Sensor Information

2.1 Description of Pressure Monitoring System

The pressure monitoring system discussed in this thesis consists of three components. The first component of the system is the implantable pressure sensor. The pressure sensor has a height of 1 mm and a width of 2 mm and represents a hollow sealed cube as shown in Figure 2.1.

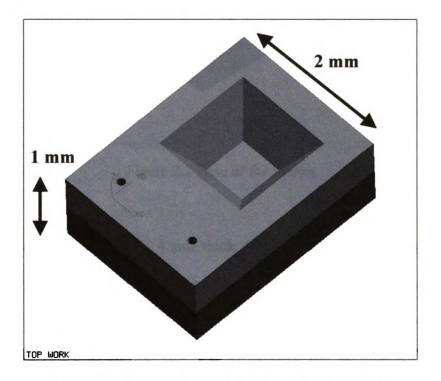


Figure 2.1 Pressure Sensor with Overall Dimensions

The exact length of the sensor will be determined during the fabrication of the final batch of sensors. The overall length is expected to be approximately 3 mm. The body of the sensor will contain two holes through which sutures will be threaded during implantation. Exact hole dimensions and positioning will also be determined during final batch

fabrication. The base of the cube consists of a square spiral inductor and an electrode, as shown in Figure 2.2.

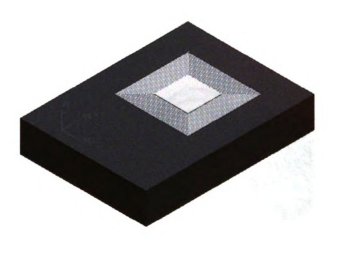


Figure 2.2 Base of the Sensor

The lid of the sealed cube is a 4 µm thick diaphragm. This diaphragm is also an electrode, creating a capacitance with the base of the cube. The diaphragm and electrode act as a variable capacitor, dependent upon the deflection of the diaphragm. Taking into account the resistance in the inductor, the whole cube can be modeled as a resistor-inductor-capacitor (RLC) circuit.

The second component of the system is the data acquisition and processing device that will remain outside the patient's body. This device contains a larger RL circuit. The external device will be battery powered. When placed in close proximity to the implanted sensor, the external inductor will induce a current in the sensor's inductor, thus eliminating the need for a physical connection between the two. The external inductor

will be housed in a patch to be placed on the side of the patient's head near the eye. The patch will be connected to a unit containing the rest of the circuitry. This unit may be worn in the patient's shirt pocket or attached at the waist. Unlike the sensor, the external circuit contains an actual resistor. Information about the sensor will be obtained by interrogating this element. The data acquisition and processing device is shown aligned with the sensor in Figure 2.3.

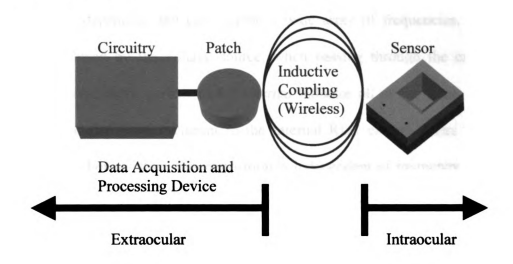


Figure 2.3 Data Acquisition and Processing Device

The third component of the system is a central database that will maintain a time record of the patient's IOP measurements. This will allow for correlations between the patient's lifestyle, treatment strategies and changes in IOP. This component can be located in the patient's home. The patient can download logged information from the data acquisition and processing device to this component at daily or perhaps weekly intervals. There is also the possibility for the central database to send these records to the physician over the internet or through phone lines.

An extensive description of the sensor design and fabrication is provided by Goodall [4].

2.2 Overview for Determining IOP

Measuring IOP is not an easy task and must be done in several steps. The external RL circuit is powered by an oscillating sinusoidal voltage source. This voltage is frequency dependant and can assume a wide array of frequencies. The sinusoidal current produced by the voltage source, when passing through the external inductor, induces an equivalent current in the internal inductor all at the same frequency. The opposition to the flow of current in the internal RLC circuit differs for the types of components. For resistors, this opposition is independent of frequency and is called the resistance. The opposition to current flow due to inductors and capacitors is frequency dependant and known as reactance. The overall opposition to the flow of current in a circuit is known as the impedance and is the sum of the resistance and the reactance. Due to the nature of the reactance for the inductor and capacitor, they will cancel each other out at a particular frequency known as the natural frequency. The natural frequency is dependant on the inductor and capacitor values for the circuit. The cancellation that occurs at the natural frequency results in a local minimum for the internal circuit's impedance. When the external and internal RLC circuits are placed in close proximity, the inductive coupling induces an additional reactance in the external circuit. This reactance is at a local maximum for the local minimum impedance of the internal circuit at the natural frequency.

With the internal circuit inaccessible, implanted in the body, it is therefore necessary to interrogate components of the external circuit. There is a finite voltage drop along the closed-loop path of any circuit. With the induced reactance in the external circuit at a local maximum, this leaves less voltage to be dropped across the external resistor and inductor. When the internal circuit is at the natural frequency, the voltage drop across the accessible external resistor will therefore be at a local minimum. Comparatively, the current through the external resistor, which can be determined from the voltage drop, will also be at a local minimum. By sweeping the voltage source through a range of frequencies and observing the voltage drop profile across the external resistor, the natural frequency of the internal circuit can be determined.

The natural frequency of the internal circuit is dependent on the circuit's inductor and capacitor values. Knowing the natural frequency and the inductor's fixed value, it is possible to determine the value of the capacitance at that point in time. The capacitance created by the fixed electrode and flexible diaphragm can be modeled as a parallel plate capacitor. The capacitance is dependent on the dielectric constant of the material between the plates, the spacing between the plates and the area of the plates. The sealed, hollow cube form of the sensor contains air at atmospheric pressure, the dielectric constant for which is known. The dimensions of the diaphragm lid and electrode plate are also known analogous to the area of the parallel plates. Knowing the capacitance, along with the other parameters, it is possible to determine the spacing between the plates in the capacitor model.

Equations governing the vertical deflection of the center of a diaphragm subject to a uniform differential pressure are known. These equations are dependant on diaphragm

dimensions and properties. With these dimensions and properties known, along with the center deflection of the diaphragm from the capacitor model, the differential pressure applied to the diaphragm is known.

The differential pressure is the difference between the pressures applied at the outer and inner surfaces of the diaphragm. Knowing the differential pressure from the deflection equation and the pressure inside the sensor, the absolute pressure in the eye (IOP) can be determined. The process of obtaining IOP readings from the implanted sensor by interrogating the external device is shown in Figure 2.4.

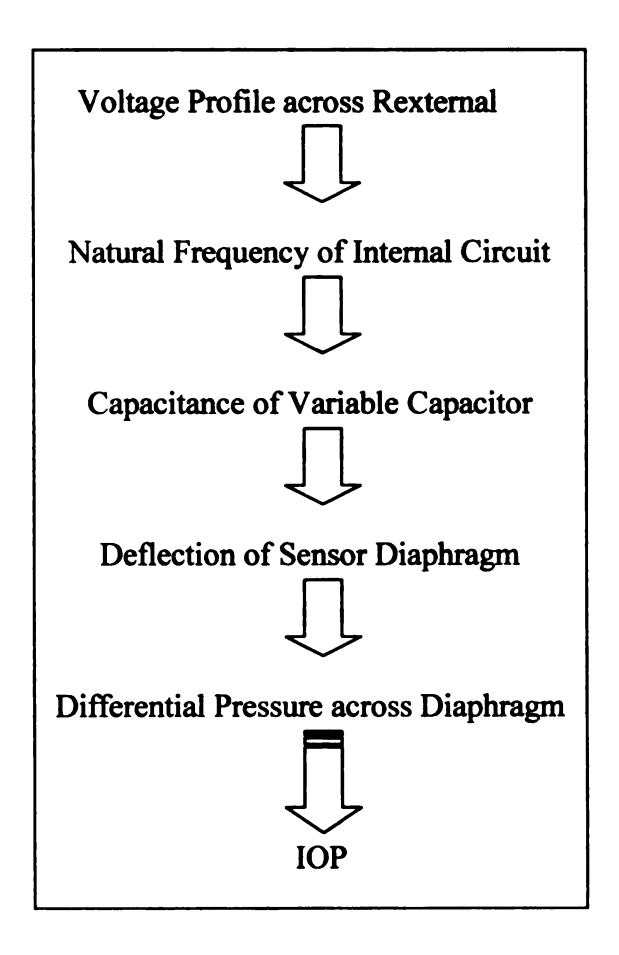


Figure 2.4 Process for Determining IOP

2.3 Description of how the System Works

Section 2.2 provided an overview of how the IOP monitoring system works; this will now be covered in detail. The equivalent circuit for the data acquisition and processing device and the implantable sensor is shown in Figure 2.5. The ovals joining the circuits represent the inductive coupling.

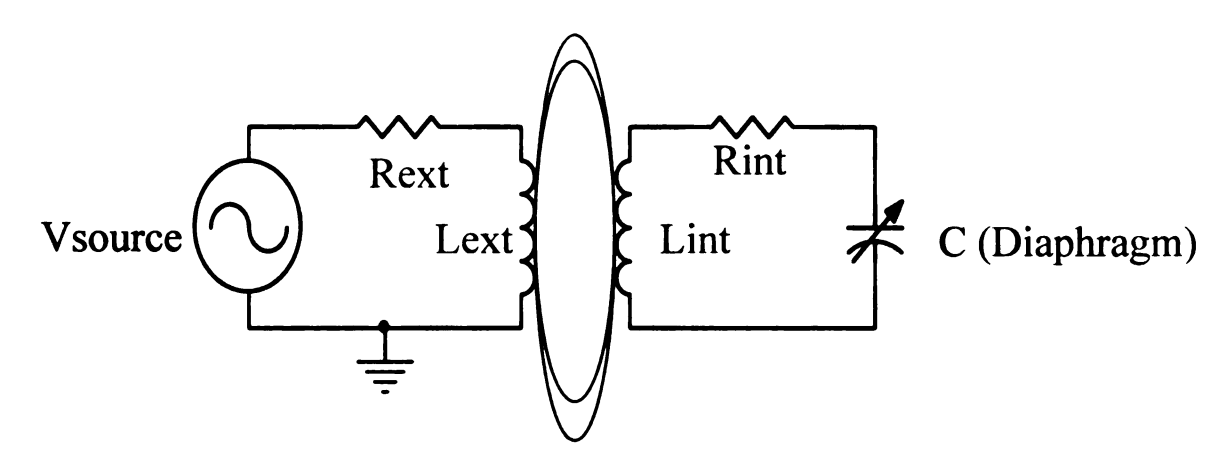


Figure 2.5 Equivalent Circuit

The inductor in the internal circuit, L_{int} , represents the square spiral inductor on the glass substrate. The internal resistor, R_{int} , represents the resistance associated with the inductor coils. The capacitor in the internal circuit, C, represents the variable capacitor formed by the flexible silicon diaphragm and the fixed gold electrode. As mentioned in Section 2.2, the external circuit is powered by an oscillating sinusoidal voltage source of the form

$$V = V_0 \sin(\omega t) \tag{2.1}$$

where V_0 is the amplitude of the voltage, ω is the angular frequency, and t is time. This voltage will create sinusoidal current in the external circuit of the form

$$I = I_0 \sin(\omega t + \phi) \tag{2.2}$$

where I_0 is the amplitude of the current, and ϕ is the phase angle between the current and the impressed voltage in radians.

When circuit elements are connected in series, as is the case for our external and internal circuits, the current in all of the elements must be the same. However, the voltage drop across the elements will be out of phase with the current to varying degrees depending on the type of element.

In a resistor, the opposition to the flow of current through that element is independent of the current frequency. This opposition is called resistance (R) and has the unit of Ohms (Ω). The instantaneous voltage required to force the alternating current (AC) through a resistor is IR. Figure 2.6 shows the relationship between the voltage and current through a resistor.

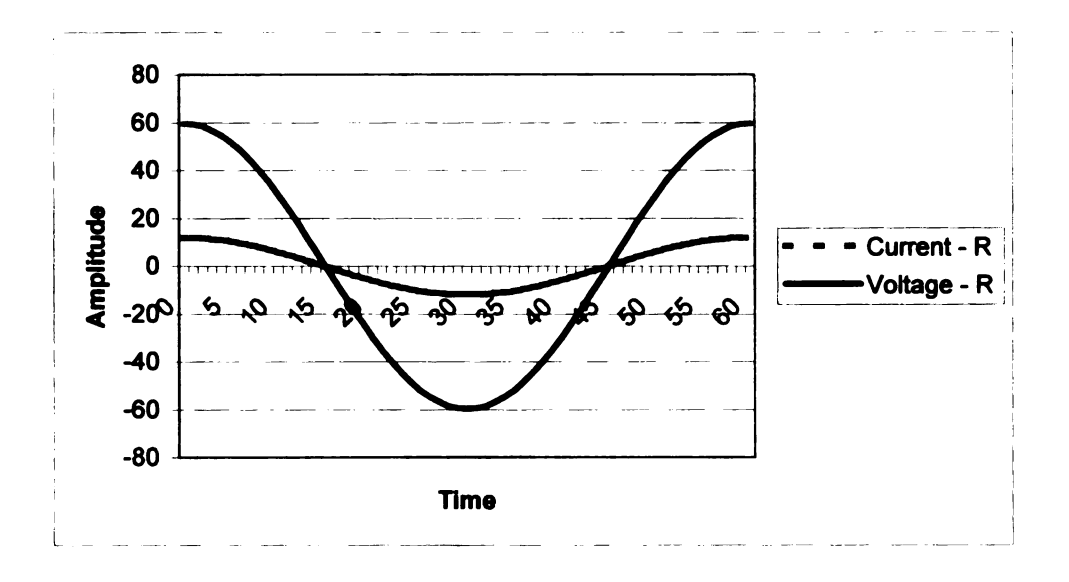


Figure 2.6 Current, Voltage Relationship – Resistor

The maximum voltage drop across the resistor is I₀R and is in phase with the current.

In capacitors and inductors, the opposition to the flow of current through that element is dependent upon the current frequency and is called reactance. Reactance also has units of Ohms. The reactance for capacitors and inductors is defined as

$$X_C = \frac{1}{\omega C} \tag{2.3}$$

and

$$X_L = \omega L \tag{2.4}$$

where C is the capacitance in Farads (F) and L is the inductance in Henries (H). The instantaneous voltage required to force the current through a capacitor is $\frac{1}{C} \int Idt$. Figure 2.7 shows the relationship between the voltage and current through a capacitor.

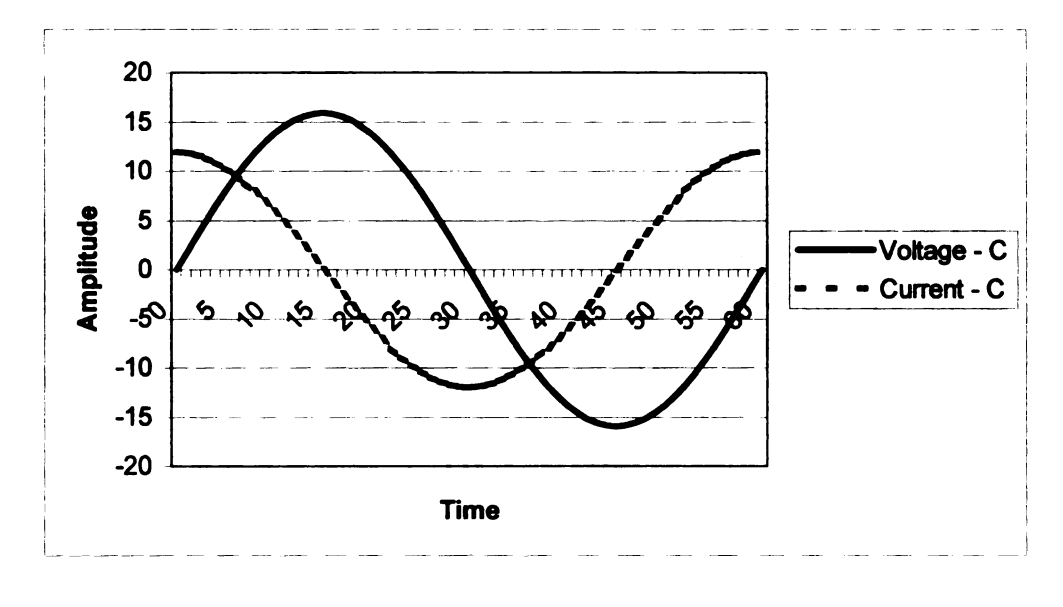


Figure 2.7 Current, Voltage Relationship - Capacitor

The maximum voltage drop across a capacitor is I_0X_C and will occur later than the maximum current, lagging by 90° [5]. The instantaneous voltage required to force the

current through an inductor is $L\frac{dI}{dt}$. The relationship between the voltage and current through an inductor is shown in Figure 2.8.

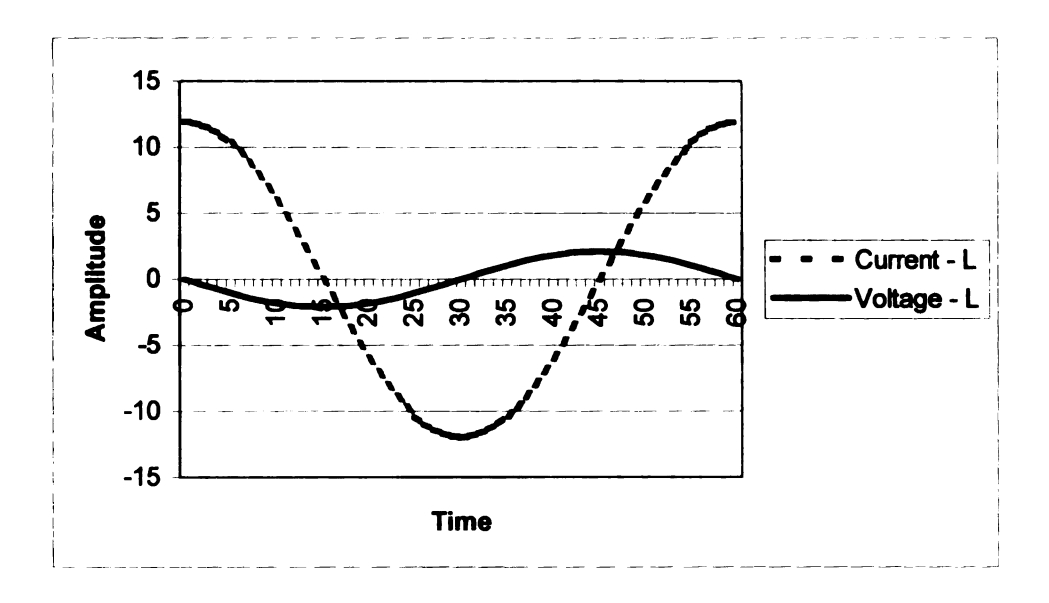


Figure 2.8 Current, Voltage Relationship - Inductor

The maximum voltage drop across an inductor is I_oX_L will occur before the maximum current, leading by 90° [5]. Phasor diagrams are a convenient way to illustrate the voltage, current and resistance, reactance phase relations between components. Phasor diagrams for RLC components are shown in Figure 2.9.

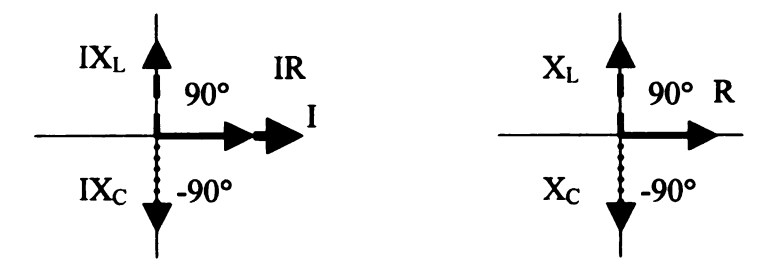


Figure 2.9 RLC Phasor Diagrams

The impedance (Z) is the overall resistance to the flow of current in a circuit. The impedance of the external circuit (Z_{ext}) can be found by adding the resistance of R_{ext} and

the reactance of L_{ext} . The resistance and reactance of the series components are out of phase and must be added as vectors. The impedance for the external circuit is

$$Z_{ext} = \sqrt{R_{ext}^2 + X_{Lext}^2} \tag{2.5}$$

The impedance for the internal circuit (Z_{int}) can be found by adding the resistance of R_{int} , along with the reactance of L_{int} and C. The impedance for the internal circuit is

$$Z_{\rm int} = \sqrt{R_{\rm int}^2 + (X_{L \, \rm int} - X_C)^2}$$
 (2.6)

Figure 2.10 shows the phasor diagram for solving Z_{int}.

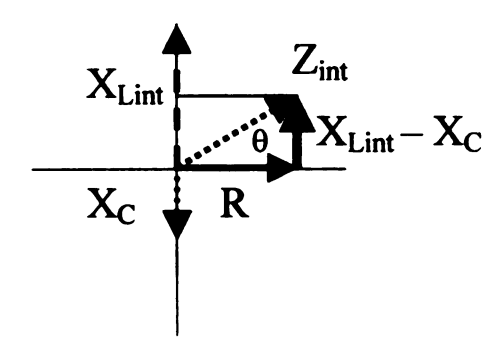


Figure 2.10 Phasor Diagram of Impedance for the Internal Circuit

The angle θ is defined as

$$\theta = \tan^{-1} \left(\frac{X_{Lint} - X_C}{R_{int}} \right) \tag{2.7}$$

and represents the phase angle between the current and the impressed voltage for the internal circuit in radians. Substituting equations 2.3 and 2.4 into equation 2.6, the impedance of the internal circuit is a function angular frequency defined as

$$Z_{\text{int}}(\omega) = \sqrt{R_{\text{int}}^2 + \left(\omega L_{\text{int}} - \frac{1}{\omega C}\right)^2}$$
 (2.8)

It can be seen by observing equation 2.8 that the inductive and capacitive reactance will cancel out at a particular frequency. This frequency is known as the natural frequency and is defined as

$$\omega_r = \frac{1}{\sqrt{L_{\text{int}}C}} \tag{2.9}$$

in radians/second. A more convenient form of the natural frequency is defined as

$$f_r = \frac{1}{2\pi\sqrt{L_{\rm int}C}} \tag{2.10}$$

in cycles/second or Hertz (Hz). Due to the cancellation of the inductive and capacitive reactance at the natural frequency, the impedance of the internal circuit will be resistive only. With a fixed amplitude impressed voltage, this local minimum in Z_{int} will result in a maximum current flowing through the circuit according to

$$I = \frac{V}{Z} \tag{2.11}$$

With the current flowing through the circuit being maximized at the natural frequency, the corresponding voltage drops across the circuit components will be maximized as well. Figure 2.11 shows a simulated plot of the voltage drops across the circuit elements as a function of frequency.

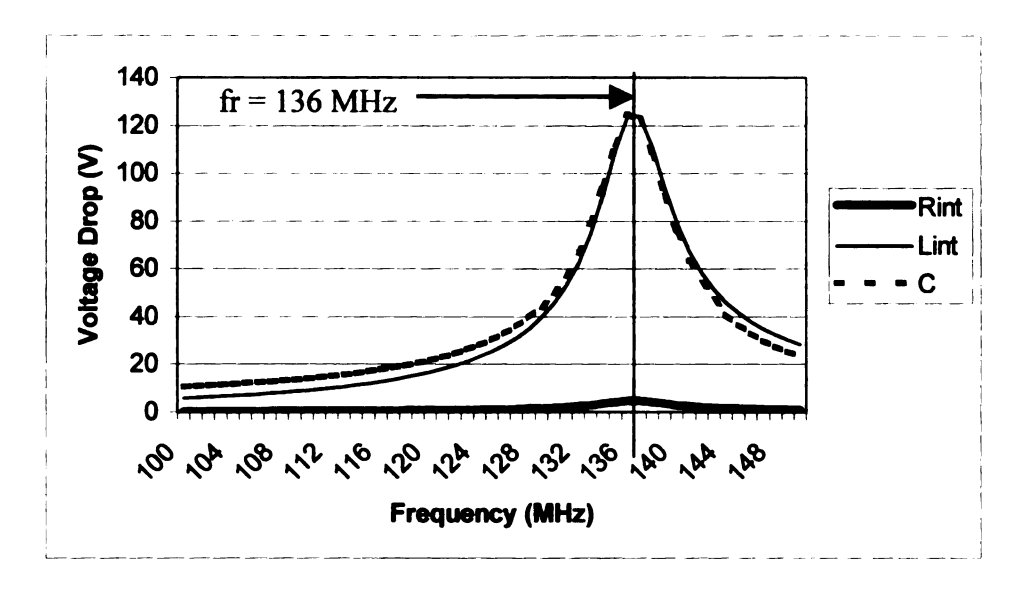


Figure 2.11 Internal Component Voltage Drops vs. Frequency

The component values used in this simulation are arbitrary and hence, the voltage drop values are irrelevant. However, the natural frequency in this simulation is 136 MHz, which is clearly indicated by the voltage peaks. If the elements in this circuit were accessible, the natural frequency could be determined by observing a component voltage drop in a frequency range of interest. With a fixed inductance for L_{int}, the present value of the variable capacitor could be established from the natural frequency. The internal circuit will be inaccessible once implanted in the eye. Therefore, information about the internal circuit must be obtained in such a way that does not require direct contact.

Once the sensor is in place, a connection is needed to power that circuit and record data. For health and safety reasons, as well as comfort, that connection must be wireless. Inductive coupling will provide that connection. When a current is passed through a wire, a magnetic field is generated around that wire. For a current carrying wire wound into a coil, in the case of an inductor, the magnetic field lines are concentrated and the flux is increased. When an AC current is passed through an

inductor, the flux generated increases and decreases sinusoidally with time just as the current is varying. If another inductor is placed in close proximity to the primary inductor, some of the magnetic field lines will pass through the secondary inductor. According to Lenz's law, the changing flux in the secondary inductor produces a current in that inductor in such a direction as to oppose the flux that is causing it [5]. This is known as mutual inductance. The produced current in the secondary inductor in turn generates a flux that also threads through the primary inductor. When the two inductors are not physically connected and air provides a path for the flux, it is known as an air-core transformer. In this type of transformer, the inductors are said to be loosely coupled. The coefficient of coupling of the two coils may be expressed as

$$k = \frac{\Phi_{12}}{\Phi_1} = \frac{\Phi_{21}}{\Phi_2} \tag{2.12}$$

where k is the coupling coefficient, Φ_1 is the total flux in coil 1, Φ_{12} is the flux from coil 1 that links to coil 2, Φ_2 is the total flux in coil 2, and Φ_{21} is the flux from coil 2 that links to coil 1 [5]. The mutual inductance for the two coils can be expressed in terms of the two inductors as

$$M = k\sqrt{L_{\text{int}}L_{\text{ext}}} \tag{2.13}$$

where M is the mutual inductance [5]. When mutual inductance occurs, an additional reactance is induced in the external circuit coupling the impedance of both circuits. This reactance is frequency dependent and can be expressed as

$$X_M(\omega) = \frac{(\omega M)^2}{Z_{\text{int}}}$$
 (2.14)

where X_M is the induced reactance in the external circuit [4]. The equivalent circuit during mutual inductance is shown in Figure 2.12.

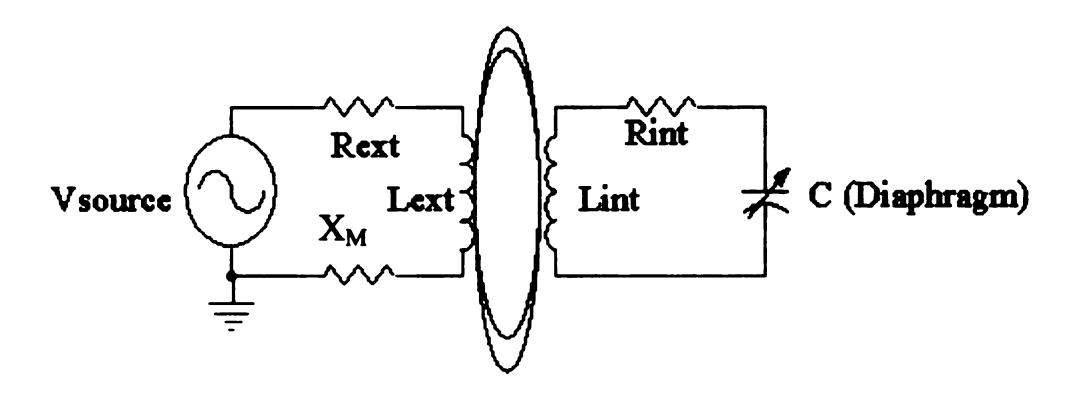


Figure 2.12 Equivalent Circuit During Mutual Inductance

By substituting the impedance of the internal circuit into equation 2.14, the induced reactance becomes

$$X_{M}(\omega) = \frac{(\omega M)^{2}}{\sqrt{R_{\text{int}}^{2} + \left(\omega L_{\text{int}} - \frac{1}{\omega C}\right)^{2}}}$$
(2.15)

With the additional induced reactance, the impedance of the external circuit when mutual inductance occurs is

$$Z_{ext}(\omega) = \sqrt{R_{ext}^2 + \left(\omega L_{ext} + \frac{(\omega M)^2}{\sqrt{R_{int}^2 + \left(\omega L_{int} - \frac{1}{\omega C}\right)^2}}\right)^2}$$
(2.16)

At the natural frequency, the induced reactance and hence $Z_{\rm ext}$ reach a local maximum. According to Kirchhoff's Voltage Law, the sum of all voltages through a loop must equal zero. Therefore, the finite amount of voltage impressed on the circuit must be dropped across its components. With $X_{\rm M}$ maximized at the natural frequency, much of the impressed voltage is spent on this reactance leaving a minimal amount to be dropped across $R_{\rm ext}$. Furthermore, according to equation 2.11, with a fixed amplitude voltage and $Z_{\rm ext}$ maximized, the current flowing through the external circuit will be minimized. This reinforces the fact that the voltage drop across $R_{\rm ext}$ will hit a local minimum at the natural frequency. Figure 2.13 shows the simulated voltage drop across $R_{\rm ext}$.

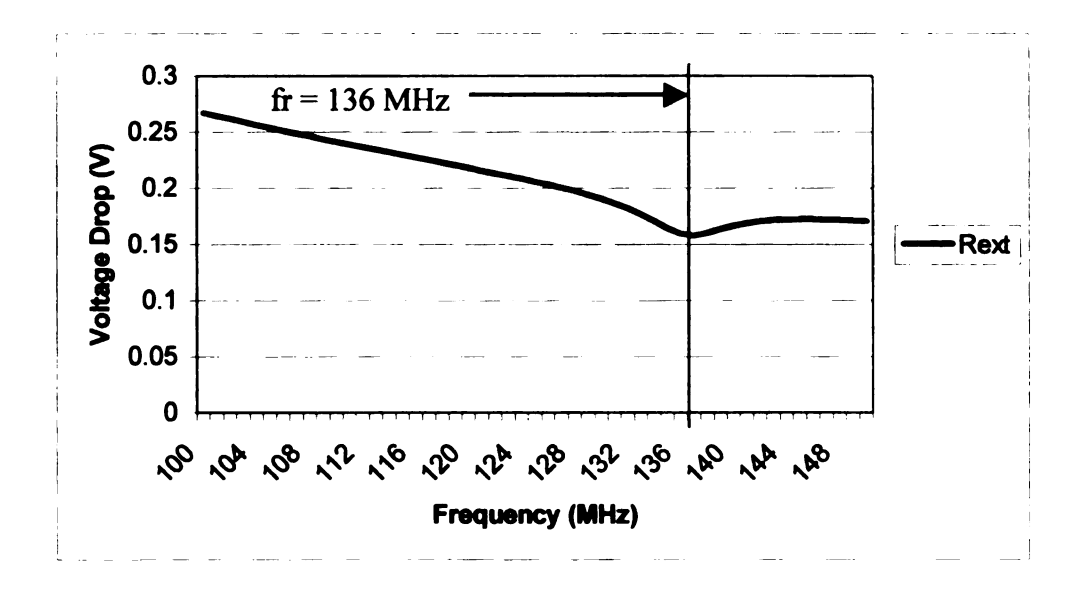


Figure 2.13 External Voltage Drop vs. Frequency

Again, the voltage drop values are arbitrary, but the voltage dip clearly indicates the natural frequency for this simulation, 136 MHz. The current through $R_{\rm ext}$ can be inferred from the voltage drop and is shown in Figure 2.14.

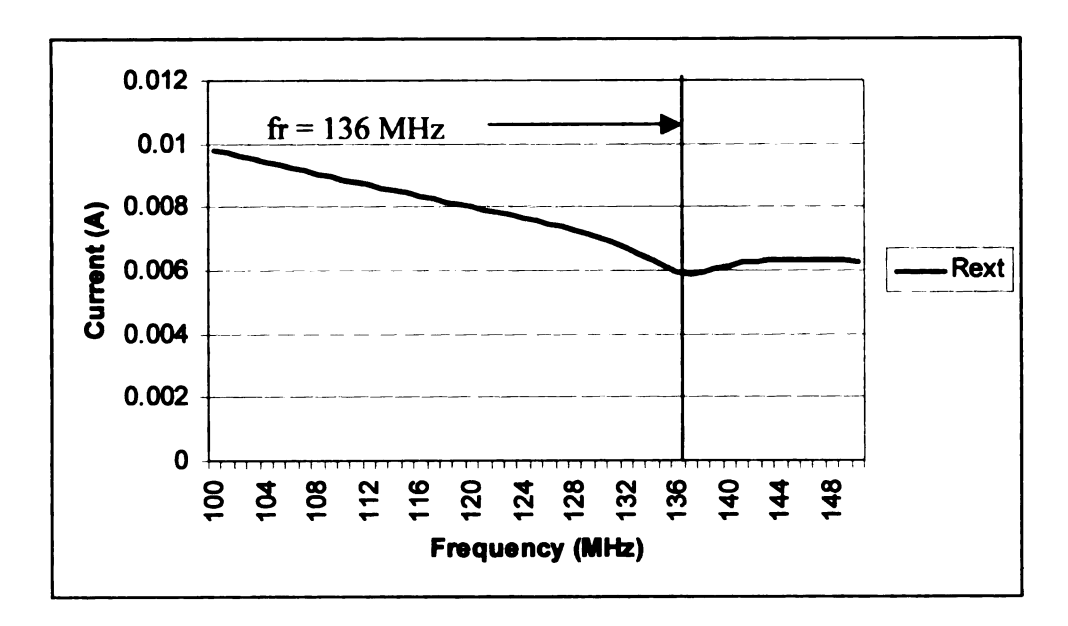


Figure 2.14 External Current vs. Frequency

The inductive coupling between the two circuits allows the internal circuit to be powered without the use of batteries, allowing its miniscule size. The wireless connection makes the IOP monitoring system safer and more comfortable to the patient. By sweeping the voltage source through a frequency range determined by the limits of the variable capacitor and exploiting the phenomenon of mutual inductance, the natural frequency of the sensor can be determined by examining an accessible component of the external circuit. With a known, fixed value for the sensor's inductance, the present value of the sensor's variable capacitor can also be determined. Upon establishing a relationship between the sensor's capacitance and the deflection of the sensor's diaphragm, the differential pressure applied to the diaphragm will be known.

The capacitor formed by fixed, gold electrode and flexible, silicon diaphragm of the sensor can be modeled as a parallel plate capacitor. The capacitance of such is given as

$$C = \frac{\varepsilon_o \varepsilon_r A}{d} \tag{2.17}$$

where C is the capacitance in Farads (F), ε_0 is the dielectric constant of free space = 8.85E-12 F/m, ϵ_r is the relative dielectric constant of the material between the plates (1 for air), A is the overlapping area of the plates in m², and d is the spacing between the plates in m [6]. The overlapping area of the plates is determined by the area of the smaller, fixed electrode. The side length of the square electrode is 537 µm resulting in an overlapping area of 2.88E5 μm^2 . The deflection of the center of the diaphragm will be used as the spacing between the plates in this model. The distance between the plates varies between its zero deflection and full-scale deflection of 0.5 µm. This corresponds to a spacing of 1.5 µm and 1 µm respectively. The capacitance is inversely proportional to the plate separation with the maximum capacitance of 2.55 pF occurring at the minimum spacing of 1 µm and the minimum capacitance of 1.7 pF occurring at the maximum spacing of 1.5 µm. Once the sensor's natural frequency is determined from the voltage profile across Rext and the fixed, known inductance of 800.2 nH is used in equation 2.10, the sensor's capacitance is known. Since the overlapping plate area and dielectric constants are fixed, using the capacitance in equation 2.17 reveals the present center deflection of the diaphragm. Capacitor plate spacing, capacitance and natural frequency information is listed in Table 2.1.

Table 2.1 Plate Spacing, Capacitance and Natural Frequency

Plate Spacing	Capacitance	Natural Frequency
1.5 μm	1.7 pF	136 MHz
1.0 μm	2.55 pF	111 MHz

Once the center deflection of the diaphragm is known, a relationship is needed between that deflection and the differential pressure across the diaphragm. The diaphragm thickness is much smaller than the diaphragm side length. Therefore, the diaphragm can be modeled as a membrane. The uniform pressure required to deflect a membrane is given by

$$\Delta P = \frac{Eh^4}{(1 - v^2)a^4} \left[4.20 \frac{w_c}{h} + 1.58 \frac{w_c^3}{h^3} + \frac{4\sigma a^2}{E} \frac{w_c}{h^3} \right]$$
 (2.18)

where ΔP is the differential pressure across the membrane in Pascals (Pa), E is the Young's Modulus is Pa, h is the diaphragm thickness in m, v is the Poisson's ratio of the diaphragm, a is one half of the diaphragm side length in m, w_c is the center deflection of the diaphragm in m, and σ is the intrinsic stress built into the diaphragm in Pa [4]. The sensor's diaphragm is heavily doped with boron to make it conductive. The introduction of the boron impurities into the silicon wafer produces considerable residual tension in the diaphragm [7]. It is common for the intrinsic stress in p^{++} silicon to be around 40 Mpa [8]. The presence of the tensile stress creates an increased stiffness in the diaphragm requiring a greater pressure differential to cause the equivalent deflection in a stress free diaphragm. Determining the material properties of the diaphragm is a challenge. The materials used in MEMS applications are relatively thin and can have

properties that differ from their bulk form [9]. In addition, silicon is an anisotropic material whose properties are orientation dependent. Fortunately, isotropic averages can be used. Diaphragm dimension and material property values used in this analysis are listed in Table 2.2.

Table 2.2 Diaphragm Properties and Dimensions

Young's Modulus	160 GPa	
Poisson's ratio	0.05	
h	4 μm	
a	275.5 μm	
σ	40 MPa	

Using the center deflection of the diaphragm, d, solved from equation 2.17 and plugging it into equation 2.18 as w_c , the present differential pressure across the sensor's diaphragm is known.

The differential pressure across the sensor's diaphragm is the difference between the pressure acting on the external surface, P_{ext} , and the internal surface, P_{int} , given as

$$\Delta P = P_{ext} - P_{int} \tag{2.19}$$

When implanted in the eye, P_{ext} will be the IOP. As a result of anodically bonding the silicon wafer and glass substrate, the pressure inside the cavity will be atmospheric (1 atm). Knowing the present differential pressure across the diaphragm and the constant atmospheric pressure inside the cavity, the present IOP is finally revealed from equation 2.19. When the pressures on either side of the diaphragm are equal, no deflection will occur. For a cavity pressure of 1 atm, an external pressure of 60 mmHg above

atmospheric is required to achieve the maximum diaphragm deflection of $0.5~\mu m$, according to equation 2.18. The pressure limits designed for the sensor and corresponding characteristics are listed in Table 2.3

Table 2.3 Pressure Limits and Characteristics

P _{ext} (IOP)	Plate Spacing	Capacitance	Natural Frequency
0 mmHg + 1 atm	1.5 μm	1.7 pF	136 MHz
60 mmHg + 1 atm	1.0 μm	2.55 pF	111 MHz

In summary, the natural frequency of the sensor is found by observing the voltage drop versus frequency profile for the external resistor. The instantaneous capacitance is then determined from the natural frequency using equation 2.10. The center deflection of the diaphragm is found from the parallel plate capacitor formula equation 2.17. Plugging the center deflection of the diaphragm into equation 2.18 then reveals the differential pressure across the diaphragm. With the pressure in the sensor cavity sealed with 1 atm, the instantaneous IOP level is finally known from equation 2.19. This system allows the constant monitoring of IOP without any inconvenience or discomfort to the patient. With constant monitoring, the patient can be alerted at the onset of dangerous IOP levels and seek treatment to reduce those levels, thus preventing the irreparable damage that could occur between visits to a physician. The constant monitoring will also provide valuable information as to what factors affect IOP.

2.4 Location of Implantation

As shown in Figure 2.15, the sensor will be implanted in the anterior chamber of the eye where IOP is maintained. To avoid interfering with the patient's vision, the sensor will be anchored between the iris and the comea at the side of the eye.

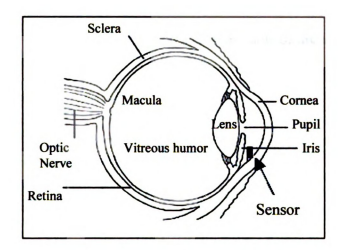


Figure 2.15 Sensor Location

Sutures threaded through the laser-drilled holes of the foot will provide that anchor. The sutures are 9-0 Vicryl with micro needles attached to their ends. The diameter of the sutures is 5 μ m, less than the diameter of a human hair. Due to the size of the sensor and the sutures, the operation will be performed under a dissecting microscope. Once in place, the sensor will be oriented so that the plane of the diaphragm is parallel to the plane of the vertical and tilted slightly at an angle towards the papillary axis. The aircore of the coupling between the internal and external inductors generally provides a loose coupling or low coupling coefficient seen in equation 2.12.

The proposed placement for the external circuit is affixed to the side of the patient's head near the eye by means of a patch. In order to have a distinguishable voltage drop across the external resistor at the natural frequency, it is desirable to

maximize the induced reactance, X_M , and hence the mutual inductance, M. As seen in equation 2.13, the mutual inductance is dependant upon the two inductor values and the coupling coefficient. While the inductor values are limited by the size of the sensor and external device, the coupling coefficient can be increased by reducing the distance between the inductors. This allows a greater flux to link the coils. Figure 2.16 shows the resonance curves for coupled circuits with different amounts of mutual inductance.

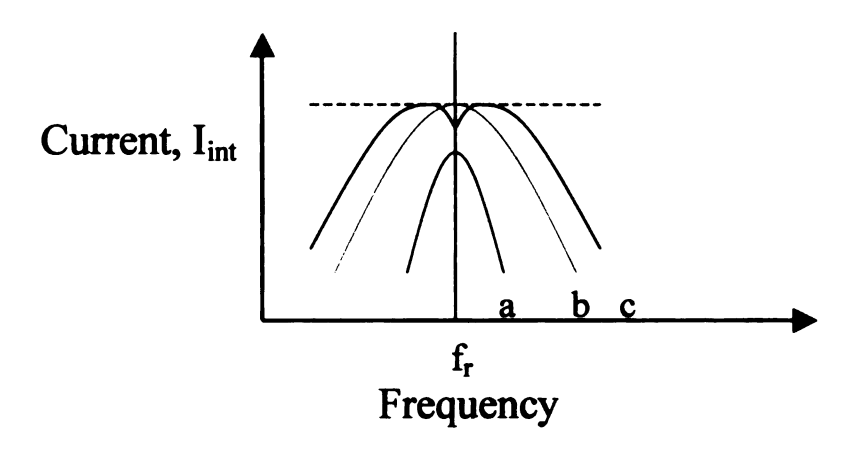


Figure 2.16 Resonance Curves for Coupled Circuits [5]

Curve a represents a coupling value below the critical level. Curve b represents a coupling value at the critical level, while curve c represents a coupling value above the critical level. When the coupling is below the critical value, the response will be very sensitive to changes in frequency but the coupling will be insufficient to produce the maximum signal in the internal circuit. If the coupling is increased until the critical value is reached, the maximum signal will occur at the natural frequency. If the coupling is increased past the critical value, the internal circuit will have a double resonance response [5]. The sensor will be positioned in the eye close to the surface, and its coils will be oriented parallel to those of the external inductor, thus permitting the maximum amount

of flux linkage. This will allow adequate coupling to produce a sufficient current in the internal circuit and induced reactance in the external circuit. The coupling limitations due to the proximity of the inductors and the air medium in which the flux is linked will ensure, however, that a double resonance response does not occur. A single resonant response is desired for ease of determining the sensor's natural frequency.

Chapter 3. Temperature and Pressure Considerations

3.1 Fabrication

The IOP sensor is designed to have a cavity pressure of 1 atm. This will ensure the sensor diaphragm does not deflect when placed in an equal ambient pressure. The anodic bonding process that seals the silicon wafer to the glass substrate typically occurs at the elevated temperature of 400°C [10]. If this bonding is performed at atmospheric pressure, the air in the cavity will contract as it cools to room temperature creating a sub-atmospheric cavity pressure. The pressure at which the anodic bonding takes place must therefore be considered. Modeling the cavity air as an ideal gas, it behaves according to the ideal gas law

$$PV = nR_u T (3.1)$$

where P is the pressure in atmospheres (atm), V is the volume in liters (L), n is the number of moles in kilomoles (kmol), R_u is the universal gas constant, $82.05 \frac{L \cdot atm}{kmol \cdot K}$, and T is the temperature in Kelvin (K) [11]. The conditions during bonding will be considered state 1 and the ambient conditions of body temperature (37°C = 310K) and 1 atm will be considered state 2 in this analysis. The universal gas constant will not change between states. In addition, the amount of air or number of moles will not change between states once the bonding has formed an airtight seal. The two states can then be related by

$$\frac{P_1 V_1}{T_1} = nR_u = \frac{P_2 V_2}{T_2} \tag{3.2}$$

The change in cavity volume as a result of contraction during the cooling to state 2 is 2.14E-11 L. Treating the volumes as equal, the ideal gas relation between the two states simplifies to

$$\frac{P_1}{T_1} = \frac{P_2}{T_2} \tag{3.3}$$

All of the conditions are known except for the ambient pressure during the bonding. Assuming a bonding temperature of 400°C (673K), the cavity should be sealed with air at 2.243 atm. The higher pressure in the cavity will be reduced to 1 atm once the air inside contracts as it cools to body temperature. This will ensure the correct cavity pressure that is required to accurately determine IOP.

3.2 RLC Considerations

3.2.1 Resistor Considerations

The equivalent circuit for the sensor contains a resistive element, R_{int} , to model the resistance of the inductor coils. The resistance of a conductor is given as

$$R = \rho \frac{L}{4} \tag{3.4}$$

where R is the resistance in Ω , ρ is the resistivity in Ω^*m , L is the length of the conductor in m, and A is the cross-sectional area of the conductor in m² [12]. Based on the dimensions of the inductor, the length is 88720 μ m. The cross-sectional area is the product of the line height, L_H, and line width, L_W, which equals 72 μ m². The resistivity of gold is dependant on its purity and processing. The value used in this analysis is 2.40E-8 Ω^*m [6]. The nominal resistance of the inductor is therefore 29.57 Ω .

Previously, the resistance of the internal inductor coil has been treated as a constant value. This is not entirely valid. As the frequency of the alternating current increases, the generated magnetic field and thus the current is concentrated closer to the conductor surface, as shown in Figure 3.1.

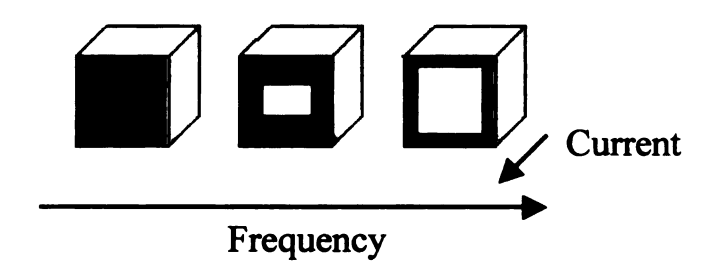


Figure 3.1 Effect of Frequency on Skin Depth [13]

The skin depth is defined as the distance from the metal surface beyond which the current density falls below 1/e (about 37%) of its original magnitude. Mathematically, the skin depth is expressed as

$$\delta = \sqrt{\frac{\rho}{\pi f \mu}} \tag{3.5}$$

where δ is the skin depth in m, ρ is the resistivity of the metal in Ω^*m , f is the frequency in Hz, and μ is the permeability of the metal in Henries/meter (H/m) [13]. The permeability of a material is its ratio of magnetic flux density to magnetic field strength,

$$\mu = \mu_0 \mu_r \tag{3.6}$$

where μ_0 is the permeability of free space ($\mu_0 = 4\pi E$ -7 H/m) and μ_T is the dimensionless relative permeability of the material [6]. The relative permeability of gold is 0.99996 [14]. The permeability of gold is therefore 1.26E-6 H/m. The skin depth as a function of frequency is plotted in Figure 3.2.

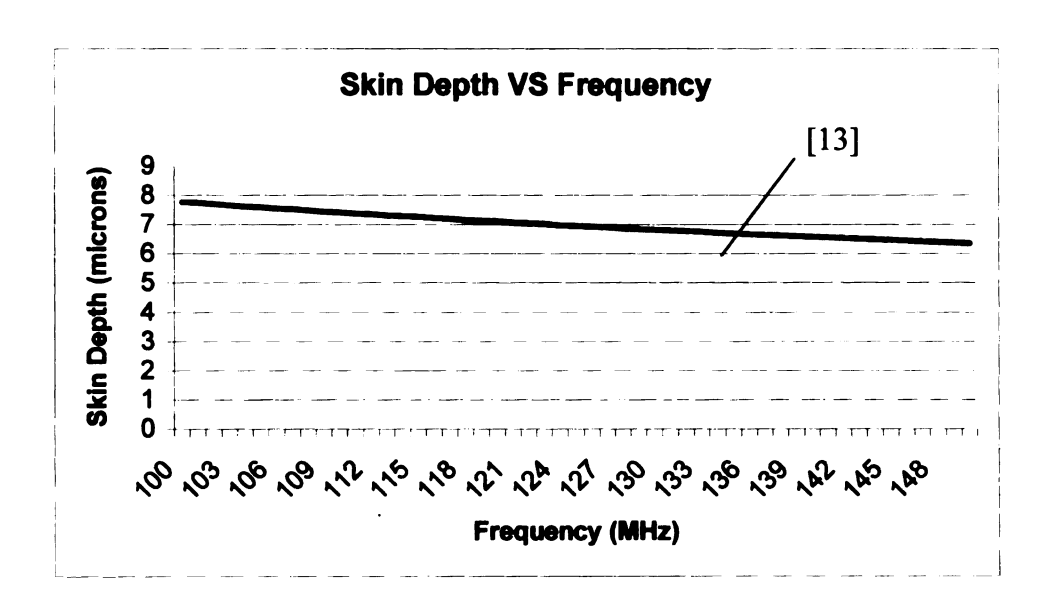


Figure 3.2 Skin Depth vs. Frequency

Figure 3.2 indicates that the skin depth never drops below half of the inductor line height, 4.5 µm. This does not mean that the skin effect is not present. This does show, however, that the current density in the inductor will not fall below 37% of its original magnitude anywhere in the coil.

The resistance of the inductor coil must now be revised to include the skin effect.

The reevaluated resistance for the inductor coil is given as

$$R(f) = \frac{\rho L_L}{L_W \delta \sqrt{1 - e^{-L_H/\delta}}}$$
(3.7)

where R(f) is the resistance in Ω , ρ is the resistivity in Ω^*m , L_L is the length of the inductor in m, L_W is the line width of the inductor in m, δ is the skin depth in m, and L_H is the line height of the inductor in m [15]. The resistance is dependant on the skin depth, more specifically the frequency of the alternating current. As the frequency increases,

the skin effect reduces the effective cross-sectional area of the inductor thus increasing the resistance. The resistance as a function of frequency is shown in Figure 3.3.

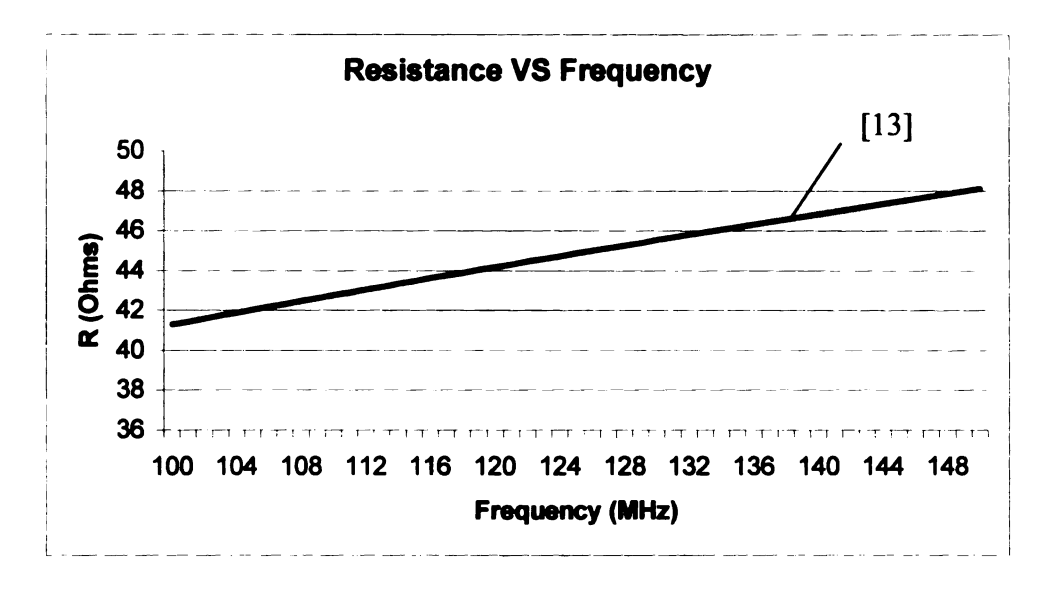


Figure 3.3 Resistance vs. Frequency

The frequency of the alternating current is not the only thing that affects the inductor coil resistance. The resistivity of most materials changes with temperature. For moderate temperature changes (0-100°C) and assuming only ρ varies significantly, the corresponding resistance change can be approximated by

$$R_T = R_o(1 + \alpha_R \Delta T) \tag{3.8}$$

where R_T is the temperature dependant resistance in Ω , R_0 is the known resistance measured at some reference temperature in Ω , α_R is the temperature coefficient of resistance (TCR) in ${}^{\circ}C^{-1}$, and ΔT is the difference between the actual and reference temperatures in ${}^{\circ}C$ [6]. A range of TCR values for gold can be found in handbooks. The TCR value used in this analysis is 0.0083 ${}^{\circ}C^{-1}$ [6]. Figure 3.4 demonstrates the dependence of resistance on temperature using 20°C as the reference temperature.

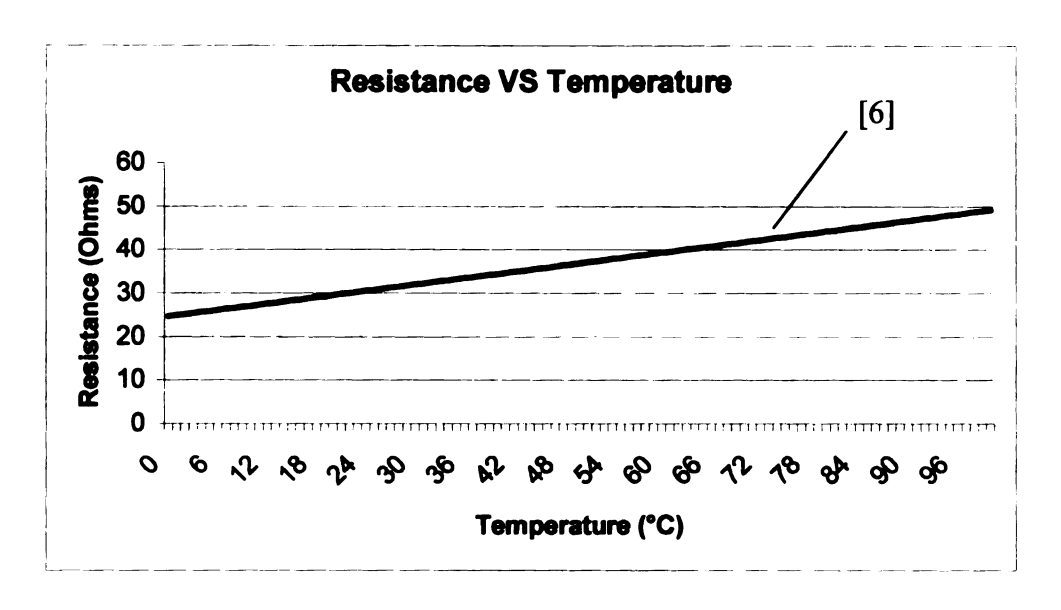


Figure 3.4 Resistance vs. Temperature

Combining the temperature and frequency dependence, the resistance as a function of temperature and frequency is given as

$$R_T(f) = \frac{\rho L_L}{L_W \delta \sqrt{1 - e^{-L_H/\delta}}} (1 + \alpha_R \Delta T)$$
(3.9)

While it is assumed that only ρ varies significantly in the R_T model, temperature changes will also affect the cross-sectional area of the inductor. Changes in the cross-sectional area will then affect the resistance according to equation 3.4. The change in a dimension of the coil as it changes with temperature can be described by

$$\Delta L = L_o \alpha_T \Delta T \tag{3.10}$$

where ΔL is the change in the dimension in m, L_0 is the original dimension in m, and α_T is the linear coefficient of thermal expansion (CTE) in ${}^{\circ}C^{-1}$ [6]. The new dimension of the inductor can then be found from

$$L = L_o(1 + \alpha_T \Delta T) \tag{3.11}$$

where L is the new dimension in m. The vertical expansion and contraction of the inductor coil is unrestricted by any other structures in the sensor. Therefore, the CTE of gold will be used when solving the line height for changes in temperature

$$L_{HT} = L_H \left(1 + \alpha_{A\mu} \Delta T \right) \tag{3.12}$$

where L_{HT} is the new line height in m. The CTE for gold, α_{Au} , that will be used in this analysis is 14.2E-6 °C⁻¹ [6]. Equation 3.11 can also be used to describe the change in line width with temperature. While the top surface is unconstrained, the base of the thin coil is attached to the bulk glass substrate and is therefore restricted by its motion. The width at the top of the coil will be described by equation 3.11 using the CTE for gold. The width at the base of the coil will be described by the same equation using the CTE for the glass. The CTE for glass, α_{7740} , that will be used in this analysis is 3.25E-6 °C⁻¹ [16]. Assuming the line width varies linearly over the 9 μ m height between top and bottom surfaces, the average line width is given as

$$L_{WT} = \frac{L_W}{2} (2 + \Delta T [\alpha_{Au} + \alpha_{7740}])$$
 (3.13)

where L_{WT} is the new, average line width in m. Figure 3.5 shows how the line width varies over the coil line height for different temperatures.

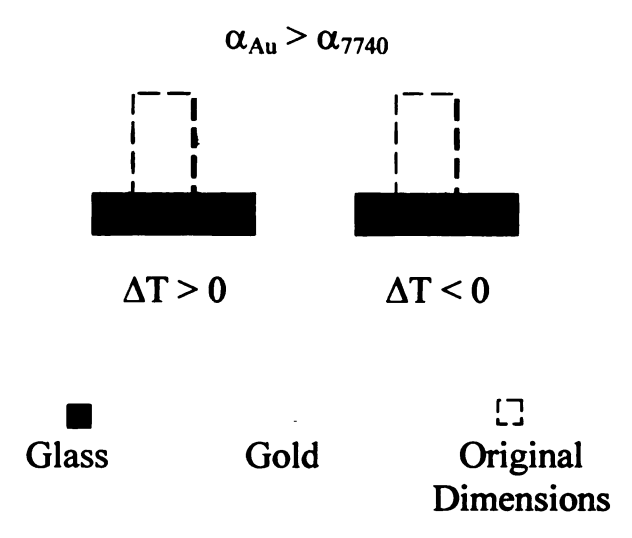


Figure 3.5 Line Width Variation of Coil for Different Temperatures

The overall length of the inductor will face the same set of constraints as the line width.

The length of the inductor as it changes with temperature follows the modified version of equation 3.13

$$L_{LT} = \frac{L_L}{2} (2 + \Delta T [\alpha_{Au} + \alpha_{7740}])$$
 (3.14)

where L_{LT} is the new inductor length in m, and L_{L} is the original length in m. By incorporating equations 3.14, 3.13, and 3.12 into equation 3.4, the resistance as a function of the CTEs for gold and glass is given as

$$R(CTE) = \rho \frac{L_{LT}}{L_{HT}L_{WT}} \tag{3.15}$$

where R(CTE) is the new resistance in Ω . Figure 3.6 shows the variation of R(CTE) with temperature.

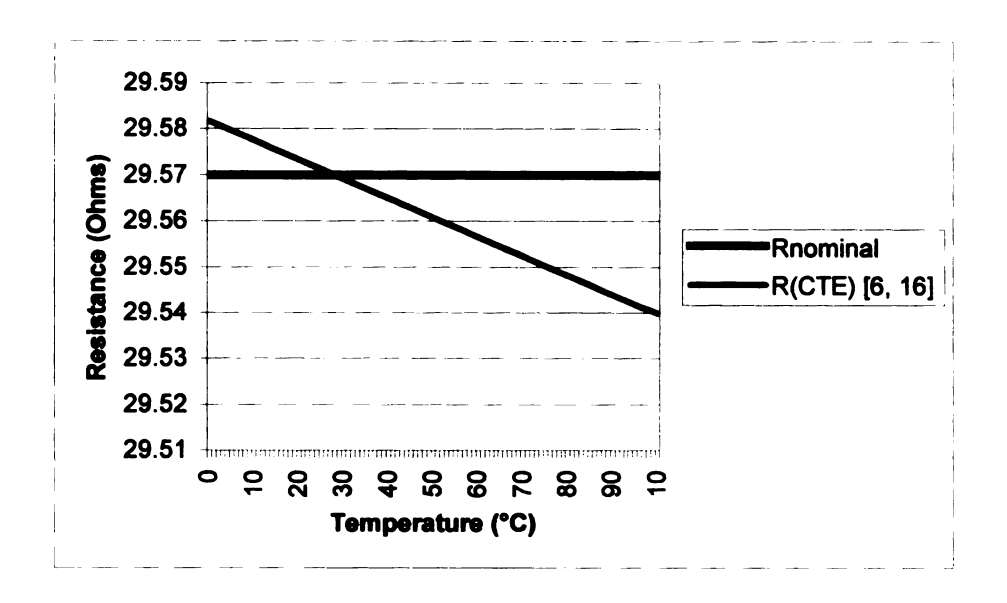


Figure 3.6 R(CTE) vs. Temperature

The reason for the decreasing resistance in Figure 3.6 is the increasing cross-sectional area of the coil with temperature. However, the resistance, R(CTE), is not very sensitive to changes in temperature. The sensitivity of R(CTE) is $-4.196E-4 \Omega/^{\circ}C$. The change in resistance due to the CTE, TCR, and a combination of both can be seen in Figure 3.7.

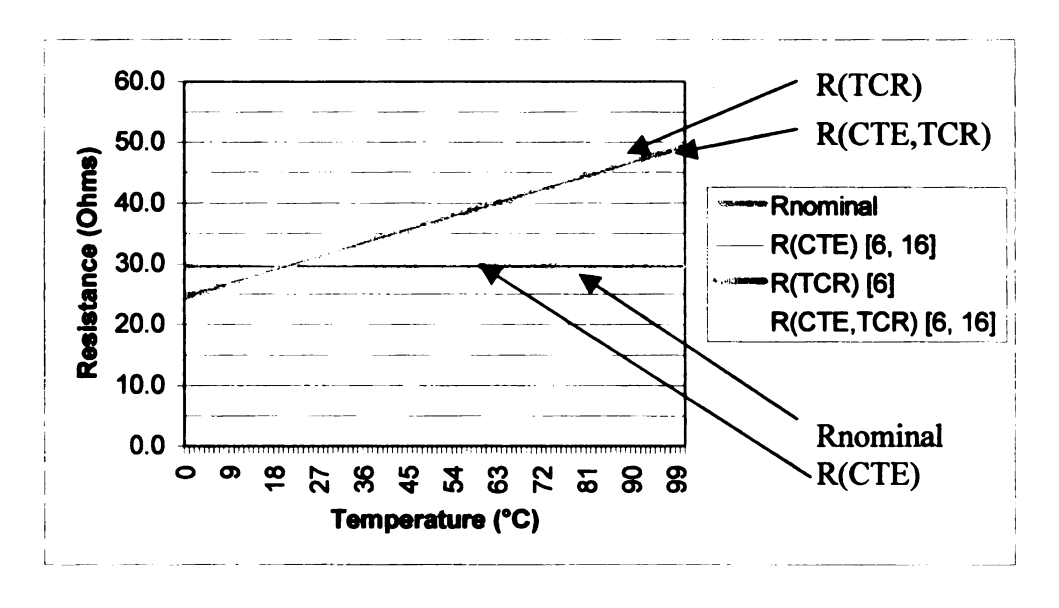


Figure 3.7 Resistance Variations with Temperature

It is evident from Figure 3.7 that the resistance R(TCR) is much more sensitive to changes in temperature than R(CTE). Furthermore, there is an insignificant difference in

sensitivities between R(TCR) and R(CTE,TCR). The sensitivities for the different models are listed in Table 3.1.

Table 3.1 Sensitivities of Resistor models

Sensitivity (Ω/°C)	
-4.196E-4	
2.448E-1	
2.454E-1	

Upon reviewing Table 3.1, the effects of thermal expansion and contraction on the coil resistance can be neglected. The model for the inductor resistance will incorporate the skin effect and the TCR, given in equation 3.9 as

$$R_T(f) = \frac{\rho L_L}{L_W \delta \sqrt{1 - e^{-L_H/\delta}}} (1 + \alpha_R \Delta T)$$

It has been shown that the inductor resistance is not a constant value, as it was treated while describing how the IOP monitoring system works in section 2.3. Rather, it is a function of frequency and temperature. When the internal circuit is at the natural frequency, Z_{int} will be at a minimum. According to equation 2.11, the current flowing in the circuit will therefore be at a maximum. The magnitude of the peak current is dependent upon the resistance so that the height and slope of the peak of the curve increases as the resistance is reduced and vice versa [5]. This effect is illustrated in Figure 3.8.

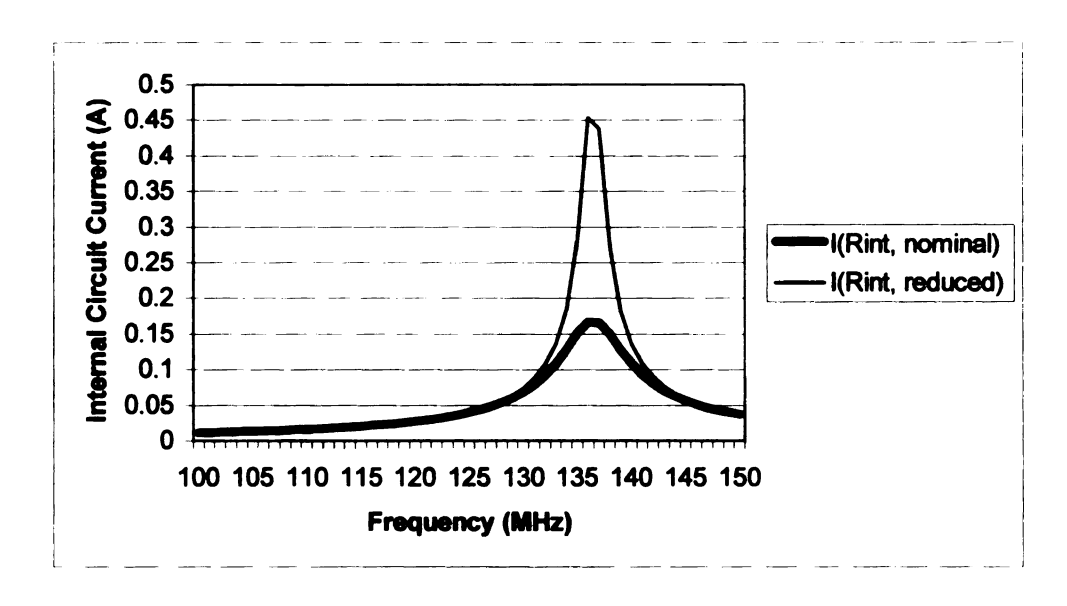


Figure 3.8 Resistance Change on Internal Peak Current Curve

When the current is maximized, the voltage drop across R_{int} will also be maximized. The resistance affects the curve of the voltage drop in the same way. This is shown in Figure 3.9.

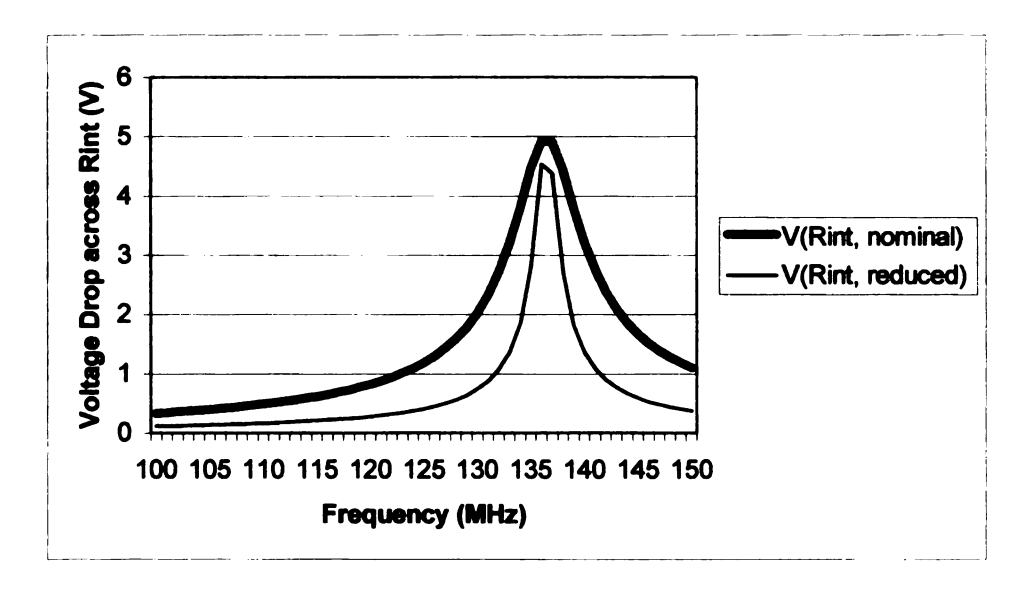


Figure 3.9 Resistance Change on Internal Voltage Curve

The effect on current and voltage curves due to changes in R_{int} also carries over to the external circuit. At the natural frequency Z_{ext} will be maximized. Therefore, the current in the external circuit will be minimized as shown in Figure 3.10.

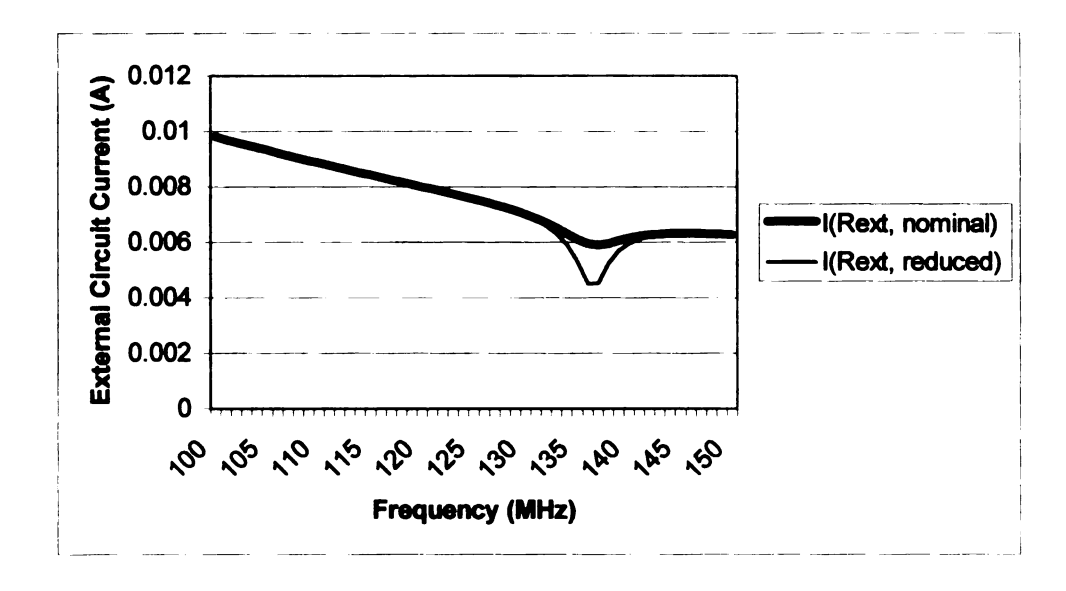


Figure 3.10 Resistance Change on External Peak Current Curve

With the external current minimized and the induced reactance, X_M , maximized at the natural frequency, the voltage drop across R_{ext} will therefore be minimized as well. This is illustrated in Figure 3.11.

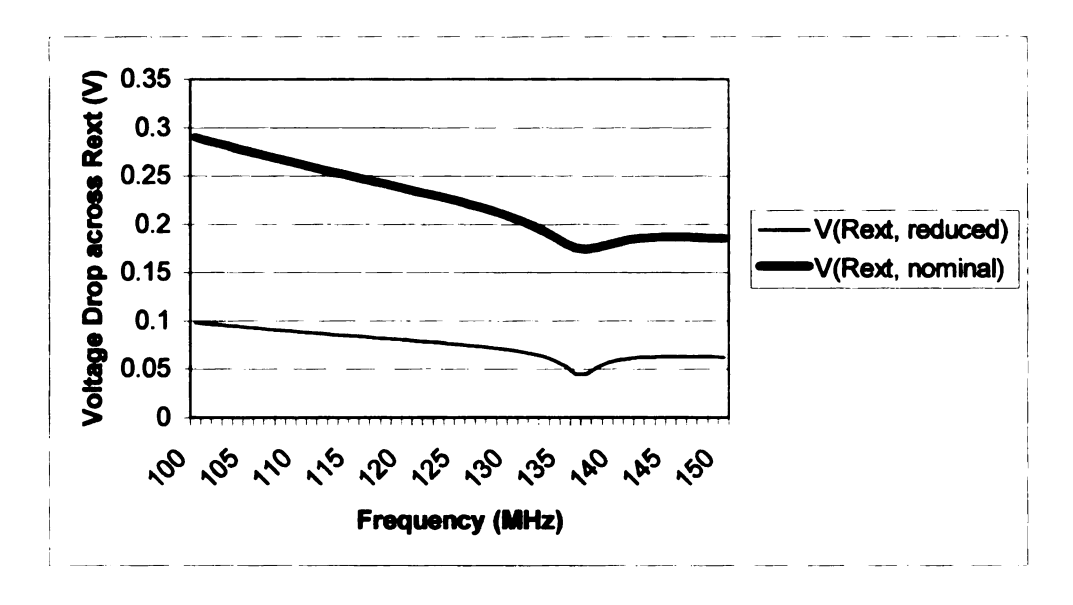


Figure 3.11 Resistance Change on External Voltage Curve

Resistance changes of R_{int} will affect the IOP monitoring system in another way.

The changing resistance values will affect the amplitudes of the resistor vector and its corresponding voltage drop, but the phases will not change, as can be seen in Figure 2.9. These changing resistance values will, however, affect the phase angle between the current and impressed voltage for the internal circuit [15]. This is apparent from the phasor diagram in Figure 2.10. From equation 2.7 it is clear that the capacitive and inductive reactance will cancel out at the natural frequency. This will result in a phase lag of 0° between the current and impressed voltage for the internal circuit. Figure 3.12 shows that the current and voltage are in phase for several capacitance values and corresponding natural frequencies.

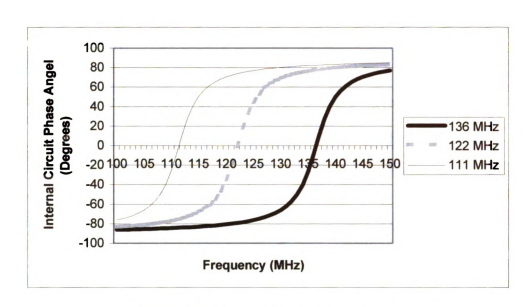


Figure 3.12 Internal Circuit Phase Angle

For non-zero phase angles, changes in $R_{\rm int}$ will affect the slope of the phase curve such that the slope of the phase curve increases as the resistance is reduced and vice versa. This effect is illustrated in Figure 3.13.

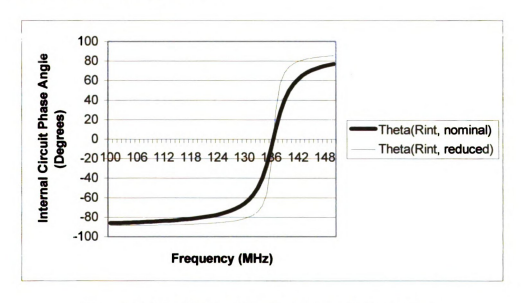


Figure 3.13 Resistance Change on Internal Phase Curve

The phase angle between the current and impressed voltage in the external circuit is given

as

$$\phi = \tan^{-1} \left(\frac{X_{Lext} + X_M}{R_{ext}} \right) \tag{3.16}$$

At the natural frequency, the sum of the induced and inductive reactance is locally maximized causing a spike in the phase curve. This can be seen in Figure 3.14.

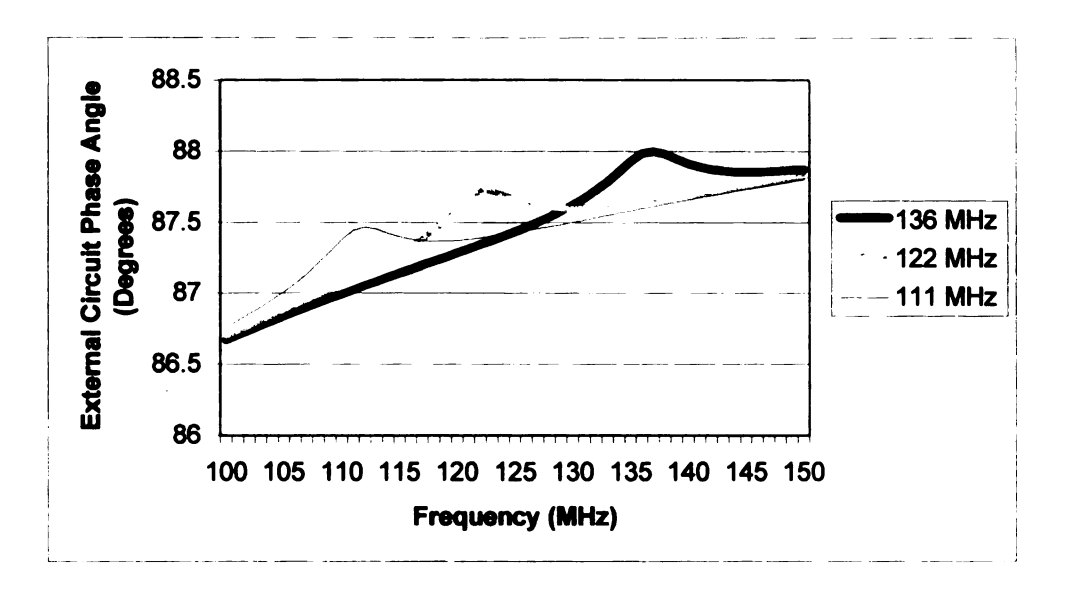


Figure 3.14 External Circuit Phase Angle

Changes in R_{int} will affect the phase curve by shifting it vertically positive and increasing the slope of the spike as the resistance is reduced. This effect is illustrated in Figure 3.15.

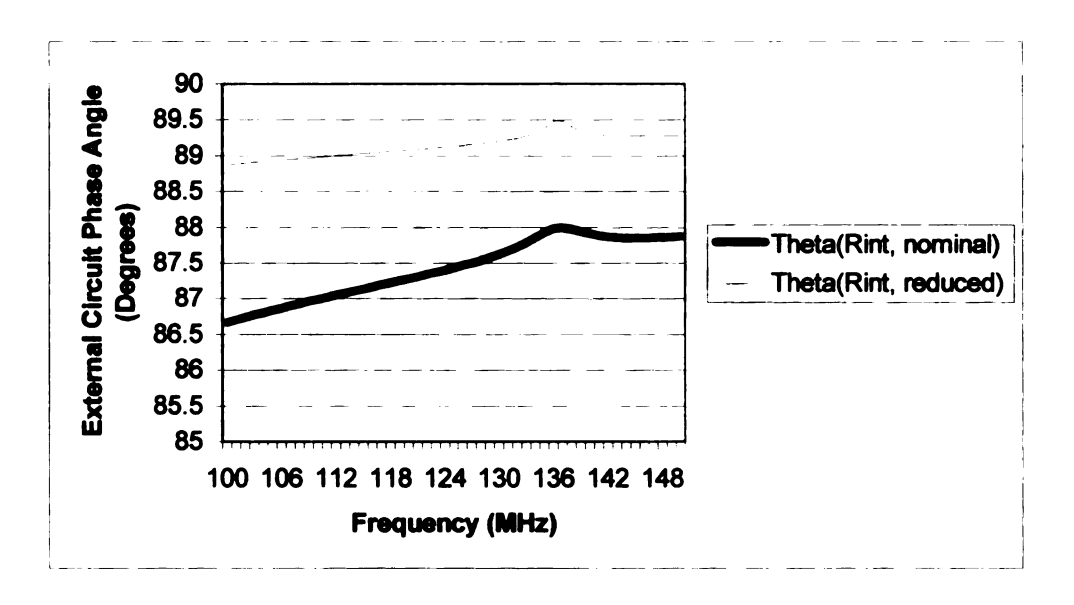


Figure 3.15 Resistance Change on External Phase Curve

This section has shown the changes that will occur to the internal inductor's resistance value and how those changes will manifest themselves in the system as a whole. The system can be calibrated to account for resistance changes due to the skin effect. Resistance changes due to the inductor coil's TCR can be detected by observing the voltage drop across R_{ext}, the current through R_{ext}, or alternatively by observing the phase of the external circuit. If these changes are small, they may be neglected or the system may be calibrated for accuracy. If these changes are significant, the IOP sensor will have the added ability to remotely monitor temperature as well as pressure.

An additional resistor consideration is the power in that sensor component. The power in the components of an RLC circuit is shown in Figure 3.16.

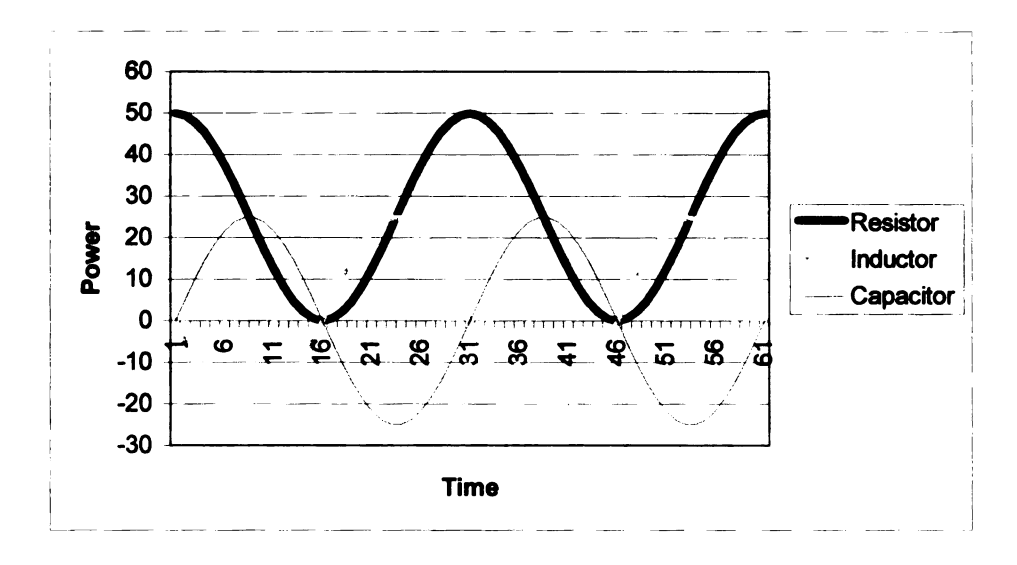


Figure 3.16 Instantaneous Power in Internal Circuit

Ideal inductors and capacitors are passive components having a zero average power. The power in those elements is 180° out of phase, and they merely exchange their electrical energy much like the transfer of kinetic and potential energy in a mechanical system. Resistors, however, have a positive average power. Resistors transfer electrical energy out of the circuit in the form of heat. This is analogous to damping or friction in a mechanical system.

A more convenient way to express the heating effect of resistors is to use the average or root mean square (rms) power given as

$$P_{rms} = \frac{V_R I_R}{2} \tag{3.17}$$

where P_{rms} is the average power in watts (W), V_R is the maximum amplitude of the voltage across the resistor in V, and I_R is the maximum amplitude of the current through the resistor in A [5]. By substituting $V_R = I_R R$ and $I_R = I_o = \frac{V_o}{Z}$ into equation 3.17, the rms power can also be expressed as

$$P_{rms} = \frac{{V_o}^2}{2Z^2}R\tag{3.18}$$

Neglecting temperature changes and the skin effect, P_{rms} will reach a maximum at the natural frequency when the inductive and capacitive reactance cancels out. The changing capacitance due to the deflection of the sensor diaphragm will therefore shift the frequency where the maximum P_{rms} occurs but not the maximum value itself. This is shown in Figure 3.17.

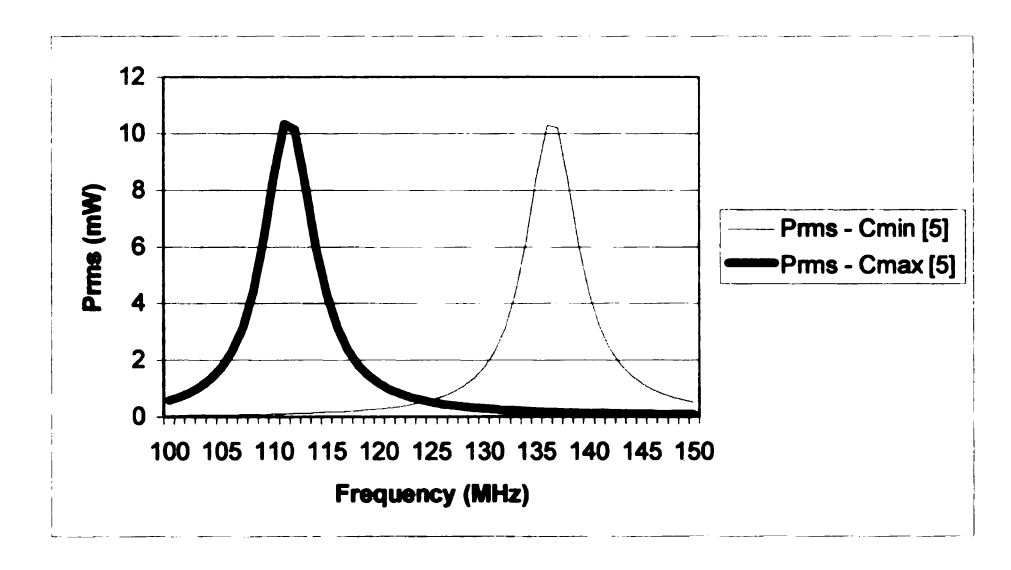


Figure 3.17 P_{rms} in Internal Circuit

A final resistor consideration is thermal noise. In any conducting material whose temperature is above absolute zero (0 K), the random motion of charge carriers in that conductor produces random currents and voltages. These currents and voltages produce noise. As the temperature of the conductor increases, the random motion of the charge carriers increases, hence increasing the noise voltage. Neglecting the skin effect, the noise voltage in the coil windings is given by

$$V_N = \sqrt{4kTR_T B} \tag{3.19}$$

where V_N is the rms noise voltage in V, k is Boltzmann's constant (1.38E-23 Joules/K), V_N is the absolute temperature in V_N is the temperature dependent resistance in V_N , and V_N is the bandwidth in Hz [17]. The estimated natural frequency range for the sensor is 111-136 MHz. A frequency sweep of roughly 100-150 MHz will therefore be employed to include the complete voltage profiles produced at these frequencies. This corresponds to an effective bandwidth of 50 MHz to determine the noise voltage shown in Figure 3.18.

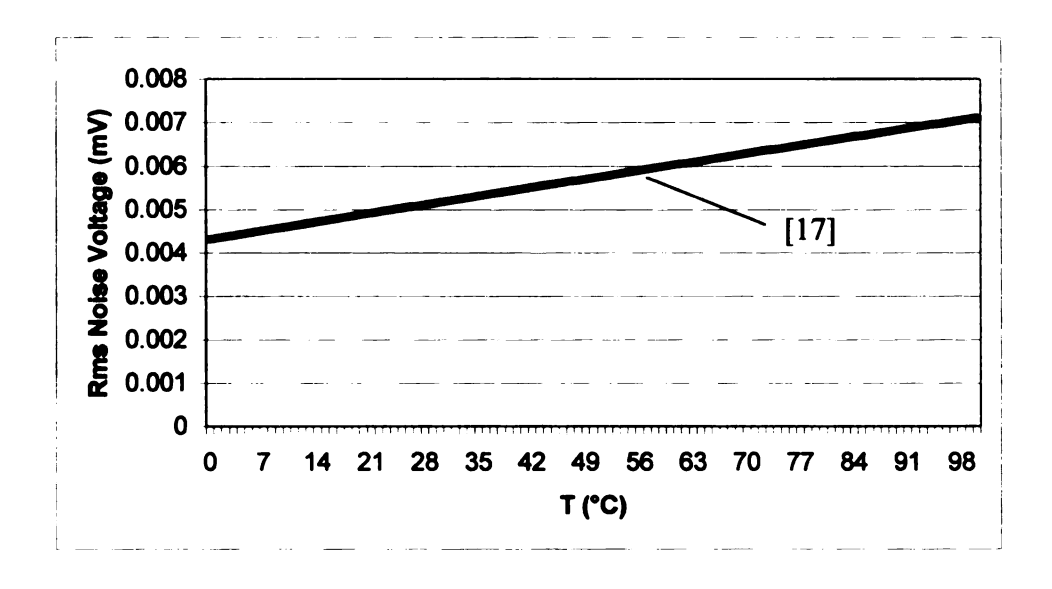


Figure 3.18 Thermal Noise vs. Temperature

When the sensor is at the human body temperature (37°C), an rms noise voltage of 0.0054 mV will be present. This seems like a relatively small value but it must be compared to the signal to be measured from the external circuit. In order to determine the sensor's natural frequency from the external circuit, the voltage drop profile across

R_{ext} must exhibit a significant dip at that frequency. The dip will be defined as the difference between the local maximum and minimum voltages as shown in Figure 3.19.

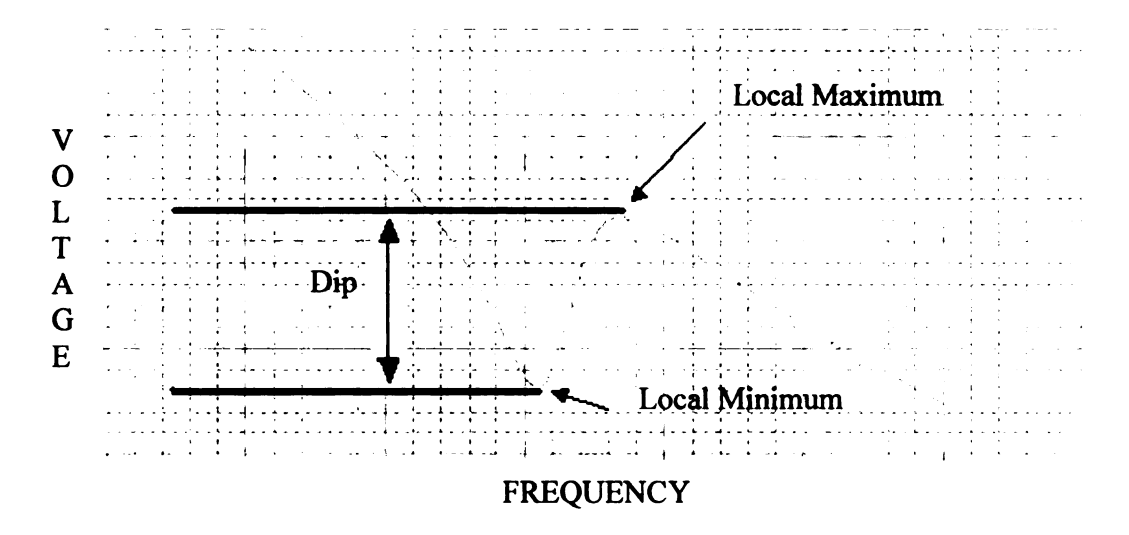


Figure 3.19 Dip Measurement from Rext Voltage Profile

The voltage dip obtained from a Pspice simulation at body temperature has a value of 160.2 mV. Comparing this to the corresponding noise voltage, a signal to noise ratio (SNR) of 57,302 will exist. As the temperature of the sensor increases, the noise voltage will increase and the temperature dependent resistance will increase causing a smaller dip in the voltage profile. However, even at extreme temperatures the SNR remains considerably >>1 to allow sensor natural frequency readings from the external circuit.

Noise must still be considered in the external circuit. If thermal noise presents a problem outside the sensor, a tracking program may be incorporated to reduce the required frequency sweep range and hence the bandwidth, reducing the noise.

3.2.2 Inductor Considerations

Initially the sensor was treated as a three-component RLC circuit. The capacitor element models the capacitance between the flexible diaphragm and the fixed, gold

electrode. The gold coil inductor is modeled by the inductor element and its series resistance is accounted for by the resistor element. However, additional capacitance will be present in the circuit due to the nature of the coil and the design of the sensor. In creating the flexible diaphragm, a 3.5 µm recess is etched in the bottom surface of the silicon wafer. The doping process used to create the diaphragm is then applied to the 1.2 mm x 1.2 mm area of the recess. This makes the entire recess area including the diaphragm conductive. When the silicon wafer is bonded to the glass substrate, a capacitance will be formed between the recess area and the top face of the inductor. The recess area outside of the diaphragm will not be flexible, creating a fixed, parallel plate capacitor. Referring to equation 2.17, the capacitance between the inductor and the recess can be given as

$$C_{Si-L} = \frac{\varepsilon_o \varepsilon_r L_L L_W}{d_{Si-L}} \tag{3.20}$$

where d_{Si-L} is the spacing between the recess plane and the top face of the inductor in m. The top face of the inductor is 1 μ m below the top face of the glass substrate providing a d_{Si-L} of 4.5 μ m. Therefore, C_{Si-L} has a capacitance of 1.396 pF. Additional line-to-line capacitance will also be present between the windings of the coil. This capacitance cannot be modeled as a parallel plate capacitor because of the continuous voltage drop across the length of the inductor. The line-to-line capacitance for a single level, square spiral inductor can be approximated by

$$C_{L-L} = \varepsilon_0 \varepsilon_{7740} L_L \left[\frac{L_H}{s} \left(\frac{L_H + 2h}{L_H + 2h + 0.5s} \right)^{0.695} + \left(\frac{L_W}{L_W + 0.8s} \right)^{1.4148} \right] + 0.831 \left(\frac{L_H + 2h}{L_W + 0.8s} \right)^{0.804}$$

$$(3.21)$$

where ε_{7740} is the dielectric constant of the substrate in F/m, s is the line spacing in m, and h is the height of the substrate in m [18]. The dielectric constant of the glass substrate is 44.25 pF/m [19]. The height of the glass substrate under the coils is 0.49 mm providing a self-capacitance of 0.125 fF for the inductor. The self-capacitance of the inductor and the inductor-recess capacitance will be in parallel with diaphragm-electrode capacitance as shown in Figure 3.20.

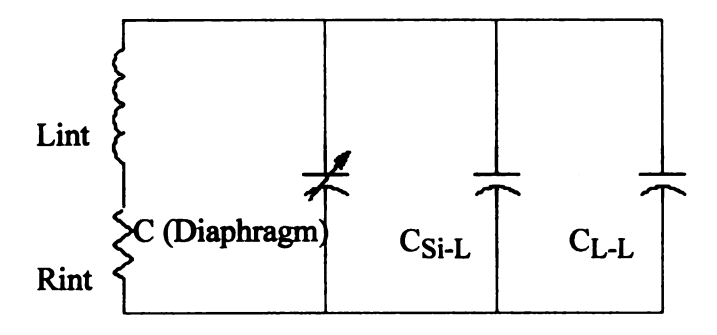


Figure 3.20 Sensor Equivalent Circuit Showing Additional Capacitance

The equivalent capacitance for the sensor can be found by summing all three capacitive

 $Ceq = C + C_{Si-I} + C_{I-I}$ (3.22)

elements

According to equation 2.10, the increased capacitance will reduce the natural frequency of the sensor. This will benefit the system's function by lowering the frequency operating range and reducing the skin effect according to equations 3.5 and 3.7.

However, the system will have to be calibrated to obtain the correct relationship between IOP and the sensor's natural frequency. The additional capacitance values and their effect on the natural frequency range are listed in Table 3.2

Table 3.2 Additional Capacitance Effects on Natural Frequency Range

Original Model	С			C _{eq}	f _r Range (MHz)
		1.7 – 2.55 pF		1.7 – 2.55 pF	111 – 136
	С	C _{Si-L}	C _{L-L}	C _{eq}	89.56 –
New Model	1.7 – 2.55 pF	1.396 pF	0.125 fF	3.096 – 3.946 pF	101.11

The inductive reactance in equation 2.4 provides the reactance of an ideal inductor. However, the reactance of a practical inductor will increase with frequency only to a certain point. At this point, the self-resonant frequency of the inductor, the inductor begins to look like a capacitor and the reactance rapidly drops to zero. The self-resonant frequency is dependent upon the resistance of the inductor coil as well as the distributed capacitance between the windings of the coil. This frequency can be given in terms of the sensor as

$$f_{rL} = \frac{1}{2\pi\sqrt{L_{\text{int}}C_{L-L}}} \tag{3.23}$$

where f_{rL} is the self-resonant frequency of the inductor in Hz [17]. The behavior of practical inductor reactance can be illustrated by introducing a figure of merit, Q, used to express the quality of an inductor. The Q of an inductor is the ratio of its reactance to

resistance. A high Q means that little electric energy is lost to resistive heating. The Q of a practical inductor in terms of the sensor can be expressed as

$$Q = \frac{\omega L_{\text{int}}}{R_{\text{int}}} \left[1 - \left(\frac{f}{f_{rL}} \right)^2 \right]$$
 (3.24)

where f is the frequency of interest in Hz [13]. This expression is valid for all non-zero frequencies up to the self-resonant frequency, after which the Q is zero. This is illustrated in Figure 3.21.

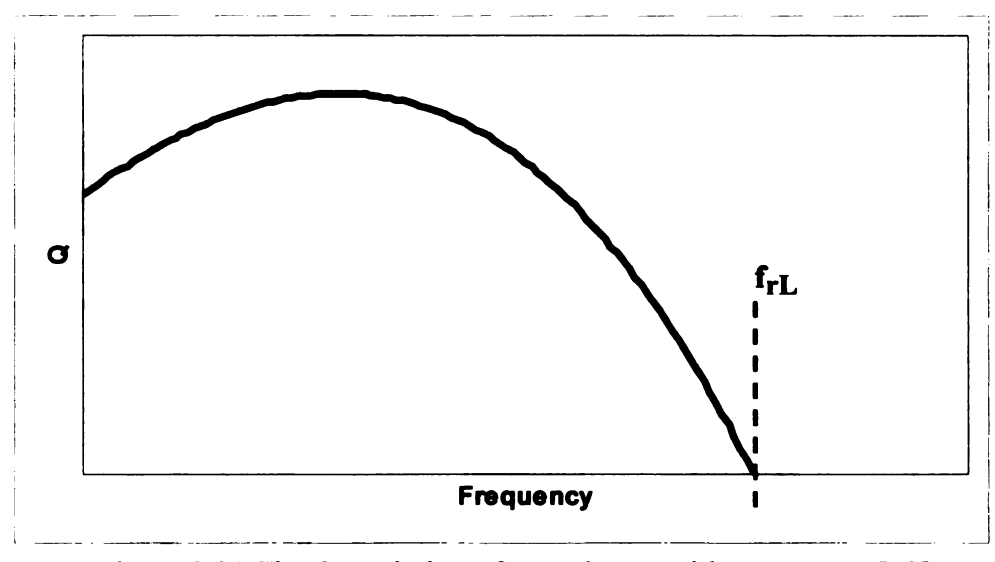


Figure 3.21 The Q Variation of an Inductor with Frequency [13]

The curve in Figure 3.21 begins by increasing with frequency, as the resistance in the coil windings is relatively small. As the frequency is further increased, the skin effect becomes more prominent. The increased resistance combined with the capacitance of the windings of the coil degrade the quality of the inductor to zero at its self-resonant frequency. In order to maintain a high Q of the inductor, the frequency of operation for the sensor must be kept well below the self-resonant frequency of the inductor. More importantly, the determination of IOP is based on the reactance of an ideal inductor. To obtain accurate readings from the sensor, the frequency of operation must be kept well

below f_{rL} where the behavior of a practical inductor follows that of an ideal one. The self-resonant frequency of the inductor is listed in Table 3.3 for comparison with operating frequencies of the sensor.

Table 3.3 f_{rL}, Operating Range of the Sensor

Sens	Sensor Operating Range (MHz)		
Original	111 - 136	1.59	
New	89.56 – 101.11	1.37	

From Table 3.3 it is evident that the original sensor operating range as well as the new range, accounting for additional sensor capacitance, is much lower than the self-resonant frequency of the inductor. Therefore, the sensor coil can be modeled as an ideal inductor to accurately determine IOP.

The expression used to determine the value of the inductor in [4] is given as

$$L_{MON} = \beta d_{OUT}^{\alpha 1} w^{\alpha 2} d_{AVG}^{\alpha 3} n^{\alpha 4} s^{\alpha 5}$$
(3.25)

where L_{MON} is the inductance in H, d_{OUT} is the outer spiral diameter in μm , d_{AVG} is the average spiral diameter in μm , n is the number of turns, s is the line spacing in μm , β and α are layout dependent coefficients provided by [20]. Figure 3.22 and Table 3.4 provide the inductor layout and the values used in equation 3.25, respectively.

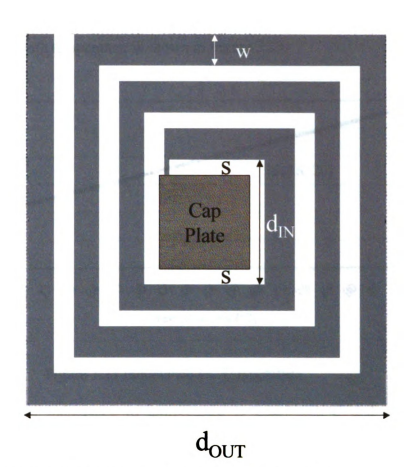


Figure 3.22 Layout for a Square Spiral Inductor [4]

Table 3.4 Inductance Equation Parameters

β	α1	α2	α3	α4	α5
0.00162	-1.21	-0.147	2.4	1.78	-0.03
d _{OUT}	d _{IN}	d _{AVG}	w	n	s
1161 μm	545 μm	853 μm	4 μm	26	4 μm

Some of the parameters in equation 3.25, namely $d_{\rm OUT}$, $d_{\rm AVG}$, w and s, are dependant on the inductor dimensions that will change with temperature. Under the same assumptions

made in section 3.2.1 regarding the behavior and constraints for the inductor, the changing inductance with temperature is shown in Figure 3.23.

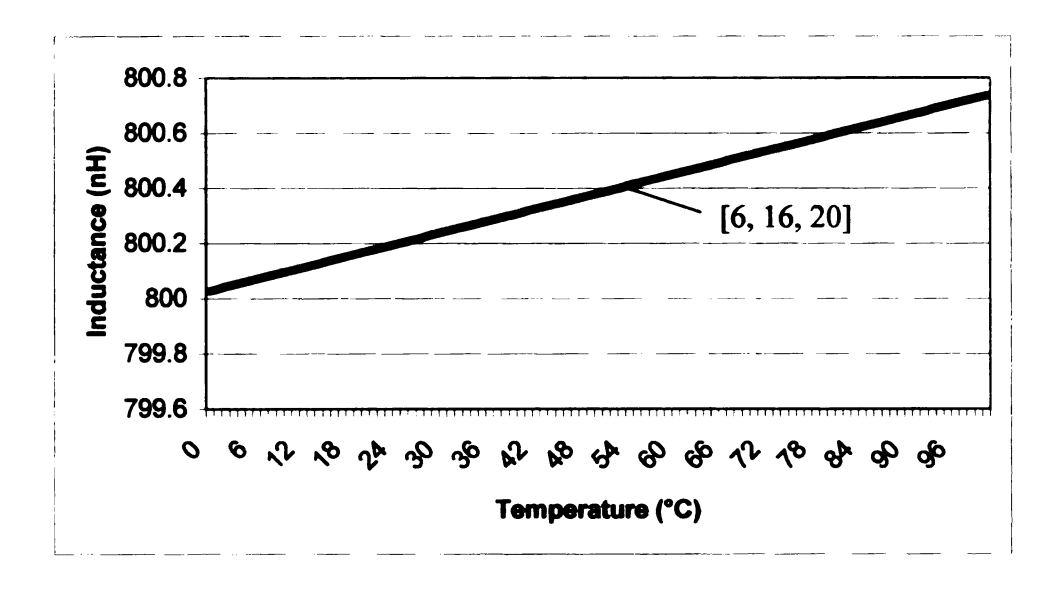


Figure 3.23 Inductance vs. Temperature

The sensitivity of the inductance to temperature is 0.007 nH/°C and is therefore negligible.

3.2.3 Capacitor Considerations

In designing the IOP sensor, the capacitance created by the flexible diaphragm and fixed electrode was modeled as a parallel plate capacitor. However, this model may not be the most accurate for determining the center deflection of the diaphragm from the capacitance. The parallel plate model treats the electrodes as two rigid plates parallel at a distance. In the case of the sensor, the top plate is not rigid and the center deflects from its fixed edges creating a non-uniform spacing between the plates. Other capacitor models should be considered to determine the center diaphragm deflection from the capacitance.

One option is to model the diaphragm as two rigid plates hinged together and at the edges as shown in Figure 3.24.

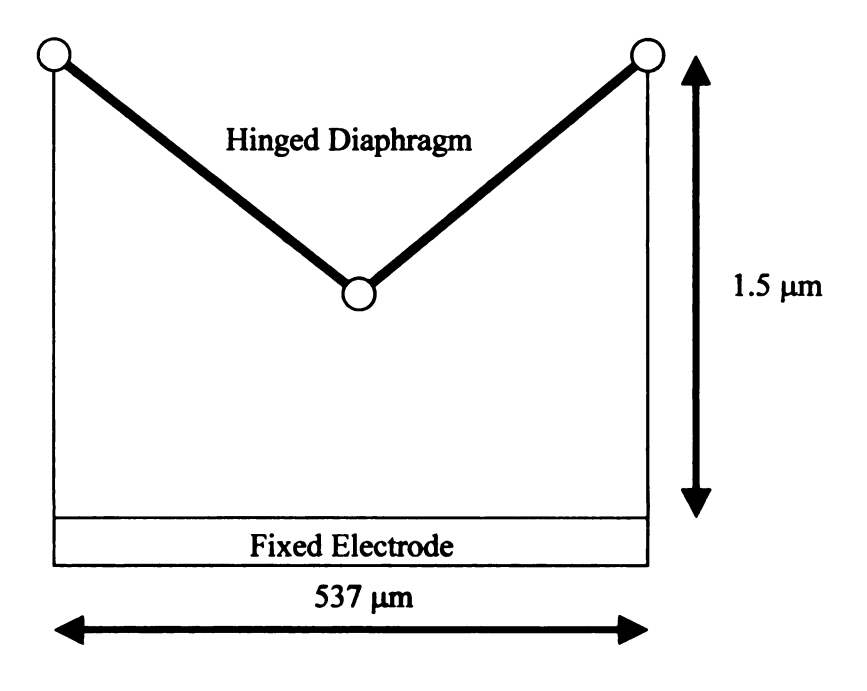


Figure 3.24 Hinged Plate Capacitor Model

The capacitance for this model can be derived by examining one of the hinged plates.

Figure 3.25 shows the schematic for deriving the capacitance.

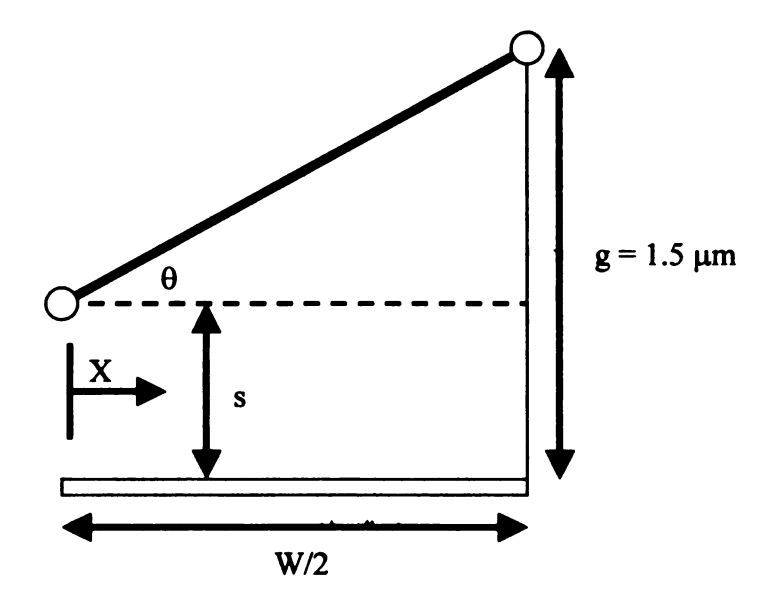


Figure 3.25 Capacitance Derivation Schematic

Half of the hinged plate capacitance, C_{HP}, can be derived as

$$\frac{1}{2}C_{HP} = \int_{0}^{\frac{W}{2}} dC(x) = \int_{0}^{\frac{W}{2}} \varepsilon_{o}\varepsilon_{r} \frac{W}{s + x \tan \theta} dx = \varepsilon_{o}\varepsilon_{r}W \int_{0}^{\frac{W}{2}} \frac{dx}{s + x \tan \theta} = \frac{\varepsilon_{o}\varepsilon_{r}W}{\tan \theta} \left[\ln(s + x \tan \theta) \right]_{0}^{\frac{W}{2}} = \frac{\varepsilon_{o}\varepsilon_{r}W}{\tan \theta} \left[\ln(s + \frac{W}{2} \tan \theta) - \ln(s) \right] = \frac{\varepsilon_{o}\varepsilon_{r}W}{\tan \theta} \left[\ln\left(\frac{s + \frac{W}{2} \tan \theta}{s}\right) \right] = \frac{\varepsilon_{o}\varepsilon_{r}W}{\tan \theta} \left[\ln\left(\frac{s + \frac{W}{2} \tan \theta}{s}\right) \right] = \frac{\varepsilon_{o}\varepsilon_{r}W}{\tan \theta} \left[\ln\left(\frac{s + \frac{W}{2} \tan \theta}{s}\right) \right] = \frac{\varepsilon_{o}\varepsilon_{r}W}{\tan \theta} \left[\ln\left(\frac{s + \frac{W}{2} \tan \theta}{s}\right) \right] = \frac{\varepsilon_{o}\varepsilon_{r}W}{\tan \theta} \left[\ln\left(\frac{s + \frac{W}{2} \tan \theta}{s}\right) \right] = \frac{\varepsilon_{o}\varepsilon_{r}W}{\tan \theta} \left[\ln\left(\frac{s + \frac{W}{2} \tan \theta}{s}\right) \right] = \frac{\varepsilon_{o}\varepsilon_{r}W}{\tan \theta} \left[\ln\left(\frac{s + \frac{W}{2} \tan \theta}{s}\right) \right] = \frac{\varepsilon_{o}\varepsilon_{r}W}{\tan \theta} \left[\ln\left(\frac{s + \frac{W}{2} \tan \theta}{s}\right) \right] = \frac{\varepsilon_{o}\varepsilon_{r}W}{\tan \theta} \left[\ln\left(\frac{s + \frac{W}{2} \tan \theta}{s}\right) \right] = \frac{\varepsilon_{o}\varepsilon_{r}W}{\tan \theta} \left[\ln\left(\frac{s + \frac{W}{2} \tan \theta}{s}\right) \right] = \frac{\varepsilon_{o}\varepsilon_{r}W}{\tan \theta} \left[\ln\left(\frac{s + \frac{W}{2} \tan \theta}{s}\right) \right] = \frac{\varepsilon_{o}\varepsilon_{r}W}{\tan \theta} \left[\ln\left(\frac{s + \frac{W}{2} \tan \theta}{s}\right) \right] = \frac{\varepsilon_{o}\varepsilon_{r}W}{\tan \theta} \left[\ln\left(\frac{s + \frac{W}{2} \tan \theta}{s}\right) \right] = \frac{\varepsilon_{o}\varepsilon_{r}W}{\tan \theta} \left[\ln\left(\frac{s + \frac{W}{2} \tan \theta}{s}\right) \right] = \frac{\varepsilon_{o}\varepsilon_{r}W}{\tan \theta} \left[\ln\left(\frac{s + \frac{W}{2} \tan \theta}{s}\right) \right] = \frac{\varepsilon_{o}\varepsilon_{r}W}{\tan \theta} \left[\ln\left(\frac{s + \frac{W}{2} \tan \theta}{s}\right) \right] = \frac{\varepsilon_{o}\varepsilon_{r}W}{\tan \theta} \left[\ln\left(\frac{s + \frac{W}{2} \tan \theta}{s}\right) \right] = \frac{\varepsilon_{o}\varepsilon_{r}W}{\tan \theta} \left[\ln\left(\frac{s + \frac{W}{2} \tan \theta}{s}\right) \right] = \frac{\varepsilon_{o}\varepsilon_{r}W}{\tan \theta} \left[\ln\left(\frac{s + \frac{W}{2} \tan \theta}{s}\right) \right] = \frac{\varepsilon_{o}\varepsilon_{r}W}{\tan \theta} \left[\ln\left(\frac{s + \frac{W}{2} \tan \theta}{s}\right) \right] = \frac{\varepsilon_{o}\varepsilon_{r}W}{\tan \theta} \left[\ln\left(\frac{s + \frac{W}{2} \tan \theta}{s}\right) \right] = \frac{\varepsilon_{o}\varepsilon_{r}W}{\tan \theta} \left[\ln\left(\frac{s + \frac{W}{2} \tan \theta}{s}\right) \right] = \frac{\varepsilon_{o}\varepsilon_{r}W}{\tan \theta} \left[\ln\left(\frac{s + \frac{W}{2} \tan \theta}{s}\right) \right] = \frac{\varepsilon_{o}\varepsilon_{r}W}{\tan \theta} \left[\ln\left(\frac{s + \frac{W}{2} \tan \theta}{s}\right) \right] = \frac{\varepsilon_{o}\varepsilon_{r}W}{\tan \theta} \left[\ln\left(\frac{s + \frac{W}{2} \tan \theta}{s}\right) \right] = \frac{\varepsilon_{o}\varepsilon_{r}W}{\tan \theta} \left[\ln\left(\frac{s + \frac{W}{2} \tan \theta}{s}\right) \right] = \frac{\varepsilon_{o}\varepsilon_{r}W}{\tan \theta} \left[\ln\left(\frac{s + \frac{W}{2} \tan \theta}{s}\right) \right] = \frac{\varepsilon_{o}\varepsilon_{r}W}{\tan \theta} \left[\ln\left(\frac{s + \frac{W}{2} \tan \theta}{s}\right) \right] = \frac{\varepsilon_{o}\varepsilon_{r}W}{\tan \theta} \left[\ln\left(\frac{s + \frac{W}{2} \tan \theta}{s}\right) \right] = \frac{\varepsilon_{o}\varepsilon_{r}W}{\tan \theta} \left[\ln\left(\frac{s + \frac{W}{2} \tan \theta}{s}\right) \right] = \frac{\varepsilon_{o}\varepsilon_{r}W}{\tan \theta} \left[\ln\left(\frac{s + \frac{W}{2} \tan \theta}{s}\right) \right] = \frac{\varepsilon_{o}\varepsilon_{r}W}{\tan \theta} \left[\ln\left(\frac{s + \frac{W}{2} \tan \theta}{s}\right) \right] = \frac{\varepsilon_{o}\varepsilon_{r}W}{\tan \theta} \left[\ln\left(\frac{s + \frac{W}{2}$$

where W is the total side length of the square electrode in m (537 μ m), s is the spacing between the lowest point of the hinged plate and the electrode in m, and θ is the angle the hinged plate makes with the horizontal in radians [21]. As the hinged plate becomes parallel to the electrode or as θ approaches zero, this model assumes the form of the parallel plate model as $\ln(1 + x) \approx x$. The total hinged plate capacitance is then found by doubling this, as equation 3.26 accounts for only one of the hinged plates.

Another option is to again model the diaphragm and electrode as a parallel plate capacitor, modifying the spacing variable. The parallel plate model treats the spacing between the plates as uniform and equal to the spacing between the center of the diaphragm and the electrode. A more accurate determination of the capacitance may be to use the average of the center and edge spacing of the diaphragm for the uniform plate spacing given by

$$C_{Pave} = \varepsilon_o \varepsilon_r \frac{W^2}{\frac{s+g}{2}}$$
 (3.27)

where g is the spacing when the diaphragm is at zero deflection in m (1.5 μ m).

The capacitance for the three models from zero to full-scale deflection is shown in Figure 3.26.

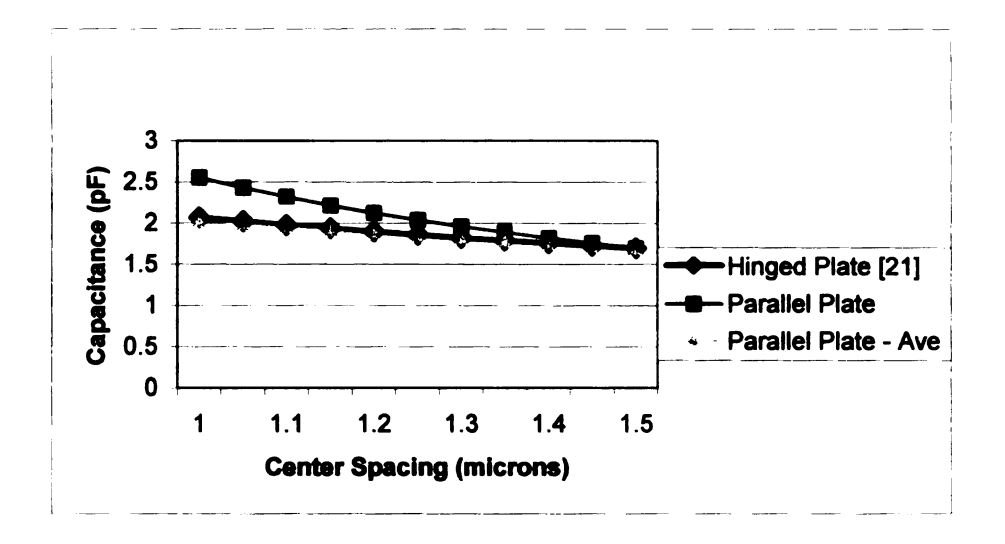


Figure 3.26 Comparison of Capacitance Models

While all three models are equal for zero diaphragm deflection, C_{Pave} and C_{HP} are approximately equal and significantly different than the parallel plate model as deflection increases. The parallel plate model provides the only direct relationship between the center deflection of the diaphragm and sensor capacitance. However, a more accurate relationship may be provided through calibration of the device.

The sensor capacitance is intended to change with diaphragm deflection only. Therefore the sensitivity of capacitance to temperature and pressure must be examined. As discussed with the parallel plate model, among other variables, the capacitance is dependent upon the dielectric constant of the insulating material between the plates. Variations in the dielectric constant may produce undesirable changes in the sensor capacitance.

The temperature coefficient of the dielectric constant of air, $\alpha_{\epsilon T}$, at 1 atm and 20°C is 2E-6/°C [6]. The capacitance as a function of temperature is given as

$$C_{\varepsilon T} = \frac{\varepsilon_o \varepsilon_r (1 + \alpha_{\varepsilon T} \Delta T) A}{d} \tag{3.28}$$

where A is the overlapping area of the plates (2.88E-7 m²), and d is the plate spacing in m. Holding all other variables constant, the capacitance is plotted as a function of cavity temperature along with the nominal capacitance in Figure 3.27.

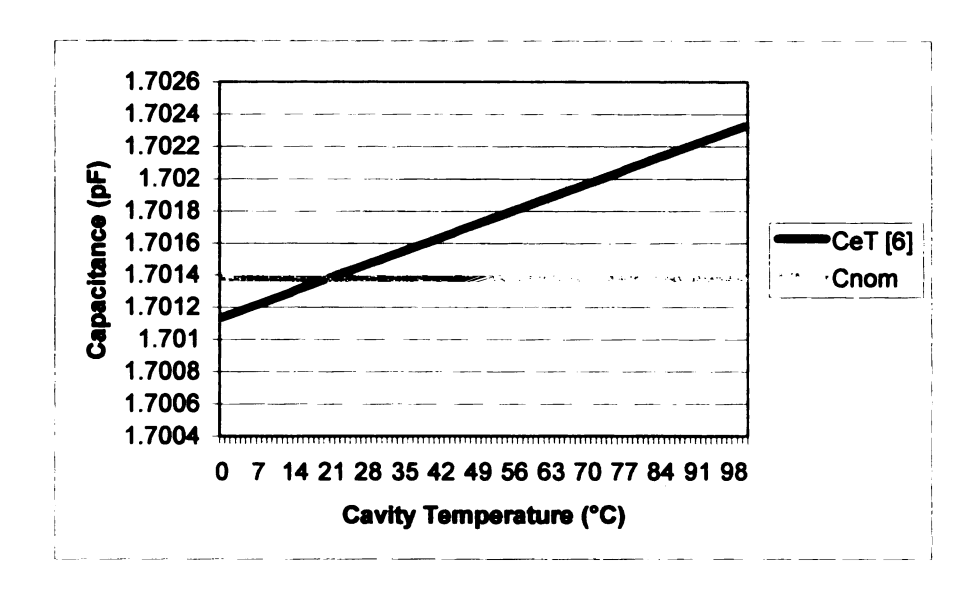


Figure 3.27 Capacitance vs. Cavity Temperature

Figure 3.27 shows the sensitivity of the capacitance to changes in the dielectric constant with temperature is 1.19E-5 pF/°C and is therefore negligible.

The pressure coefficient of the dielectric constant of air, $\alpha_{\epsilon P}$, at 1 atm is a more sizable 100E-6/°C [6]. The sensor cavity behaves according to the ideal gas law so that the cavity pressure will vary with volume and temperature of the cavity.

The volume of the cavity will change with thermal expansion/contraction of the sensor materials as well as the deflection of the diaphragm. The nominal volume of the

cavity, V_o, was calculated to be 8.69E-9 L at 20°C. When subjected to an increase in temperature of 80°C, the cavity volume was slightly decreased to 8.67E-9 L. This slight decrease is attributed to several factors. The minor expansions caused by the relatively low CTE for glass and silicon mostly cancel each other out producing a small increase in cavity volume. This small increase is dominated by the expansion of the relatively high CTE gold, filling up the cavity and reducing overall volume. To determine the volume change of the cavity due to deflections of the diaphragm, the volume created by the deflected diaphragm is modeled as a spherical segment according to Figure 3.28.

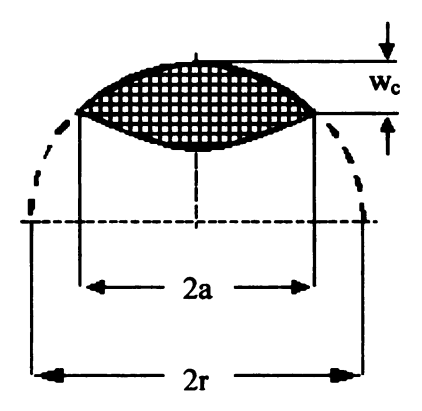


Figure 3.28 Model of a Spherical Segment [22]

The volume of the spherical segment in Figure 3.28 can be computed by

$$V_{seg} = \frac{\pi w_c}{6} \left(3a^2 + w_c^2 \right) \tag{3.29}$$

where V_{seg} is the volume in m³, w_c is the center deflection of the diaphragm in m, and a is half the side length of the diaphragm (2.755E-4 m) [22]. The volume of the spherical segment at a maximum diaphragm deflection of 0.5 μ m is 5.96E-11 m³. When subtracted from the nominal volume, the cavity volume is decreased to 8.63E-9 L. This

is a greater change in volume than that created by the expansion of the sensor materials and will therefore be used to determine how the changing volume of the cavity affects cavity pressure. The cavity pressure as a function of cavity volume, and hence diaphragm center deflection can be described by

$$P(V)_{cov} = [nR_u T]V_{cov}^{-1}$$
(3.30)

where P(V)_{cav} is given in L, n is 3.42E-13 kmol, R_u is 82.05 $\frac{L \cdot atm}{kmol \cdot K}$, and T is fixed at

the body temperature of 310 K. The cavity volume, V_{cav}, is given in L and is defined as

$$V_{cav} = V_o - V_{seg} \tag{3.31}$$

once V_{seg} has been converted to L. The capacitance as a function of volume dependent pressure, $C_{\epsilon(P-V)}$, is given in F by

$$C_{\varepsilon(P-V)} = \frac{\varepsilon_o \varepsilon_r (1 + \alpha_{\varepsilon P} \Delta P) A}{d}$$
(3.32)

where ΔP is the difference between $P(V)_{cav}$ and the reference pressure of 1 atm. $P(V)_{cav}$ is a function of diaphragm deflection and $C_{\epsilon(P-V)}$ can therefore be plotted with the nominal capacitance against the plate spacing in Figure 3.29.

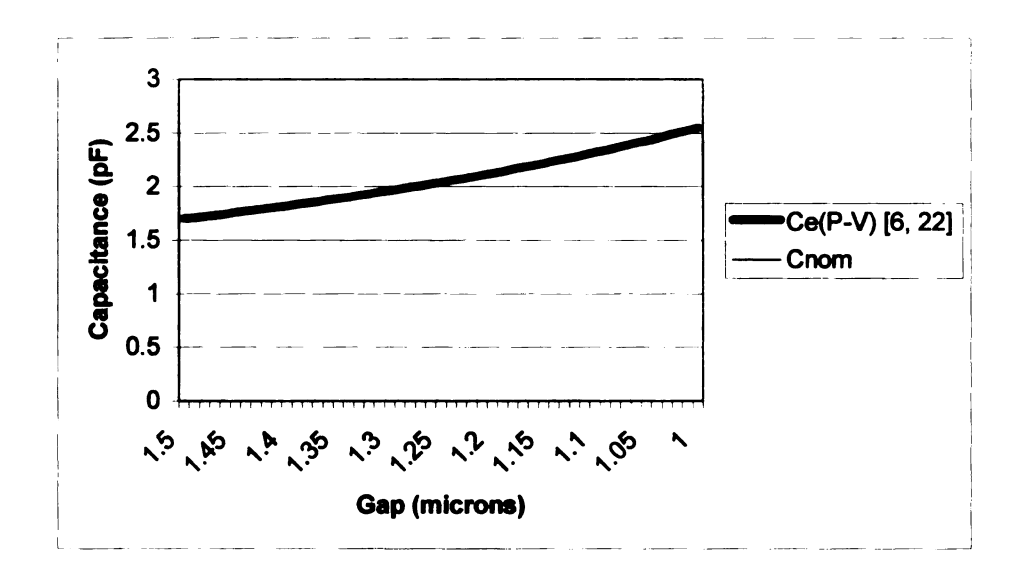


Figure 3.29 $C_{\epsilon(P-V)}$ vs. Plate Spacing

Figure 3.29 shows that the capacitance is not affected by changes in the dielectric constant with volume dependant pressure. Therefore, the cavity volume will be held constant in determining how the changing temperature of the cavity affects cavity pressure.

The cavity pressure as a function of temperature is given as

$$P(T)_{cav} = \left[\frac{nR_u}{V_o}\right] T_{cav} \tag{3.33}$$

where $P(T)_{cav}$ is given in L. The capacitance as a function of temperature dependent pressure, $C_{\epsilon(P-T)}$, is given in F by

$$C_{\varepsilon(P-T)} = \frac{\varepsilon_o \varepsilon_r (1 + \alpha_{\varepsilon P} \Delta P) A}{d}$$
(3.34)

where ΔP is the difference between $P(T)_{cav}$ and the reference pressure of 1 atm. $C_{\epsilon(P-T)}$ is plotted with the nominal capacitance against pressure for a corresponding temperature range of 0-100°C in Figure 3.30.

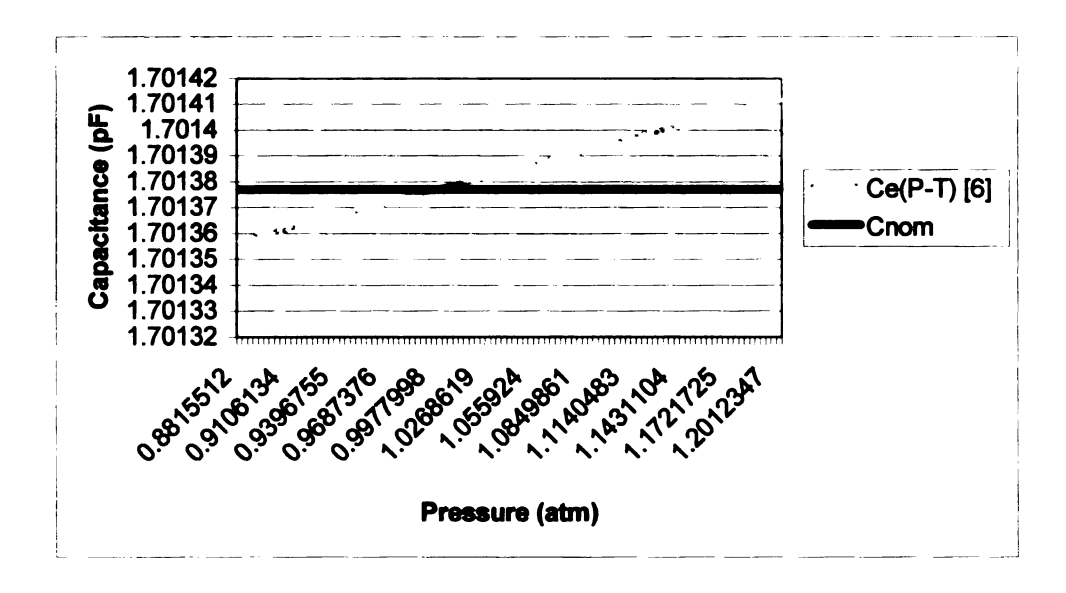


Figure 3.30 $C_{\epsilon(P-T)}$ vs. Pressure

Figure 3.30 shows the sensitivity of the capacitance to changes in the dielectric constant with temperature dependent pressure is 1.70E-4 pF/atm and is therefore negligible.

Capacitance changes as a result of dielectric constant variations with cavity temperature and pressure are negligible for the sensor operating conditions. Capacitance changes due to variations in overlapping plate area and spacing must therefore be examined. The overlapping plate area will be limited by the expansion of the smaller gold electrode. Assuming the planar expansion of the gold electrode is unconstrained at the top surface, the overlapping plate area, A_T , in m^2 is given as

$$A_T = A_o(1 + \alpha_{A\mu}\Delta T) \tag{3.35}$$

where A_0 is the nominal plate area (2.88E-7 m²). The thermal expansion of the silicon wafer and diaphragm, and the glass substrate will effectively cancel each other out due to the structure of the cavity and the similar CTEs of the materials, 2.6E-6/°C and 3.25E-6°C respectively [6]. The nominal spacing between the bottom face of the diaphragm and the base of the 2 μ m high gold electrode, g_0 , at zero deflection is 3.5 μ m. The unconstrained height of the gold electrode, h_{TAu} , is given in m by

$$h_{TAu} = h_{oAu} (1 + \alpha_{Au} \Delta T) \tag{3.36}$$

where h_{oAu} is 2E-6 m. The temperature dependent capacitance due to thermal expansions of the sensor, C_T , is given in F as

$$C_T = \frac{\varepsilon_o \varepsilon_r A_T}{g_o - h_{TAu}} \tag{3.37}$$

 C_T is plotted with the nominal capacitance against temperature in Figure 3.31.

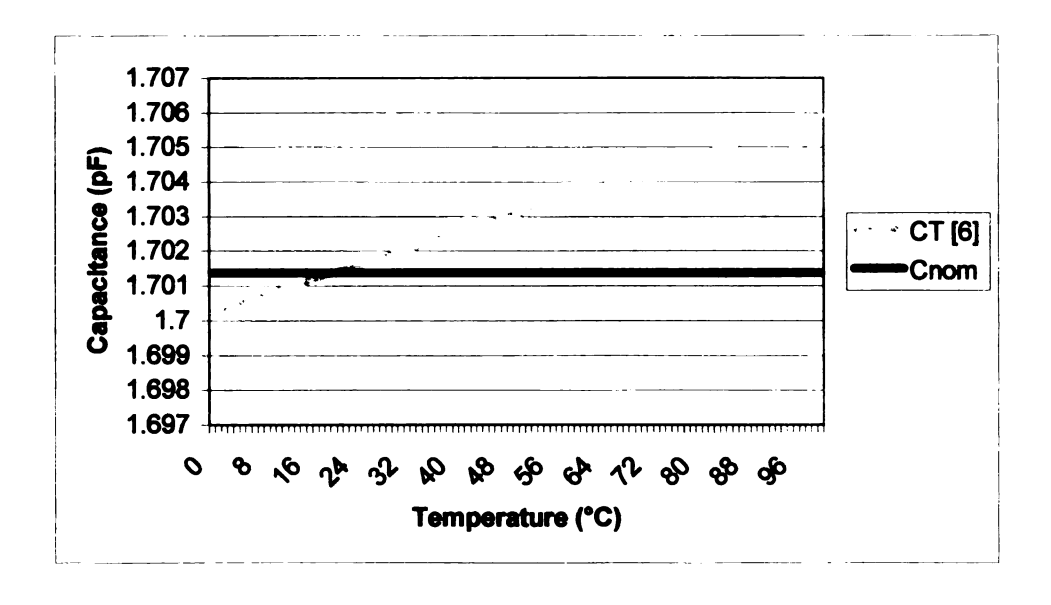


Figure 3.31 C_T vs. Temperature

Figure 3.31 shows the sensitivity of the capacitance to changes in temperature is 5.64E-5 pF/°C and is therefore negligible. The sensor capacitor will therefore perform as designed. The capacitance will be a function of diaphragm deflection only with insignificant changes as the temperature and pressure of the sensor cavity vary.

An important consideration when dealing with capacitors is the phenomenon of dielectric breakdown or electrostatic discharge (ESD). This occurs when a charge buildup or potential difference across the capacitor plates exceeds the dielectric strength of the insulating material. The resulting breakdown permanently damages the capacitor. The well-known Paschen curve describes the breakdown voltage of air at atmospheric pressure as a function of the gap spacing [23]. Breakdown is attributed to the Townsend avalanche. The excessive charge buildup pulls the negatively charged electrons in one direction and the positively charged ions in the other. As the electrons are accelerated towards the anode and the cations towards the cathode, they collide with other neutral atoms in the air creating more electron/cation pairs. These then undergo the same separating process creating an avalanche. This avalanche ionizes the air molecules changing the air from an insulator to a conductor. The ionized air provides a path for the current between the capacitor plates. For gaps greater than 10 µm, breakdown has been well studied and occurs when the potential difference exceeds 3 V/µm [23]. Circuit simulations indicate the sensor capacitor will experience voltage drops in the range of 7.2-3.5 V. ESD would certainly occur for the capacitor spacing of 1.5-1.0 µm. However, the electrical current can result from other mechanisms besides the Townsend avalanche in an ionized gas, and these other mechanisms are not considered in the theory behind the Paschen curve. For electric fields across gaps from 5nm to 5µm, field emission is the

mechanism responsible for ESD [23]. The Modified Paschen curve suggests a more lenient field breakdown strength of 75V/µm [23]. Other sub micron gap testing in literature reports the field breakdown strength on the order of 150V/µm [23, 24]. The greater field breakdown strengths assure that ESD will not occur in the sensor's capacitor.

3.3 Cavity Pressure Considerations

The differential pressure across the sensor diaphragm is determined from the diaphragm's deflection. Once the pressure differential is known, exact IOP measurements can be recorded only if the cavity pressure values are accurate. The nominal cavity pressure when the sensor is at the body temperature of 37°C is 1 atm. However, this will change as the cavity temperature varies. Cavity temperature variations will occur as the temperature of the sensor environment changes. While the sensor is in operation, resistive heating may also elevate the cavity temperature. To investigate the effects environmental temperature and the resistive heating of the coil will have on cavity temperature, a FEM analysis was performed using the Ansys University High program. To reduce the size of the program, half of the sensor cross-section was modeled surrounded by a layer of aqueous humor. Figures 3.32 and 3.33 show the whole model and a close-up of a portion of the sensor cavity respectively.



Figure 3.32 FEM Model

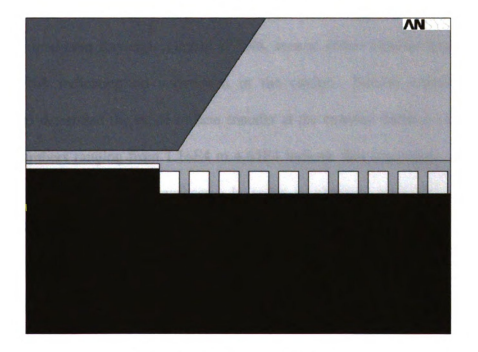


Figure 3.33 Close-up of Cavity

The mode of heat transfer in the cavity was determined by examining the cavity's Rayleigh number. For horizontal cavities heated from below with a width and depth much greater than the height and Rayleigh numbers less than the critical value of 1708,

buoyancy forces cannot overcome the resistance imposed by viscous forces and there is no convection in the cavity [25]. The Rayleigh number is defined as

$$Ra_{L} = \frac{g\beta(T_{1} - T_{2})L^{3}}{\alpha v}$$
 (3.38)

where g is gravity in m/s², T_1 and T_2 are the temperatures at the bottom and top of the cavity respectively in K, L is the cavity width in m, α is the thermal diffusivity of the cavity fluid in m²/s and ν is the kinematic viscosity of the cavity fluid in m²/s. The expansion coefficient, β , for an ideal gas is 1/ T_2 [25]. Rayleigh numbers were calculated using a cavity width of 1160 μ m. Temperatures at the top of the cavity were varied from -23 to 127°C while increasing the temperature differential up to 20°C. Calculations produced a maximum Rayleigh number of 2.46, several orders smaller than the critical value of 1708 indicating no convection in the cavity. Similar calculations were performed to determine the mode of heat transfer at the external surfaces of the sensor. Rayleigh numbers ranging from 1.16E4 to 4.65E4 indicate that convection would occur at the top and bottom sensor surfaces. In order to obtain a worst-case scenario of elevated cavity temperatures, conduction was the only mode of heat transfer used in the analysis.

A constant temperature of 37°C was applied to the outer boundary of the aqueous humor to model body core temperature. The heat generated by the resistive components of the sensor varies with frequency as the circuit performs a frequency sweep. It is estimated that it will take approximately 1 second to complete a sweep and that they will be performed continuously. In adherence to a worst-case scenario for cavity temperature

elevations, the maximum value of 10.6 mW was used to apply a constant volumetric heat generation of 1.5E-9 $W/\mu m^3$ to the model areas representing the gold portions of the sensor.

The thermal conductivity of the glass, gold, silicon and aqueous humor portions of the model were treated as properties independent of temperature. The values used in the analysis are listed in Table 3.5.

Table 3.5 Constant Thermal Conductivities

Material	Thermal Conductivity (W/mK)
Glass	1.4
Gold	317
Silicon	148
Aqueous Humor	0.58

The thermal conductivity for air was entered as temperature dependent. The values used are shown in Table 3.6.

Table 3.6 Thermal Conductivity of Air

Temperature (K)	Thermal Conductivity (W/mK)
250	22.3E-3
300	26.3E-3
350	30E-3
400	33.8E-3

The elements used to mesh the model are the PLANE55 four node rectangular elements. Each node has one degree of freedom representing temperature. The model was meshed using free triangular shapes. The triangular shapes are formed by collapsing two nodes together. The Smart Size option was implemented using a fine mesh size of 1. The entire meshed model and a portion of the meshed cavity are shown in Figures 3.34 and 3.35 respectively.

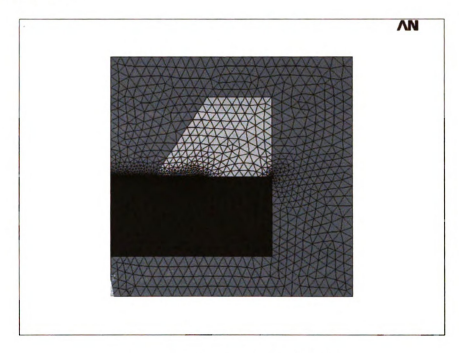


Figure 3.34 Entire Meshed Model

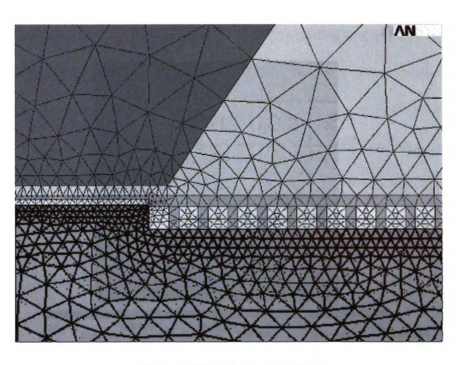


Figure 3.35 Meshed Cavity

It is assumed the sensor will reach steady-state rapidly compared to changes in body temperature due to its miniature size. Therefore, a steady-state analysis was performed. Results of the analysis are presented as contour plots of the temperature distribution throughout the sensor. Figures 3.36 and 3.37 show the contour plots of the whole model and the cavity portion respectively. Temperatures are listed in K.

ΛN

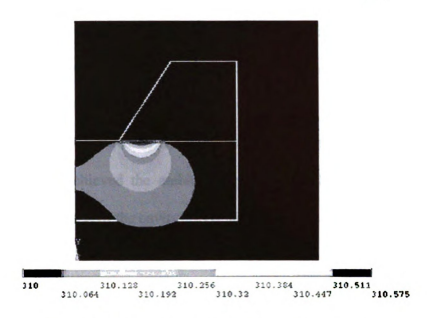


Figure 3.36 Temperature Distribution in the Sensor

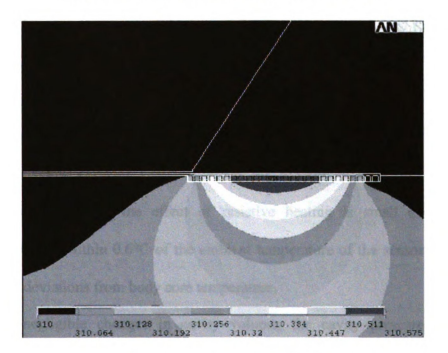


Figure 3.37 Cavity Temperature Distribution

The cavity temperature under the diaphragm is maintained at the body-core temperature of 37°C (310 K). Even with the worst-case scenario heat generation applied to the model, the cavity temperature in the coil region is elevated a mere 0.575°C above the

ambient temperature. After obtaining the results, the meshing was refined at the material interfaces in the model. Refined meshing produced identical temperature distributions indicating the initial mesh was accurate. Additional analyses were then performed by applying different temperatures at the outer boundary of the aqueous humor. The ambient temperature was increased and decreased 10°C. In both cases the diaphragm region of the cavity achieved the ambient temperature. The maximum temperature elevation in the coil region of the cavity was 0.58°C. Results of the analyses are listed in Table 3.7.

Table 3.7 FEM Analysis Results

Cavity Temperature (°C)		
Diaphragm Region	Coil Region	
27	27.58	
37	37.575	
47	47.57	
	Diaphragm Region 27 37	

The results conclude that the effect of resistive heating is small and the cavity temperature will be within 0.6°C of the ambient temperature of the sensor environment for 10-degree deviations from body core temperature.

With negligible changes in cavity volume, the cavity pressure varies with temperature according to the Ideal Gas Law. The temperature dependent cavity pressure is plotted in Figure 3.38.

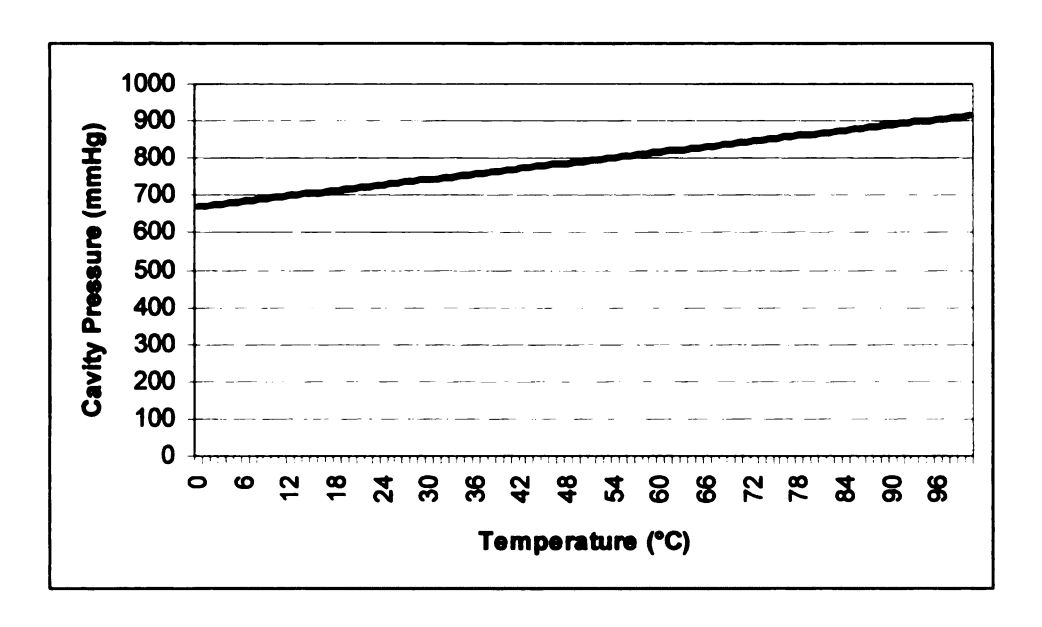


Figure 3.38 Cavity Pressure vs. Temperature

The cavity pressure varies with temperature with a sensitivity of 2.45 (mmHg/°C). The 0.6°C deviations caused by resistive heating would produce a mere 1.47 mmHg change in cavity pressure. An ambient temperature swing of approximately 10°C from body core would offset the nominal cavity pressure by 24.5 mmHg. This deviation is equivalent to 40.83% of the pressure range of interest (760 – 820 mmHg). Therefore, once implanted in the eye, the cavity pressure of the sensor cannot be treated as a constant 1 atm (760 mmHg). Cavity temperatures can potentially be determined from observations in the peak height and width from the voltage profile acquired from R_{ext} as discussed in section 3.2.1. With known cavity temperatures, the exact cavity pressure can be used to obtain IOP measurements accurately.

Chapter 4. Eye Considerations

4.1 Eye Models Available in Literature

The previous chapter has shown that the IOP sensor is temperature sensitive. It is therefore necessary to understand what temperatures the sensor will be subjected to once implanted in the eye. A common belief is that the temperature in the vitreous cavity is regulated with body temperature to within a few tenths of a degree centigrade [26]. The sensor will not be located in the vitreous cavity. Rather, it will be implanted in the anterior chamber between the iris and cornea. A review of pertinent literature was undertaken to investigate what sort of temperature fluctuations the sensor environment might experience.

An article by Scott discusses a finite element model of heat transport in the human eye [27]. The control ambient temperature is 20°C and the control body-core temperature imposed on the sclera is 37°C. The cooling mechanisms of the model are assumed to be at the surface of the eyeball. Heat is lost to the surrounding air from the anterior corneal surface by evaporation, convection and radiation. The steady-state temperatures along the pupillary axis of a wide-open eye were calculated using the control parameters. Scott's results for several points along the pupillary axis are listed in Table 4.1.

Table 4.1 Steady-state Temperatures (Control Values) [27]

Location	Temperature (°C)
Posterior Corneal Surface	33.25
Anterior Pole of the Lens	35.20
Posterior Pole of the Lens	36.01
Retina	36.89

These values indicate an uneven temperature distribution throughout the eye. The location of the sensor would lie somewhere between the posterior corneal surface and the anterior pole of the lens. The location of the sensor alone suggests a temperature difference of several degrees from body-core temperature under the controlled circumstances. Next Scott considers the effect of changing the ambient temperature. Scott's results of this analysis are listed in Table 4.2.

Table 4.2 Steady-state Temperatures (Increased Ambient) [27]

Ambient	Location			
Temperature	Posterior	Anterior Pole	Posterior Pole	
(°C)	Corneal Surface	of the Lens	of the Lens	Retina
20	33.25	35.20	36.01	36.89
25	34.79	35.65	36.26	36.92
30	35.15	36.11	36.51	36.94

The effect of the increased ambient temperature is most severe at the corneal region and decreases towards the retina. In the region of implantation, the values suggest an increase of 1.9 – 0.91°C from the control values for a 10°C increase in ambient temperature. Scott then proceeds to examine the effects of increasing the body-core temperature, which may occur during physical activity, while holding the ambient temperature at the control value. These results are listed in Table 4.3.

Table 4.3 Steady-state Temperatures (Increased Body-core) [27]

Body-core	Location				
Temperature	Posterior	Anterior Pole	Posterior Pole		
(°C)	Corneal Surface	of the Lens	of the Lens	Retina	
37	33.25	35.20	36.01	36.89	
37.7	33.81	35.83	36.67	37.58	
38	34.05	36.10	36.96	37.88	
38.5	34.45	36.55	37.43	38.38	

The effect of the increased body-core temperature is most severe in the retina region and decreases towards the cornea. The values suggest an increase of 1.2 – 1.35°C from the control values in the region of implantation for a 1.5°C increase in body-core temperature. However, Scott does not include an analysis for increasing both ambient and body-core temperatures nor any experimental data.

In another article Scott author considers temperature rises in the human eye induced by infrared radiation [28]. The article focuses on glass and iron mill workers who may be exposed to temperatures in the range of 1250 - 1500°C and experience

irradiation incident upon the eye up to 5000 W/m². The effect of blinking every 2.8s and holding the eyelid closed for 0.3s is incorporated in the cooling mechanisms of this finite element model. Scott considers the case of a wide-open eye in an ambient temperature of 20°C, with a body-core temperature of 37°C exposed to the incident irradiation of 2100 W/m². The steady-state temperature at the corneal surface reaches an elevated 44°C. Scott then examines the effects of increased blinking, increased tear evaporation and eyelid shielding. The author's results are listed in Table 4.4.

Table 4.4 Corneal Surface Temperatures for 2100 W/m² Incident Irradiation [28]

C	Control	Increased	Increased	Eyelid ½	Eyelid 3/4
Case	Control	Blinking	Evaporation	Closed	Closed
Temperature	44	43	40.6	41.5	39
(°C)	17	73	70.0	71.5	39

These values show the corneal surface temperature is significantly reduced. However, even with the most effective cooling mechanism of eyelid shielding, the temperature is several degrees higher than body core temperature. Scott proceeds to examine the case of a wide-open eye subject to an incident irradiation of 1250 W/m² for a period of 30s combined with the effect of changing the ambient temperature. The standard cooling mechanisms are utilized with the control body-core temperature of 37°C. The Scott's results are listed in Table 4.5.

Table 4.5 The Effect of Ambient Temperature on Temperature Rises Experienced in the Eye Exposed to an Incident Irradiance of 1250 W/m² [28]

Exposure Time (s)	Tamb (°C)	Anterior Pole of the Lens (°C)	Posterior Pole of the Lens (°C)	Posterior Surface of Iris in Contact with Lens (°C)
0	20	34.57	36.01	35.20
30	20	35.41	36.10	35.81
0	30	35.80	36.51	36.11
30	30	36.64	36.60	36.73
0	20	34.57	36.01	35.20
30	30	35.61	36.11	35.98

These values indicate that the largest temperature elevation will occur in the implantation region for irradiation exposure combined with elevated ambient temperatures. Scott's calculations suggest that different levels of exposure to infrared radiation for varying amounts of time coupled with increased ambient temperatures may significantly elevate the temperature of the sensor's environment.

An article by Lagendijk [29] contains a finite difference model of the human eye along with experimental data on New Zealand rabbits. The steady-state temperature distribution in the human eye subject to a body-core temperature of 37°C and an ambient temperature of 20°C matches that of Scott [27]. For the experimental data, a constant temperature water bath at 43 - 45°C transferred heat to the rabbit eyes through a thin rubber film. A thin thermocouple was inserted in the eye of four rabbits to record temperatures at various locations. Control values for comparison were recorded for an

ambient temperature of 23°C and a rectal temperature of 38.8°C. The Lagendijk's results are listed in Table 4.6.

Table 4.6 Experimental Rabbit Data [29]

Location	Control Temperature (°C)	Average Temperature (°C)
Cornea	34.5	43.8
Behind Lens	37.4	40.4
Retina	38.1	39.4

Results show a large increase of 9.3°C from the control temperature at the cornea and a significant increase of 3°C behind the lens. This experiment proves that the temperature of the sensor environment can be considerable increased under certain conditions.

The review of the above articles suggests that the temperature distribution throughout the eye varies by several degrees. Although increased cooling mechanisms may reduce the effect, elevated body-core temperature combined with ambient and environmental conditions have the potential to severely elevate the temperature of the sensor's environment. The experimental data proves that this temperature can be significantly elevated under the right conditions.

4.2 Heat Transfer Model of the Human Eye

Upon reviewing available eye models, a two-dimensional heat transfer model of the human eye was created to further investigate what temperature fluctuations the eye might experience. The perimeter of the eye was modeled as a circle with a bulging at the equator of the cornea with a diameter of 20.8 mm according to Gustrau *et al* [30]. The interior of the eye is modeled according to Amara *et al* and consists of seven tissues [31]. These tissues are: 1) vitreous humor; 2) aqueous humor; 3) lens; 4) iris; 5) cilliary body;

6) cornea; and 7) retina. Figure 4.1 shows the FEM model of the eye created with the Ansys University High program.

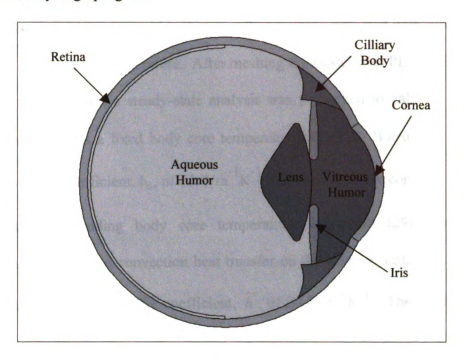


Figure 4.1 FEM Human Eye Model

The thermal conductivities of the tissues are taken from Amara *et al* [31] and are listed in Table 4.7.

Table 4.7 Tissue Thermal Conductivities [31]

Tissue	k (W/mK)	
Vitreous Humor	0.603	
Aqueous Humor	0.58	
Lens	0.4	
Iris	0.58	
Cilliary Body	0.58	
Cornea	0.58	
Retina	0.628	

The modes of heat transfer considered in the model are tear film evaporation, radiation and convection at the anterior corneal surface with the surroundings, and convection between the sclera and body core. The retina, permeated with blood vessels, will be held at body core temperature. After meshing the model with PLANE55 elements as free triangular shapes, a steady-state analysis was performed to validate the model. The retina was held at a fixed body core temperature of 37°C. Borrowing from Scott [28], a convective coefficient, h_s , of 65 Wm⁻¹K⁻¹ was used to apply convection from the sclera to the surrounding body core temperature. Lagendijk [29] combined the evaporation, radiation and convection heat transfer on the anterior surface of the cornea to give a combined heat transfer coefficient, \tilde{h} , of 20 Wm⁻¹K⁻¹. This coefficient was used for the convection between the cornea and quiescent air at 20°C. Conduction is the mode of heat transfer within the eye. Results of the simulation are shown as a contour plot in Figure 4.2.

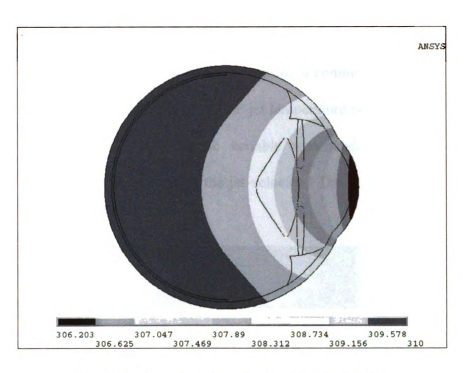


Figure 4.2 Temperature Distributions in the Eye

Temperatures in Figure 4.2 are listed in Kelvin. Results of the simulation match those of Scott [27] listed in Table 4.1, thus confirming this as an acceptable heat transfer model of the human eye.

4.3 Cat Testing

To prove temperature fluctuations can occur within eye, experimental data was needed. Cats were used as the test subject as they were readily available and have eye dimensions comparable to that of a human. A test rig was constructed to allow jets of air at various wind speeds, temperatures, and with varying relative humidities to be blown on the eye of an anesthetized cat. The rig was constructed of cylindrical aluminum duct and a plastic funnel 40.64 cm overall in length. A fan was attached at the end of the rig and the heating element from a hot plate was formed into a coil and housed within the 10.16 cm diameter duct. The base of the rig rested on top of a hot plate supporting a beaker filled with water. The 2.54 cm diameter iet outlet in the funnel was placed 2.54 cm away

from the cat's eye lined up dead center. The relative humidity of the jet was controlled by boiling water on the hot plate in addition to using a common misting bottle. Along with the steam generated by the hot plate, the jet temperature was controlled by the coil heating element connected to a Variac variable autotransformer. A whisper fan connected to another Variac controlled the jet velocity. The test rig is shown in Figure 4.3.

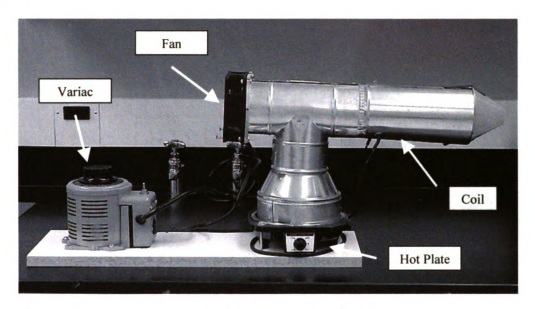


Figure 4.3 Test Rig for Cat Testing

Jet velocities and temperatures were recorded using a Dwyer Instruments VT-200 flow anemometer. Jet relative humidities were recorded using an Omega RH71 digital hygro-thermometer. Eye temperatures were recorded using an Omega HYP1-30-1/2-T-G-60-SMPW-M type T hypodermic needle thermocouple probe. The 30 gage x 15 mm needle was inserted in the eye between the cornea and iris near the cilliary body at the proposed location for the sensor. The needle was inserted to a depth of approximately 3 mm. The probe leads were connected to an Omega HH23 microprocessor thermometer,

converting voltage levels to temperature readings. Figure 4.4 shows the needle probe for size comparison.



Figure 4.4 Hypodermic Needle Thermocouple Probe

Testing simulated conditions a person's eye might experience in a hot or cold environment, under dry or humid conditions, on a calm or windy day. The purpose was to determine what temperature differences, if any, exist in the eye of a person in an Arizona summer versus that of a person experiencing a Michigan winter. The majority of the testing was conducted at room temperature in a lab while lower temperature testing was performed in a cold room. In each trial, ambient temperature, jet properties, and initial eye temperature were measured. All trials were performed at an ambient pressure of 1 atm. Upon application of the jet, final eye temperatures were allowed to reach steady state before being recorded. Rectal temperatures for the cat were also chronicled intermittently. Initial conditions of the testing are listed in Table 4.8.

Table 4.8 Cat Testing Initial Conditions

Trial	Tambient °C	Teye Initial °C	Trectal °C
1	23.61	34.61	39.17
2	23.61	34.61	
3	23.61	34.61	
4	23.61	34.61	
5	27.78	36.00	39.17
6	27.78	36.28	
7	27.78	36.83	
8	27.78	36.28	39.22
9	27.78	36.83	
10	27.78	34.50	
11	27.78	36.11	38.94
12	8.50	34.00	38.44
13	8.50	34.00	
14	8.50	34.00	

Results of the testing are listed in Table 4.9.

Table 4.9 Cat Testing Results

Trial	Tfinal °C	Tdelta °C	Vjet (m/s)	Tjet °C	Jet %RH
1	34.22	-0.39	1.79	23.67	13.80
2	33.06	-1.56	3.58	23.78	13.80
3	33.17	-1.44	8.94	23.67	13.80
4	32.50	-2.11	12.52	23.67	13.80
5	35.22	-0.78	1.79	29.44	12.70
6	37.00	0.72	1.79	35.00	12.80
7	37.50	0.67	1.79	42.50	12.80
8	36.28	0.70	1.79	48.89	13.00
9	37.72	0.89	1.79	68.33	18.30
10	35.17	0.67	12.52	50.56	20.50
11	36.50	0.39	2.32	31.11	78.00
12	32.83	-1.17	3.58	8.50	42.00
13	30.78	-3.22	12.52	8.50	42.00
14	30.78	-3.22	12.52	8.50	69.00

Tables 4.8 and 4.9 show that the maximum temperature change caused by the application of the jet is -3.22°C. Furthermore, the initial ocular temperatures change slightly as the ambient temperature varies. The relative humidity of the jet does not appear to have a significant effect on ocular temperature changes as seen by comparison of trials 5 to 11, and 13 to 14 in Figure 4.5.

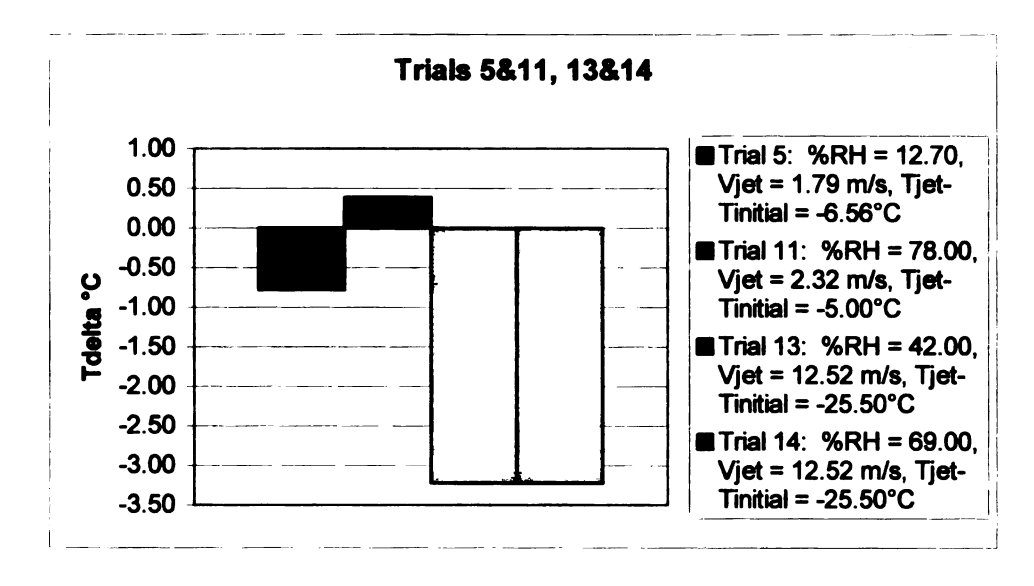


Figure 4.5 Effect of Jet Relative Humidity on Ocular Temperature Changes

While the pairs of trials in both groups have comparable jet velocities and relative jet temperatures, the jet relative humidities in each pair are drastically different. Even so, the differences for temperature changes within the eye are minimal. Therefore, the conclusion is reached that jet relative humidity does not have a significant effect on ocular temperature changes. The absolute humidities of the jet were also investigated and showed no significant effect as well.

The first four trials were performed with equal jet relative humidities and nearly identical relative jet temperatures. The jet velocities were varied considerably. Ocular temperature changes are plotted against jet velocities in Figure 4.6.

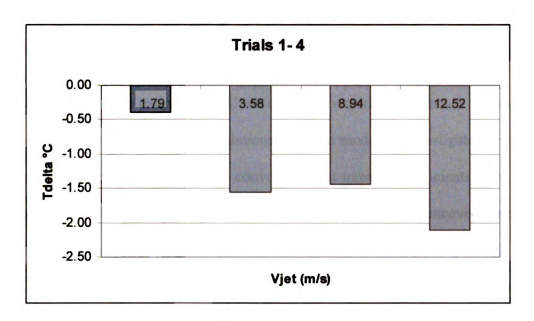


Figure 4.6 Effect of Jet Velocity on Ocular Temperature Changes

The data in Figure 4.6 shows that ocular temperature changes are sensitive to the jet velocity, independent of the other variables.

It is also evident from Table 4.9 that the eye is more sensitive to lower temperatures. Temperature changes for colder jets are greater at the same or lower jet velocities than their warmer counterparts.

Results of the cat testing indicate that ambient temperatures do in fact affect ocular temperatures. Temperature changes within the eye are increased by the application of a jet simulating a breeze. These changes are sensitive to jet velocity and temperature while the effect of humidity is insignificant. Furthermore, colder jets have a greater impact on temperature changes than warm ones. The greatest temperature fluctuations experienced during the testing suggest a deviation of ±5°C from body core would encompass all possible temperatures that may occur in the human eye.

4.4 Simulation Comparison to Cat Testing

The validity of the human eye model was previously established for heat transfer to quiescent air at room temperature. Upon obtaining experimental data, it was desirable to compare cat testing results to simulations with the model to investigate the model's potential for future applications. New convective heat transfer coefficients were needed to simulate the conditions of the testing trials. A literature review uncovered an article pertaining to round jet impingement heat transfer on a convex, hemispherical surface [32]. Lee *et al* developed a stagnation point Nusselt number correlation for jet Reynolds number range from 11,000 to 50,000 and dimensionless nozzle-to-surface distance from 2 to 10

$$Nu_{st} = 1.68(\text{Re})^{0.48} (L/d)^{0.1} (d/D)^{0.18}$$
(4.1)

where Nu_{st} is the Nusselt number at the stagnation point, Re is the Reynolds number, L is the nozzle-to-surface distance in m, d is the nozzle diameter in m, and D is the surface diameter in m [32]. The Reynolds number is defined as

$$Re = \frac{\rho V d}{\mu} \tag{4.2}$$

where ρ is the fluid density in kg/m³, V is the fluid velocity in m/s, d is the nozzle diameter in m, and μ is the dynamic fluid viscosity in Pa*s. The convective heat transfer coefficient is determined from the Nusselt number correlation

$$Nu_{st} = \frac{h_{st}D}{k} \tag{4.3}$$

where h_{st} is the stagnation point convective coefficient, D is the diameter of the eye in m,

and k is the thermal conductivity of the fluid in W/mK. The values used in Eqs 4.1-3 are listed in Table 4.10.

Table 4.10 Constants for Nu_{st} Correlation [32]

Constant	L	d	D
Value (m)	0.0254	0.0254	0.0208

For all test trials, the jet fluid had a relevant relative humidity. Therefore, the fluid properties used must be that of humid air rather than its dry air/steam constituents. Richards et al propose two correlations for determining the dynamic viscosity and thermal conductivity of moist air from the component properties [33]. The dynamic viscosity can be determined using

$$\mu_{m} = \frac{\mu_{1}}{1 + \Psi_{12}(X_{2}/X_{1})} + \frac{\mu_{2}}{1 + \Psi_{21}(X_{1}/X_{2})} \tag{4.4}$$

where μ_m is the mixture viscosity in Pa*s, μ_1 is the air viscosity in Pa*s, μ_2 is the steam viscosity in Pa*s, Ψ_{12} and Ψ_{21} are coefficients with values 0.8390 and 0.7438 respectively, and X_1 and X_2 are the mole fractions of air and steam respectively [33]. The thermal conductivity can be determined using

$$k_m = \frac{k_1}{1 + \Phi_{12}(X_2 / X_1)} + \frac{k_2}{1 + \Phi_{21}(X_1 / X_2)}$$
(4.5)

where k_m is the mixture thermal conductivity in W/mK, k_1 is the air thermal conductivity in W/mK, k_2 is the steam thermal conductivity in W/mK, Φ_{12} and Φ_{21} are coefficients with values 0.8153 and 0.7257 respectively [33].

For mixtures of ideal gasses such as air and steam, each component can be treated as an ideal gas alone at the mixture volume and temperature. Partial pressures can be evaluated using the ideal gas equation of state

$$\sum p_i = \frac{(\sum n_i)\overline{R}T}{V} \tag{4.6}$$

The mole fractions of air and steam, X₁ and X₂, can therefore be determined from

$$X_1 = \frac{P_a}{P_m}, X_2 = \frac{P_v}{P_m} \tag{4.7}$$

where P_a is the partial pressure of the dry air, P_m is the total pressure of the mixture, and P_v is the partial pressure of the steam. The relative humidity, ϕ , of the jet can be used to determine P_v by

$$\phi = \frac{P_{\nu}}{P_{g}} \tag{4.8}$$

where P_g is the saturation pressure of water at the jet temperature, readily available from steam tables. The partial pressure of the air is the difference between the atmospheric pressure of the jet mixture and the partial pressure of the steam

$$P_a = P_m - P_v = P_{atm} - P_v \tag{4.9}$$

For all trials, the partial pressure of the vapor was less than the saturation pressure of water at the jet temperature. Appropriate fluid properties for the dry air and superheated vapor at partial pressures and jet temperature were then obtained from several sources [25, 34, 35, 36]. Jet dynamic viscosity and thermal conductivity were determined using Eqs. 4.4 and 4.5 while jet density was calculated on a mole fraction basis. The jet properties are listed in Table 4.11.

Table 4.11 Jet Properties [33]

Trial	ρ (kg/m ³)	k (W/mK)	μ (Pa*s)
1	1.180	1.8469E-02	1.8292E-05
2	1.180	1.8476E-02	1.8298E-05
3	1.180	1.8469E-02	1.8292E-05
4	1.180	1.8469E-02	1.8292E-05
5	1.155	1.8857E-02	1.8571E-05
6	1.130	1.9262E-02	1.8829E-05
7	1.095	1.9852E-02	1.9175E-05
8	1.064	2.0402E-02	1.9467E-05
9	0.930	2.2787E-02	2.0289E-05
10	1.036	2.0784E-02	1.9520E-05
11	1.082	1.9654E-02	1.8577E-05
12	1.243	1.7596E-02	1.7533E-05
13	1.243	1.7596E-02	1.7533E-05
14	1.235	1.7661E-02	1.7526E-05

The jet properties were then used in Eqs. 4.1-2 to calculate the Reynolds and Nusselt numbers plotted in Figure 4.7.

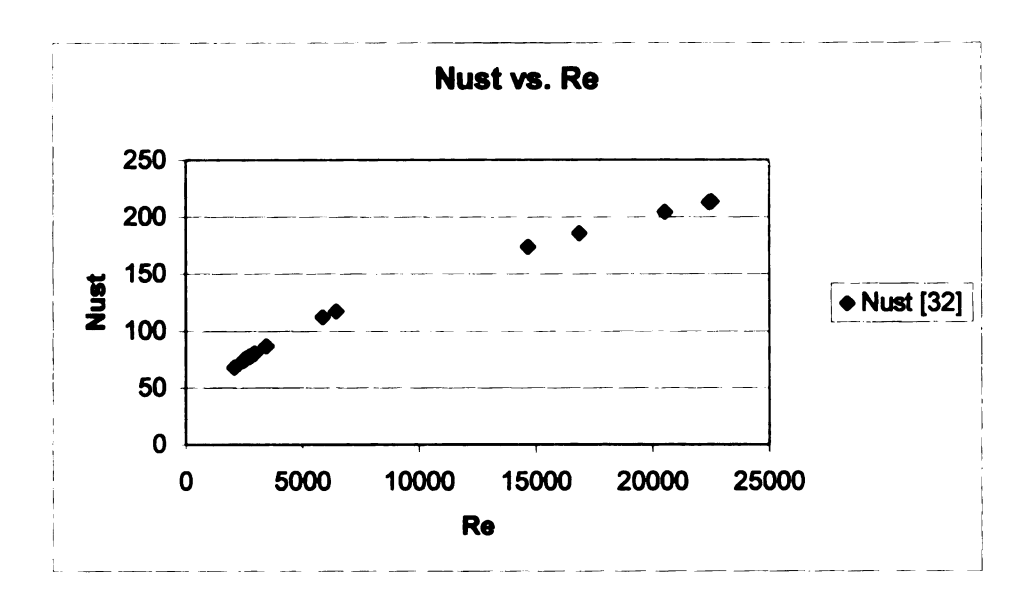


Figure 4.7 Nusselt, Reynolds Numbers From Cat Testing

It is important to note that the majority of the Reynolds numbers lie below the range used by Lee *et al* [32] and may therefore provide less accurate Nusselt number correlations for the convective heat transfer coefficient.

The coefficients obtained through Equation 4.3 were then applied to the eye model. Convection was assumed to be the dominant form of heat transfer at the corneal surface. The rest of the model remained the same, except that the cat rectal temperatures were used in place of the human body core. Temperatures from the simulations were recorded in the region of the proposed sensor location as shown in Figure 4.8.

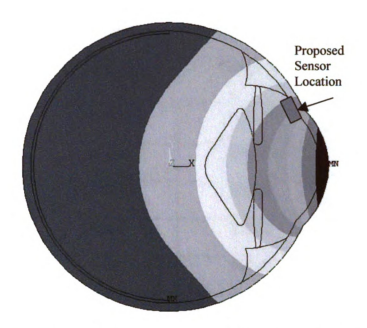


Figure 4.8 Region for Temperature Recording from Simulations

This region matches the approximate location of the needle probe used in the cat testing.

Results of the simulations are compared to the testing trials in Table 4.12.

Table 4.12 Simulation Comparison to Cat Testing

Trial	h _{st} (W/m ² K)	Tfinal (K)	Tsimulation (K)
1	71.36	307.37	306.97-308.75
2	99.54	306.21	306.11-308.18
3	154.51	306.32	304.97-307.42
4	181.60	305.65	304.61-307.18
5	71.58	308.37	308.96-310.08
6	71.87	310.15	310.88-311.36
7	72.33	310.65	313.09-313.29
8	72.78	309.43	314.06-315.18
9	74.70	310.87	319.23-320.94
10	186.05	308.32	316.16-317.11
11	81.99	309.65	309.20-310.16
12	99.19	305.98	299.54-303.55
13	180.97	303.93	296.70-301.67
14	181.15	303.93	296.70-301.66

The data in Table 4.12 indicate that the simulations with the eye model produce results comparable to those of the actual trials. The greatest discrepancies occurred in trials 7-10. The simulation did not provide adequate cooling in majority of the cases where the jet is heating the eye. The maximum difference between Tfinal and Tsimulation observed was 8.36 K. Disparities this large discount the accuracy of the model. The results are, however, comparable. For trials 12-14, where cold jets were used, the

simulation temperatures dropped a maximum of 2.6 K lower than the experimental values. Again, while not entirely accurate, the results are comparable promising this model can be improved upon for use in future applications.

Chapter 5. Future Work

5.1 Sensor

This thesis work has focused on temperature considerations surrounding the sensor's environment and operation and how they will affect its pressure readings. However, there is still work to be done in the development of the IOP monitoring system. To date, the Fraunhofer Institute has not yet delivered a functional prototype of the sensor. Current deliveries of the sensor are shown in Figures 5.1-2.



Figure 5.1 Top View of Sensor



Figure 5.2 Bottom View of Sensor

These large-scale prototypes have the overall dimensions of 4 mm x 2 mm x 1 mm. A misalignment of the wafers during bonding failed to produce a working prototype. Once all of the fabrication issues have been worked out and the proof of concept has been demonstrated, work can begin on scaling the sensor down to actual dimensions.

5.2 Extraocular Components

While fabrication issues of the sensor are being resolved, the extraocular components can be developed simultaneously. While the Data Acquisition and Processing Unit is required to complete the system, only the external coil is needed to demonstrate a proof of concept.

5.3 Chamber Testing

Upon delivery of a functional sensor prototype and completion of the external coil, testing of the sensor can begin. A cubic pressure chamber was constructed out of

1.78 cm thick PMMA. The sensor will be placed on the underside of the 2 mm thick PMMA lid while the external coil will be placed outside the chamber on top of the lid. The top of the chamber is sealed by gasket-to-gasket contact between the cube and the lid. Two c-clamps provide adequate pressure for a watertight seal. The base of the cube is joined to two square aluminum plates using silicone sealant. Sandwiched between the aluminum plates is a TE Technology potted HT-127-1.4-1.15-71 thermoelectric heater. The plates are joined by nuts and bolts at each of the four corners. The top plate is milled out on the top and bottom surfaces to the dimensions of the heater. This provides a path for heat flow from the heater to the interior of the chamber. Good thermal contact between the heater and plates is ensured by tightening the bolts and the application of thermal grease. The leads of the heater are connected to an Instek GPR-1810HD dc power supply. By adjusting the polarity and level of current to the heater, the chamber can be heated or cooled. A type T thermocouple leads into the interior of the chamber through a silicone sealed hole in the side of the cube. The thermocouple wire can be manipulated so that it records temperatures at the location of the sensor within the chamber. A manometer tube protrudes from the other side of the cube. Once the chamber is filled with water or saline solution to simulate the sensor environment, adjusting the height of the manometer tube provides a means of changing the pressure within the chamber from 0 to 60 mmHg. A meter stick attached to the side of the chamber provides a gauge for adjusting the height of the tube. The chamber is shown in Figures 5.3-4.

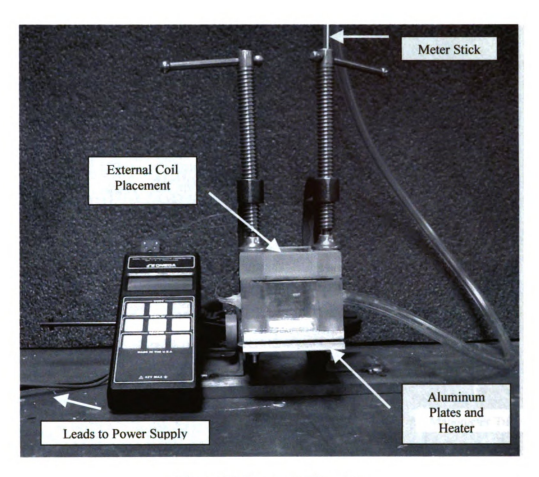


Figure 5.3 Pressure Chamber

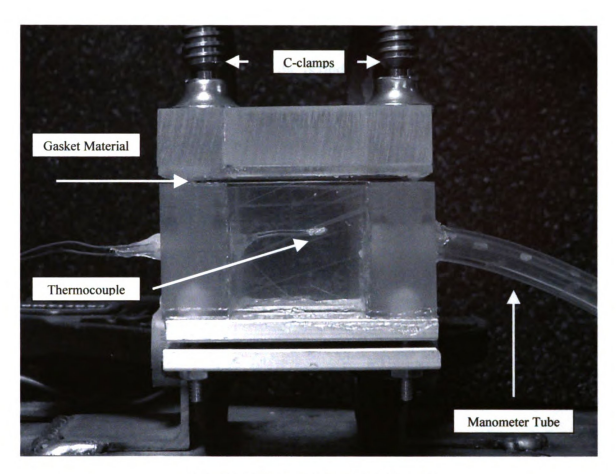


Figure 5.4 Pressure Chamber Close-up

Testing with the chamber will allow for calibration of sensor readings within the pressure range of interest. This will also allow an investigation of how sensor-coil spacing and orientation affect sensor readings. Using the heater to change the temperature of the chamber will provide an experimental TCR for the sensor. This will determine whether or not the sensor is capable of reading temperature as well as pressure.

5.4 Implantation

Once an actual scale prototype is received, the sensor may be implanted in the eyes of cats or monkeys to investigate biocompatibility issues. Short-term and long-term trials of up to six months can be performed to determine whether the external sensor materials suffer from *in vivo* etching, resulting in sensor failure. Implantation of the

sensor can also address the concern of sensor failure due to a fibrous encapsulation. Should this present a problem during the period of implantation, coatings such as the elastomer NUSIL and SiO₂ have shown promise at reducing cellular metabolic activity in other research [37,38].

Chapter 6. Social and Ethical Considerations

In today's society it is important to consider all the possible uses of a new technology before it is fully explored. Particularly in the biomedical field, a technology intended to help people could be used for harmful, if not tragic purposes. In the case of the MEMS pressure sensor, several issues need to be considered.

The external components of the IOP monitoring system will be designed to operate within certain limits. However, a large enough power source operating at extremely high frequencies could conceivably melt the sensor coil unleashing the sensor materials into the eye. All of the sensor materials themselves are biocompatible. Although, a harmful substance could be placed within the sensor cavity. An altered external device could then be programmed to destroy the sensor, releasing the harmful contents in the patient's body. While there are no issues with the sensor as designed, there are concerns as to what destructive additions could be made during implantation.

Powerful magnets have the potential to exert large forces on metallic objects. If a sensor is not removed from a patient, and they encounter a large magnet, serious damage could occur. A patient undergoing an MRI, for example, with the sensor coil still implanted, might experience severe injury to their eye. To take things a step further, strong magnets could be used to intentionally inflict harm to sensor patients.

Although the IOP monitoring system utilizes a wireless connection between internal and external components, surgery is still required to implant the sensor. Furthermore, the system demands the patient wear the external components on their

body. This may exclude them from certain physical activities or involve some discomfort.

The IOP monitoring system is being developed as a research tool to study the causes of acute and chronic IOP elevations and to help physicians learn more about the onset and progression of glaucoma. Continuous IOP monitoring will enhance the early detection of elevated IOP and aid in determining the success of various treatment strategies. The goal in developing this system is to ultimately reduce the number of people who suffer from glaucoma related blindness.

The IOP monitoring system will not be harmful to the patients unless negligence or bad intentions are involved. The potential for this research to improve the quality of life for people with elevated IOP levels outweighs the possibility it could be used to do harm.

Chapter 7. Conclusions

This work has produced several important pieces of information necessary for the development of the IOP monitoring system. A model was formulated to determine the resistance in the sensor's inductor coil as a function of temperature and frequency. While the resistance is not required for determining IOP, the author has demonstrated the potential for using the changing resistance values to record temperature as well as pressure from the sensor.

Once the sensor is implanted, a patient's IOP levels are indirectly determined from the voltage drop across the resistor in the external data acquisition and processing device. An alternate means of determining IOP has been presented by measuring the phase of the external device [15].

In order to accurately obtain IOP values from the voltage drop across the external resistor, a dip in the profile must be easily detectable. Calculations for thermal noise present a SNR >> 1, ensuring the required profile dip is distinguishable.

The presence of additional sensor capacitance due to the inductor coil was investigated. Any deviations from the nominal inductance were shown to have no detrimental effect on the sensor's operation. The sensitivity of the inductance to changes in temperature is 0.007 nH/°C and is therefore negligible.

The parallel plate model of the sensor's capacitance provides the only direct relationship between capacitance and the diaphragm's center spacing. However, two additional models were presented. Calibration of the device may prove these additional models to be more accurate as diaphragm deflection increases. The author has

demonstrated that the sensor capacitance will be determined from diaphragm deflection only, with negligible changes due to variations in cavity temperature and pressure. Furthermore, dielectric breakdown will not occur when relatively large voltages occur across the micron level gap of the capacitor.

Investigations into the sensor cavity have shown the cavity pressure has a significant sensitivity to temperature of 2.45 mmHg/°C. Resistive heating of the inductor combined with a temperature increase of 10°C would produce a deviation of 40.83% of the pressure range of interest (760 – 820 mmHg). The cavity temperature must therefore be known to accurately determine IOP.

Testing performed on cats verified that the temperature in the eye is not constant and will deviate from the body core temperature, as proposed by several articles [27, 28, 29]. The maximum temperature change achieved from blowing a jet of air at the eye of the subject was -3.22°C. Results suggest that a deviation of ± 5 °C from body core would encompass all possible temperatures that may occur in the human eye. An inspection of the testing showed that the temperature changes were a function of jet velocity and were more significant for colder jets, while the relative and absolute humidity of the jet was irrelevant. The author also generated a finite element heat transfer model of the eye, producing results comparable to those from the cat experiment.

While implanted in the eye, the temperature of the sensor's environment will vary several degrees. These variations will not affect the location of the voltage dip used to determine IOP readings from the sensor. However, temperature changes in the sensor have the potential to manifest themselves in the height of the voltage dip, allowing the

sensor to record temperature as well as pressure. Recording temperature will provide the cavity pressure values necessary to accurately determine IOP.

BIBLIOGRAPHY

BIBLIOGRAPHY

- 1. Glaucoma Research Foundation. 29 Nov. 2004. 1 Dec. 2004 http://www.glaucoma.org/>.
- 2. Hart, W. M. Jr., R. Ritch, M. B. Shields, and T. Krupin, eds. <u>The Glaucomas</u>. St. Louis: C. V. Mosby Co., 1989.
- 3. Chau, H., and K. D. Wise. "Scaling Limits in Batch-Fabricated Silicon Pressure Sensors." <u>IEEE Transactions on Electron Devices</u> ED-34.4 (1987): 850-858.
- 4. Goodall, Gregory Allen. "Design of an Implantable Micro-Scale Pressure Sensor for Managing Glaucoma." MA thesis. Michigan State U, 2002.
- 5. Everitt, W. L., eds. <u>Fundamentals of Radio and Electronics</u>. Englewood Cliffs, N.J.: Prentice-Hall Inc., 1958.
- 6. Kovacs, Gregory T. A. <u>Micromachined Transducers Sourcebook</u>. Boston: WCB, 1998.
- 7. Maseeh, F., and S. Sensturia. "Plastic Deformation of highly Doped Silicon." Sensors and Actuators, A: Physical 23.1-3 (1990): 861-865.
- 8. Cho, S. T., K. Najafi, and K. D. Wise. "Internal Stress Compensation and Scaling in Ultrasensitive Silicon Pressure Sensors." <u>IEEE Transactions on Electron Devices</u> 39.4 (1992): 836-842.
- 9. Senturia, S.D. Microsystem Design. Boston: Kluwer Academic Publishers, 2001.
- 10. Najafi, K. "Wafer Bonding." Lecture Notes. EECS 414. Center for Wireless Integrated MicroSystems, U of Michigan, Ann Arbor. Fall 2002.
- 11. Cengel, Yunus A., and Micheal A. Boles. <u>Thermodynamics: An Engineering Approach</u>. Boston: McGraw-Hill, 1998.
- 12. Zandman, Felix, Paul-Rene Simon, and Joseph Szwarc. Resistor Theory and Technology. Malvern, Pa: Vishay Intertechnology, 2001.
- 13. Elshabini-Riad, Aicha A. R., and Fred D. Barlow III. Thin Film Technology Handbook. New York: McGraw-Hill, 1998.
- 14. Cheng, David K. <u>Fundamentals of Engineering Electromagnetics</u>. Boston: Addison-Wesley, 1992.

- 15. Akar, O., T. Akin, and K. Najafi. "A Wireless Batch Sealed Absolute Capacitive Pressure Sensor." Sensors and Actuators, A: Physical 95.1 (2001): 29-38.
- 16. Lynch, Charles T., eds. <u>CRC Handbook of Materials Science</u>. vol 2. Cleveland: CRC Press, 1974.
- 17. Bowick, Chris. RF Circuit Design. Indianapolis: H.W. Sams, 1982.
- 18. Valkodai, A., and T. Manku. "Modeling and Designing Silicon Thin-Film Inductors and Transformers Using HSPICE for RFIC Applications." <u>Integration, the VLSI Journal</u> 24.2 (1997): 159-171.
- 19. Lynch, Charles T., eds. <u>CRC Handbook of Materials Science</u>. vol 3. Cleveland: CRC Press, 1974.
- 20. Mohan, S. S., M. del Mar Hershenson, S. P. Boyd, and T. H. Lee. "Simple Accurate Expressions for Planar Spiral Inductances." <u>IEEE Journal of Solid-State Circuits</u> 34.10 (1999): 1419-1420.
- 21. Avdeev, Ilya V., "New Formulation for Finite Element Modeling Electrostatically Driven Microelectromechanical Systems." Diss. U of Pittsburgh, 2003.
- 22. Nayar, Alok. The Metals Databook. New York: McGraw-Hill, 1997.
- 23. Wallash, Al, and Larry Levit. "Electrical Breakdown and ESD Phenomenon for Devices with Nanometer-to-Micron Gaps." Proceedings of Reliability Testing and Characterization of MEMS/MEOMS II, SPIE Conference. Paper 4980-10, 2003.
- 24. Walraven, J. A., J.M. Soden, D. M. Tanner, P. Tangyunyong, E. I. Cole Jr., R. R. Anderson, and L. W. Irwin. "Electrostatic Discharge/Electrical Overstress susceptibility in MEMS: A new Failure Mode." <u>Proceedings of SPIE The International Society for Optical Engineering</u> 4180 (2000): 30-39.
- 25. Incropera, Frank P., and David P. DeWitt. <u>Introduction to Heat Transfer</u>. New York: Wiley, 2002.
- 26. Collins, C. C. "Miniature Passive Pressure Transensor for Implanting in the Eye" IEEE Transactions on Bio-Medical Engineering BME-14.2 (1967): 74-83.
- 27. Scott, J.A. "A Finite Element Model of Heat Transport in the Human Eye." Physics in Medicine and Biology 33.2 (1988): 227-241.
- 28. Scott, J. A. "The Computation of Temperature Rises in the Human Eye Induced by Infrared Radiation." Physics in Medicine and Biology 33.2 (1988): 243-247.

- 29. Lagendijk, J. J. W. "A Mathematical Model to Calculate Temperature Distributions in Human and Rabbit Eyes During Hyperthermic Treatment." Physics in Medicine and Biology 27.11 (1982): 1301-1311.
- 30. Gustrau, F., and A. Bahr. "W-Band Investigation of Material Parameters, SAR Distribution, and Thermal Response in Human Tissue." <u>IEEE Transactions on Microwave Theory and Techniques</u> 50.10 (2002): 2393-2400.
- 31. Amara, E.H. "Numerical Investigations on Thermal Effects of Laser-Ocular Media Interaction." <u>International Journal of Heat and Mass Transfer</u> 33.13 (1995): 2479-2488.
- 32. Lee, D. H., Y. S. Chung, and D. S. Kim. "Turbulent Flow and Heat Transfer Measurements on a Curved Surface with a Fully Developed Round Impinging Jet." <u>International Journal of Heat and Fluid Flow</u> 18.1 (1997): 160-169.
- 33. Richards, D. R., and L. W. Florshuetz. "Forced Convection Heat Transfer to Air/Water Vapor Mixtures." <u>Proceedings of the Eighth International Heat Transfer Conference</u> 3 (1986): 1053-1058.
- 34. Hilsenrath, Joseph. <u>Tables of Thermal Properties of Gases</u>. Washington: U.S. Dept. of Commerce, National Bureau of Standards, 1955.
- 35. Moran, Micheal J., Howard N. Shapiro. <u>Fundamentals of Engineering Thermodynamics</u>. New York: Wiley, 2000.
- 36. NIST Chemistry WebBook. March 2003. 1 Nov. 2004. http://webbook.nist.gov/chemistry/fluid/
- Hierold, C., B. Clasbrummel, D. Behrend, T. Scheiter, M. Steger, K. Oppermann, H. Kapels, E. Landgraf, D. Wenzel, and D. Etzrodt. "Implantable Low Power Integrated Pressure Sensor System for Minimal Invasive Telemetric Patient Monitoring." Proceedings of the IEEE Micro Electro Mechanical Systems (MEMS) (1998): 568-573.
- 38. Kotzar, G., M. Freas, P. Abel, A. Fleischman, S. Roy, C. Zorman, J. M. Moran, and J. Melzak. "Evaluation of MEMS Materials of Construction for Implantable Medical Devices." <u>Biomaterials</u> 23 (2002): 2737-2750.

